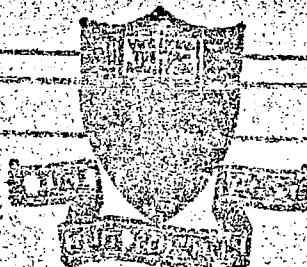
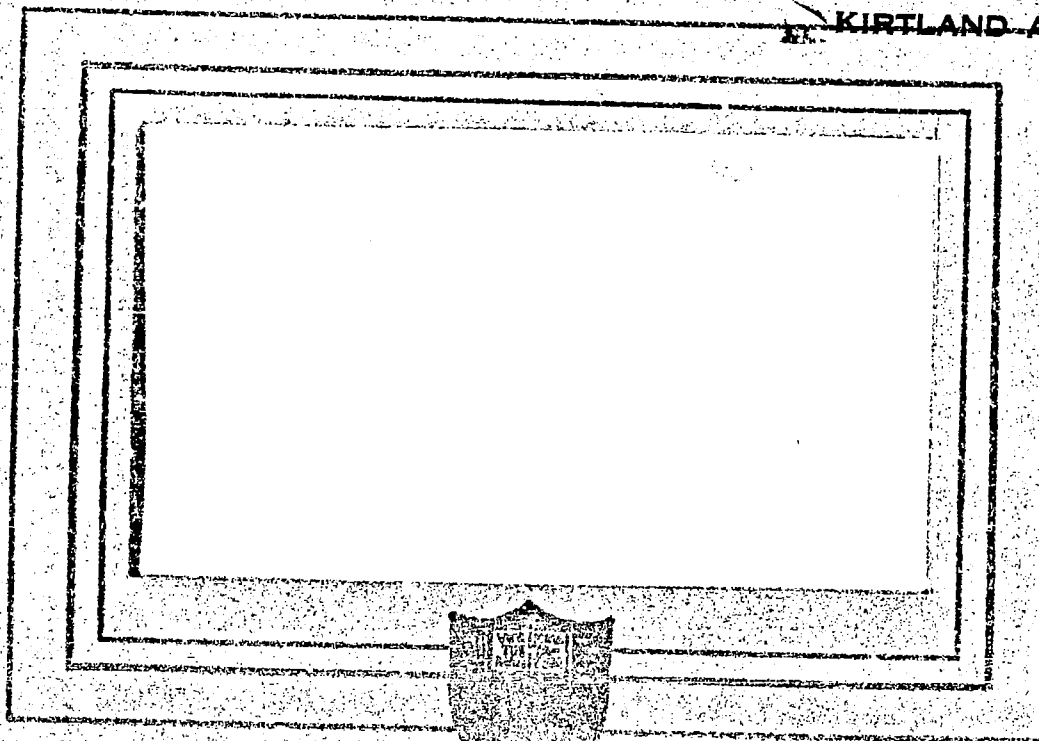


LOAN COPY: RET
AFWL TECHNICAL
KIRTLAND AFB,



N 69-20350	
(ACCESSION NUMBER)	(THRU)
130	1
(PAGES)	(CODE)
Q# 100386	25
(MAGA CR OR TMX OR AD NUMBER)	(CATEGORY)



PRINCETON UNIVERSITY
DEPARTMENT OF
AEROSPACE AND MECHANICAL SCIENCES





0063013

NASA
PEGA -

NGL 31-001-005
Supplement No. 7
(was NSG 360-63)

Prepared for
National Aeronautics
and Space Administration

4. PULSED ELECTROMAGNETIC GAS ACCELERATION

13th Semi-annual Progress Report
1 July 1968 to 31 December 1968

Report 634

Prepared by:

Robert G. Jahn
Professor
and Research Leader

and:

Woldemar F. von Jaskowsky
Senior Research Engineer
and Lecturer

Reproduction, translation, publication, use and disposal in whole, or in part, by or for the United States Government is permitted.

January 1969

School of Engineering and Applied Science
Department of Aerospace and Mechanical Sciences
Guggenheim Aerospace Propulsion Laboratories
3. PRINCETON UNIVERSITY
Princeton, New Jersey

ABSTRACT

Current sheets propagating in a parallel-plate accelerator are found to arrest their motion at an electrode-insulator junction, and there to lapse into stable, quasi-steady discharges. Kerr-cell photography, magnetic and electric probing and terminal voltage measurements indicate that these stabilized discharges accelerate gas through themselves as long as gas from the prefilling of the discharge chamber is available, after which enhanced erosion of insulator and electrode material appears. To supply fresh gas to the stabilized current zone with a minimum of delay, a shock tube gas injection technique is used. Even with this procedure, it is found that the current must be driven for hundreds of microseconds before a quasi-steady gas flow can be established in contrast to the tens of microseconds required for electrodynamic stabilization. This quasi-steady flow mode, characterized by both current pattern and gas flow stabilization is again observed to provide substantial acceleration of the inlet flow.

A similar steady state acceleration phase can be achieved in a coaxial electrode geometry by synchronized application of tailored pulses of mass flow and current. This diffuse discharge, characterized by a stabilized current distribution, constant voltage and current, and a steady argon mass flow rate of up to 50 g/sec, is of considerable interest as both a pulsed thruster and as a simulator of the self-field MPD arcjet over a power range from 100 kW to 100 MW. Kerr-cell photographs and experimental maps of the current distribution in the exhaust plume and interelectrode region clearly show the rapid transition to this steady configuration, as well as characteristic arc behavior for mass starvation and mass overfeed. Terminal voltage measurements, taken over a wide range of power and mass flow rate, are sufficiently precise to allow discrimination among several theoretical models of the acceleration process.

The process of energy transfer from a pulse network to

ABSTRACT-contd.

a propagating current sheet is studied experimentally and analytically in a linear pinch configuration. The efficiency of this process is related to the ratios of pulse line impedance/average discharge impedance, and current pulse duration/characteristic acceleration time. Experiments in hydrogen, argon, krypton, and nitrogen at a common ambient mass density and impedance ratios near unity yield efficiencies that exhibit the same qualitative variation with these ratios as those predicted, but only the hydrogen data show good quantitative agreement with the theoretical values. This failure of the theoretical model for the higher molecular weight gases is traced to the existence of diffuse current patterns flowing in the region behind the propagating current sheet, contrary to the theoretical "snowplow" assumption that all of the current flows in a thin sheet.

The structure of the current sheet in a similar pinch discharge is studied with a specialized high-speed piezoelectric pressure transducer, which is capable of determining profiles of both axial and radial pressure. Correlation of these data with electric and magnetic field profiles, along with luminosity and voltage records, indicate three distinct zones within the sheet; in sequence, regions of electron current conduction (I), mass accumulation with ion current conduction (II), and induced flow of unswept gas (III) are dominant. Profiles of particle density, velocity, and temperature can be evaluated, and the current sheet is found to entrain a large percentage of the gas encountered. A momentum balance across the sheet is in approximate agreement with snowplow predictions, but the distributions of current and mass density do not agree with piston-shock wave models.

Studies continue on the structure of the anode attachment portion of high-current discharges, and its effect on

ABSTRACT-contd.

the overall voltage. A new series of experiments probe a similar regime near the cathode. Laser techniques have been extended to search for population inversions in the outflow plasma from the quasi-steady parallel-plate accelerator. Finally a 10^5 joule pulse network is under construction to extend by an order of magnitude the available test times of all quasi-steady discharge equipment.

CONTENTS

	Page
Title Page	i
Abstract	ii
Contents	v
List of Illustrations.	vii
Current Student Participation.	x
 I. INTRODUCTION.	 1
II. CURRENT PATTERN AND GAS FLOW STABILIZATION IN PULSED PLASMA ACCELERATORS (Eckbreth).	 2
Current Pattern Stabilization	2
Quasi-steady Plasma Acceleration.	24
Summary	29
III. QUASI-STEADY PLASMA ACCELERATION (Clark).	31
Experimental Design	31
Luminosity Patterns	42
Terminal Voltage.	42
Current Density Distribution.	48
IV. ENERGY TRANSFER FROM A PULSE NETWORK TO A PROPAGATING CURRENT SHEET (Wilbur)	 52
Theoretical Analysis.	54
Experimental Behavior	66
Summary	78
V. PRESSURE DISTRIBUTION IN THE STRUCTURE OF A PROPAGATING CURRENT SHEET (York)	 81
Apparatus and Current Sheet Observations.	81
Pressure Probe Development.	84
Pressure Probe - Current Sheet Interaction.	88
Experimental Determination of Current Sheet Profiles	 92
Current Sheet Structure and Dynamics.	95
VI. POTENTIAL DISTRIBUTIONS IN A PINCH CHAMBER (Oberth).	 102
VII. POPULATION INVERSION IN A PULSED DISCHARGE (Bruckner).	 105

CONTENTS-contd.

	Page
VIII. CATHODE JET STUDIES (Turchi)	107
IX. A 100 KILOJOULE PULSE-FORMING NETWORK POWER SUPPLY FOR A QUASI-STEADY PLASMA ACCELERATOR (Di Capua)	111
PROJECT REFERENCES	117
GENERAL REFERENCES	123
APPENDIX A. SEMI-ANNUAL STATEMENT OF EXPENDITURES . . .	124

LIST OF ILLUSTRATIONS

Figure		Page
1	Schematic diagram of parallel-plate accelerator . .	4
2	Kerr-cell photographs of propagating current sheet.	6
3	Kerr-cell photographs of transition to stabilized current distribution.	7
4a	Enclosed current contours (K-Amp) in parallel-plate accelerator	9
4b	Enclosed current contours (K-Amp) in parallel-plate accelerator	10
4c	Enclosed current contours (K-Amp) in parallel-plate accelerator	11
5	Voltage signatures of current sheet stabilization .	12
6	Airfoil visualization of gas flow into stabilized current distribution.	15
7	Airfoil visualization of gas flow through stabilized current distribution	16
8	Electric probe signatures of current sheet stabilization; streamwise electric field, E_x	18
9	Trajectories of characteristic features of electric probe signatures	19
10	Transverse electric field signatures.	21
11	Shock tube gas injection system	23
12	Voltage signatures for 2-in. electrode length . . .	25
13	Luminosity of the anode and cathode jets.	28
14	Characteristic times for current pulse and mass flow	33
15	Schematic of mass injection system.	34
16	Synchronization of current pulse to injected mass pulse.	36
17	Mass flow for purely electromagnetic thrust	38
18	Discharge chamber	40
19	Electrical schematic.	41
20	Stabilized exhaust luminosity at 17.5 kA.	43
21	Typical voltage and current traces.	44
22	Summary of voltage measurements	46
23	Voltage component variation with mass flow rate . .	49

LIST OF ILLUSTRATIONS-contd.

Figure		Page
24	Stabilized current distribution	50
25	Transmission line discharging through a resistive load.	53
26	Schematic of pulse line accelerator system.	56
27	Computed current, voltage waveforms, and sheet trajectories.	58
28	Effect of current pulse length on efficiency.	62
29	The effect of pulse length and impedance on efficiency	64
30	Efficiency vs. pulse line impedance	65
31	Theoretical and experimental waveforms from matched capacitor line.	67
32	Typical capacitor arrangement	69
33	Efficiency profiles	71
34a	Efficiency profile: nitrogen - experimental.	72
34b	Efficiency profile: krypton - experimental	73
34c	Efficiency profile: hydrogen - experimental.	74
35	Voltage and current waveforms	77
36	Current trajectories.	79
37	Discharge chamber arrangement for pressure probe studies	82
38	Circuit current waveform and radial view photo- graphs of pinch discharge	83
39	Schematic of piezoelectric pressure transducer.	85
40	Pressure probe response to a reflected shock in shock tube	87
41	Luminosity patterns about radial probe.	89
42	Luminosity patterns about axial probe with flow insulator.	90
43	Effect of flow isolator on probe response	91
44	Typical probe responses	93
45	Current density, radial, and axial pressure profiles.	96
46	Estimated number density and current density profiles.	98

LIST OF ILLUSTRATIONS-contd.

Figure		Page
47	Estimated temperature and current density profiles.	99
48	Radial variation of peak density, width of entrained zone, and sweeping efficiency	101
49	Voltage distribution across chamber at 1-in. radius.	103
50	Potential contours in chamber	104
51	Schematic diagram of parallel-plate accelerator modified for cathode jet studies.	109
52	Schematic of pulse-forming network.	113
53	Voltage and current in fuse test.	115

CURRENT STUDENT PARTICIPATION

<u>Student</u>	<u>Period</u>	<u>Degree</u>	<u>Thesis Topic</u>
BOYLE, Michael J.	1968-	B.S.E. Cand.	Plasma Velocity Measure- ments
BRUCKNER, Adam P.	1966-	Ph.D. Cand.	Gas Laser Interferometry of Closed Chamber Discharges
CLARK, Kenn E.	1965-1969	Ph.D.	Quasi-steady Plasma Accel- eration
DI CAPUA, Marco S.	1966-	Ph.D. Cand.	Current-voltage Character- istics of High-current Discharges
ECKBRETH, Alan C.	1964-1968	Ph.D.	Current Pattern and Gas Flow Stabilization in Pulsed Plasma Accelerators
OBERTH, Ronald C.	1966-	Ph.D. Cand.	Current Sheet Anode Foot Phenomena
SPRENGEL, Uwe W.	1968-	Visiting Scholar	Ion Velocity Measurement in MPD Discharges
TURCHI, Peter J.	1963-	Ph.D. Cand.	Unsteady Plasma Diagnostics
VAN WOERKOM, Paul	1968-	Visiting Scholar	Static Breakdown Character- istics of Various Electrode Configurations
WILBUR, Paul J.	1966-1968	Ph.D.	Energy Transfer from a Pulse Network to a Propagating Cur- rent Sheet
YORK, Thomas M.	1965-1968	Ph.D.	Pressure Distribution in the Structure of a Propagating Current Sheet

I. INTRODUCTION

The reporting period just past has encompassed the completion of no less than four Ph.D. programs. Each of these studies has been presented in detail in the usual Ph.D. thesis format, [55,58,60,66] and each is the subject of an oral presentation and preprint at a technical society meeting [62 to 70]. It still seems appropriate, however, that this semi-annual report should contain concise reviews of these researches, particularly to emphasize the relation among them, and to define the perimeter of progress of the project as a whole.

The programs of the four younger men in our laboratory are now in transition from exploratory phases to the detailed experiments which will constitute their Ph.D. theses. Hence, there has been considerable design, assembly, and testing of new equipment, but less acquisition of hard data in these topic areas. Brief reviews of these efforts provide some flavor of the laboratory programs which will grow in the coming months to complement the continuing studies in the well-established facilities.

II. CURRENT PATTERN AND GAS FLOW STABILIZATION IN PULSED PLASMA ACCELERATORS (Eckbreth)

Two phases of stabilization have been identified in pulsed plasma accelerators: (1) current pattern stabilization, in which formerly convecting current distributions cease to propagate, and (2) gas flow stabilization, wherein an externally supplied gas flow achieves a steady acceleration profile through the stabilized current pattern. These stabilization processes are of interest in pulsed plasma accelerators both because of the fundamental questions they pose and because of their practical implementations. For example, one may inquire about the effect of current pattern stabilization on the plasma ejection losses of a pulsed accelerator, or about the details of the plasma acceleration process in a quasi-steady plasma accelerator, i.e., an accelerator in which both current pattern and gas flow stabilization coexist. On the other hand, one may employ such a quasi-steady accelerator to simulate a high-power, steady electromagnetic thruster, such as a magnetoplasmadynamic arc, for a short time. In this way one could, using transient instrumentation techniques, perform detailed interior diagnostic studies on an arc-accelerator environment which in the steady state would be too hostile for probing. Operation of an accelerator in the quasi-steady mode is of interest in its own right since this may well be the regime of operation in which electromagnetic acceleration processes are optimized. The quasi-steady regime shares many of the advantages of short-pulse operation and several of the advantages of steady state operation, while apparently possessing less of the disadvantages of either pulsed or steady operation alone.

Current Pattern Stabilization

Current pattern stabilization was first observed in connection with a series of pulsed exhaust experiments on a

linear pinch fitted with an anode containing a large circular orifice [57]. Stabilization of the current contours projecting out through the orifice occurred when the device was driven with rectangular current pulses of duration greatly in excess of the "pinch" time of the cylindrical current sheet formed inside the pinch chamber. In order to study these phenomena in a simpler geometry, a parallel-plate accelerator [57,58] was constructed. Stabilization of the propagating current sheets in this device was achieved by partially insulating the electrode surfaces with thin mylar sheets from a position several inches downstream of the discharge initiation location to the front end of the accelerator as shown schematically in Fig. 1. These initial studies, which established that spatial stabilization of the propagating current sheets occurred at the electrode-to-insulator junction, have now been supplemented by more detailed diagnostic studies performed with a pair of permanently insulated electrodes.

The "electrodes" consist of 5 1/4-in. lengths of aluminum surface followed by 42 3/4-in. lengths of nylon inlaid insulator surface. The discharge chamber formed by the two electrodes is 48-in. long, 6-in. wide, and has a 2-in. inter-electrode spacing maintained by a rectangular plexiglas housing which forms the side walls of the apparatus. A switch electrode is mounted 2 in. below the bottom electrode in a separate plexiglas switch chamber. In operation, the switch electrode is connected to the capacitor bank, charged to -10 kV. The top electrode of the accelerator is grounded and the middle electrode is maintained at ground potential during the charging process by means of a ballast resistor, R_B , connecting the top and middle electrodes. The switch is triggered by injecting argon into its initially evacuated chamber. As the gas pressure increases, the Paschen curve is crossed and the switch discharge initiates, transferring the voltage across the electrodes of the main chamber, result-

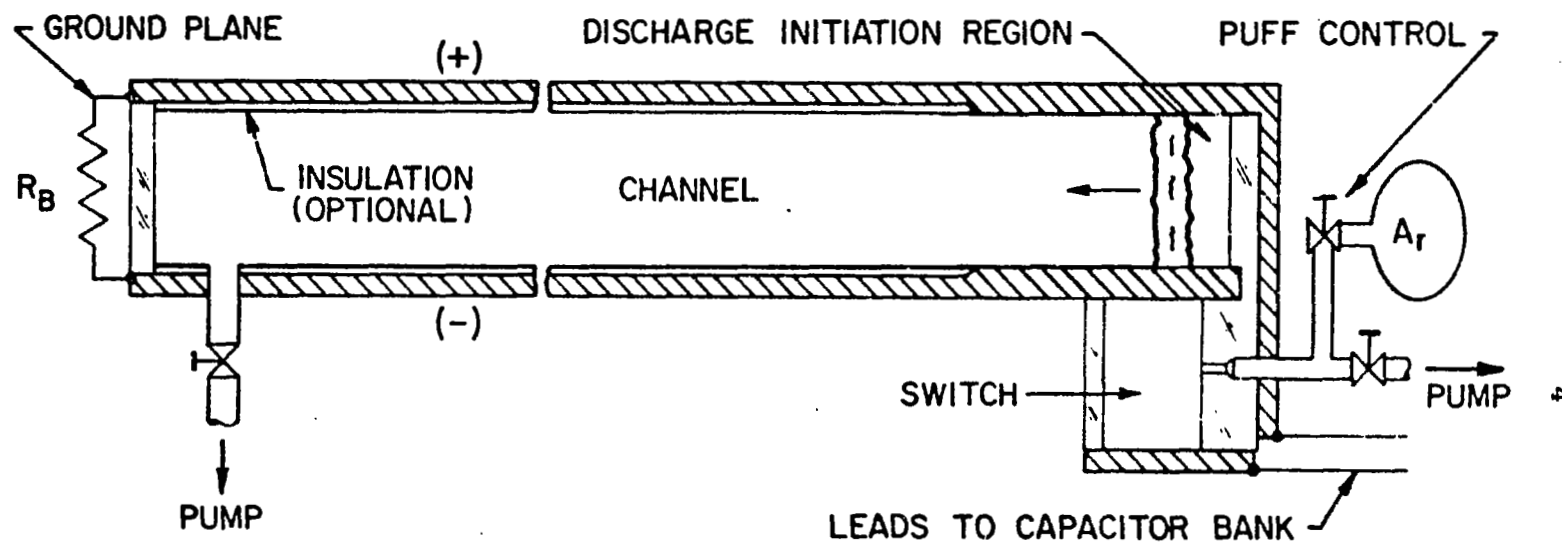


FIGURE 1

SCHEMATIC DIAGRAM OF PARALLEL PLATE ACCELERATOR

ing in the desired test gas breakdown, sheet formation, propagation, and eventual stabilization processes. The test gas in the main chamber may be set in advance at a given pressure--the "ambient mode"--or may be injected by a shock tube, a process to be described in detail in connection with the establishment of the quasi-steady mode of operation.

The capacitor bank consists of $40 \times 3.2 \mu\text{f}$ capacitors arranged in various LC ladder network configurations to deliver rectangular current pulses ranging from 120,000 amperes for 20 μsec , hereafter designated 120/20, to a nominal 5,000 amperes for 500 μsec , i.e., 5/500. In the current pattern stabilization studies to be discussed, the 120/20 pulse is employed and discharged into 100 μ argon, the ambient mode.

50 nanosecond Kerr-cell photography is used to view the luminosity associated with various phases of the discharge. The character of the propagating sheet may be seen in Fig. 2 which is a sequence of photographs taken normal to the direction of propagation through the side wall. In these illustrations, Δx is a streamwise coordinate referenced to the metal-to-insulation boundary such that $\Delta x > 0$ is downstream along the insulator, and $\Delta x < 0$ is upstream along the metal electrode portion of the accelerator. The luminous sheet is observed to be nearly one-dimensional at the time of breakdown near the back wall of the apparatus, but to become highly two-dimensional as it propagates down the channel. Of interest is the development of a diffuse "anode foot" which enlarges and grows as the sheet propagates. Inception of such a foot has been observed in other experiments of this type [48,51,54], but here it progresses nearly to the point that it completely dominates the entire luminous pattern, tilting it substantially with respect to the axis and diffusing it over a large dimension.

When the propagating luminous front reaches the end of the exposed electrode, Fig. 3, the luminosity pattern continues

ANODE

A 894

 $1 \mu \text{ sec}$

CATHODE

A 892

 $2 \mu \text{ sec}$

A 891

 $3 \mu \text{ sec}$ Δx

-2.9"

-5.3"

A 897

 $4 \mu \text{ sec}$

A 898

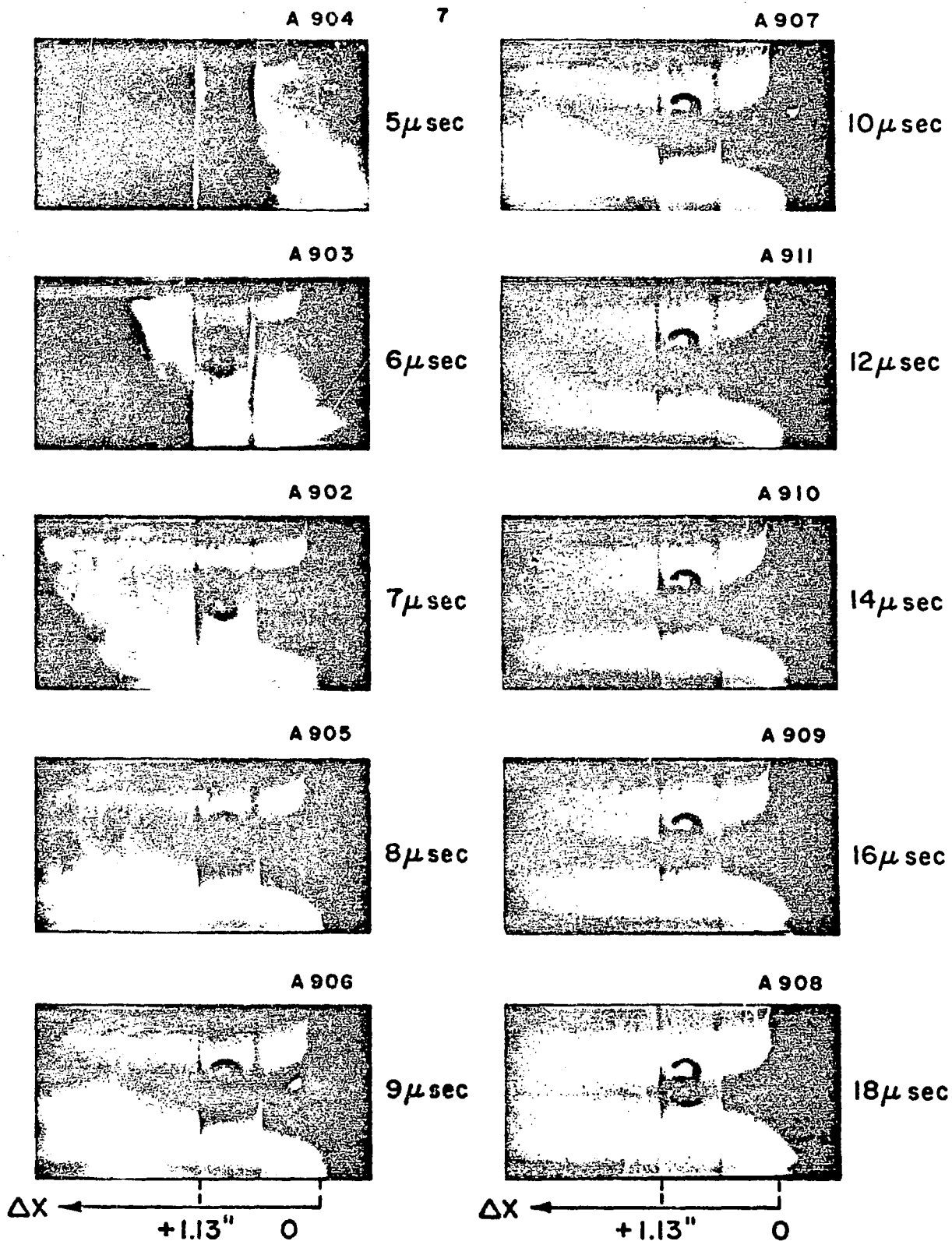
 $5 \mu \text{ sec}$ Δx

0.38" 0

-2.1"

KERR CELL PHOTOGRAPHS OF PROPAGATING
CURRENT SHEET

FIGURE 2



KERR CELL PHOTOGRAPHS OF TRANSITION
TO STABILIZED CURRENT DISTRIBUTION

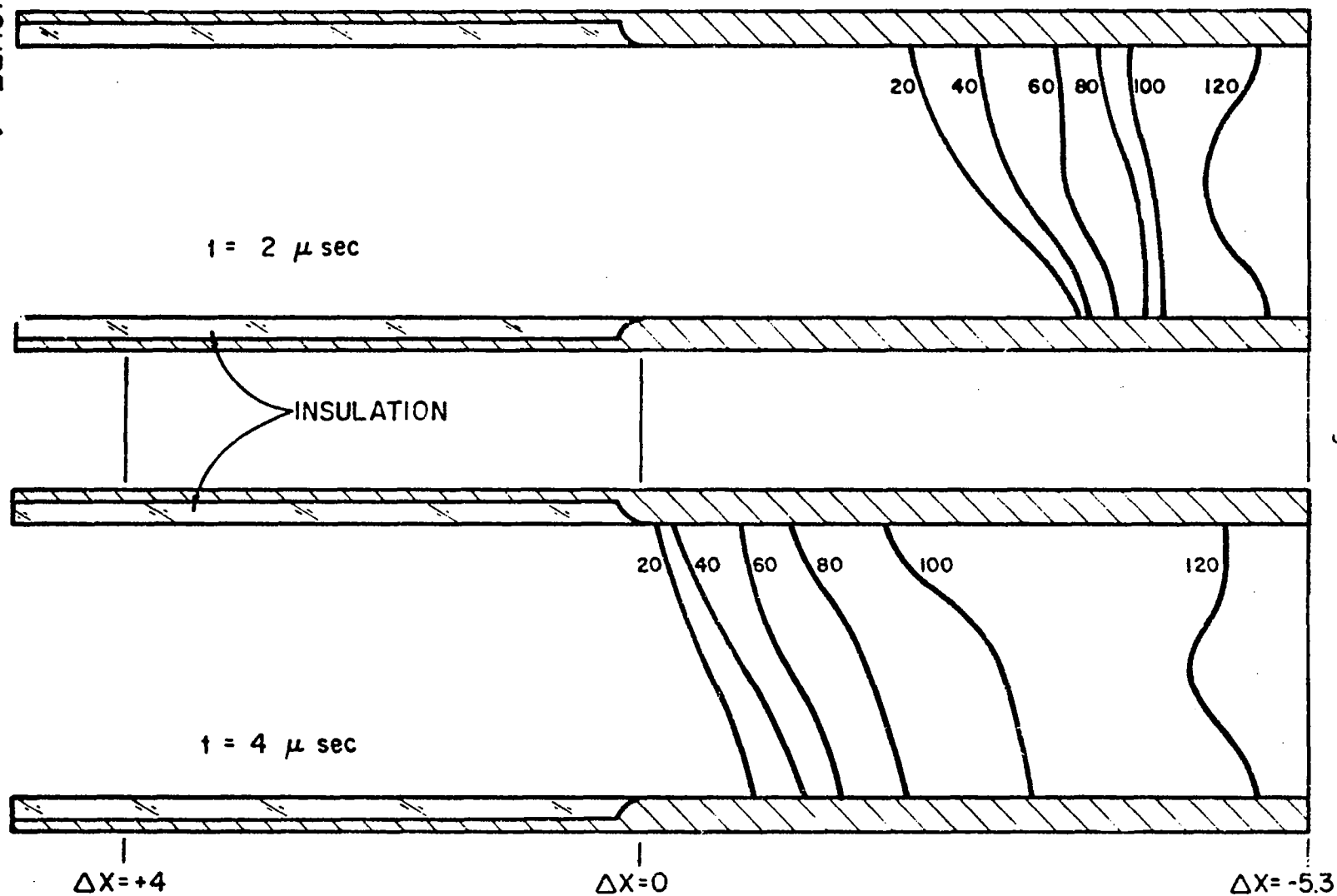
FIGURE 3

to propagate into the insulated channel unrolling, as it were, the stabilized pattern of two broad, nearly axial, and highly luminous bands emanating from the electrode discontinuity. One may speculate that these bright bands are analogous to the anode and cathode jets commonly seen in the magnetoplasmadynamic arcjet.

Confirmation that the current-carrying region has indeed ceased to propagate is best supplied by maps of enclosed current contours at a succession of times derived from magnetic field probing of the entire discharge volume. These maps are displayed in Fig. 4 where the individual contours conform to local current streamlines and their numeral indicates the cumulative current passing everywhere downstream. The slight tilt of the propagating current sheet, its broad anode attachment region and its abrupt arrest at the electrode discontinuity are again evident, in agreement with the luminosity studies. The stabilized pattern bows downstream in a hairpin fashion with the bulk of the current conducted across the midplane in the $0 < \Delta x < 6$ in. region, i.e., within three channel heights downstream of the metal-to-insulation junction.

Additional confirmation of current pattern stabilization and valuable indication that the pattern indeed continues to accelerate gas through itself in its stabilized phase is provided by a sequence of terminal voltage measurements made with an inner divider. This device is simply a voltage tap which passes through an insulated port in the anode to electrical contact with the cathode and enables one to separate the resistive and inductive voltage drops in the plasma. Should the current sheet come to rest and start accelerating gas through itself at a speed u , the probe will also record the corresponding motional emf, regardless of its location. In Fig. 5a the response of the inner divider at $\Delta x = -2 \frac{1}{4}$ in., along the metal electrodes, is shown. Before the current sheet sweeps by the probe position, only the resistive drop, here about

FIGURE 4a



ENCLOSED CURRENT CONTOURS (K-Amp) IN PARALLEL PLATE ACCELERATOR

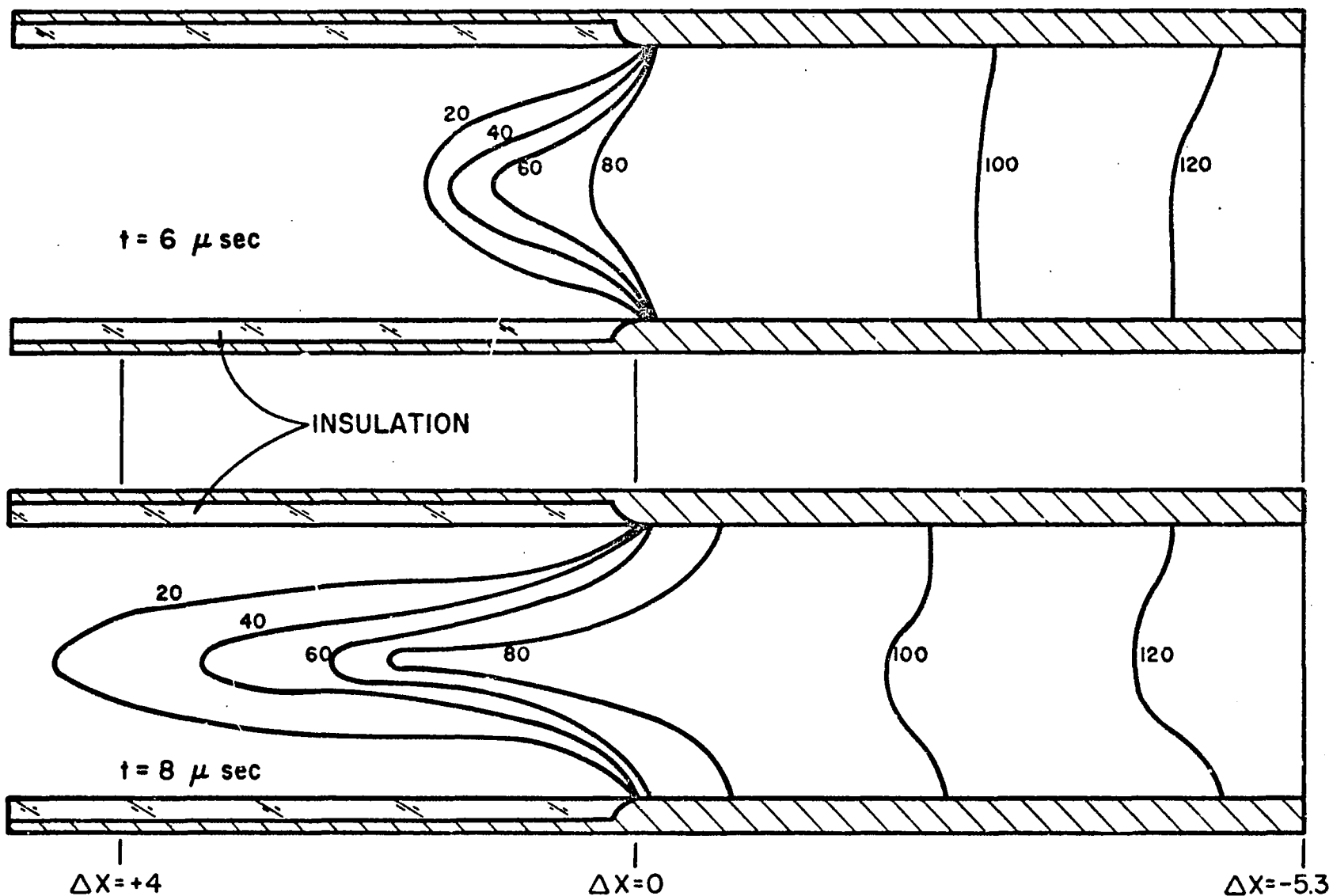
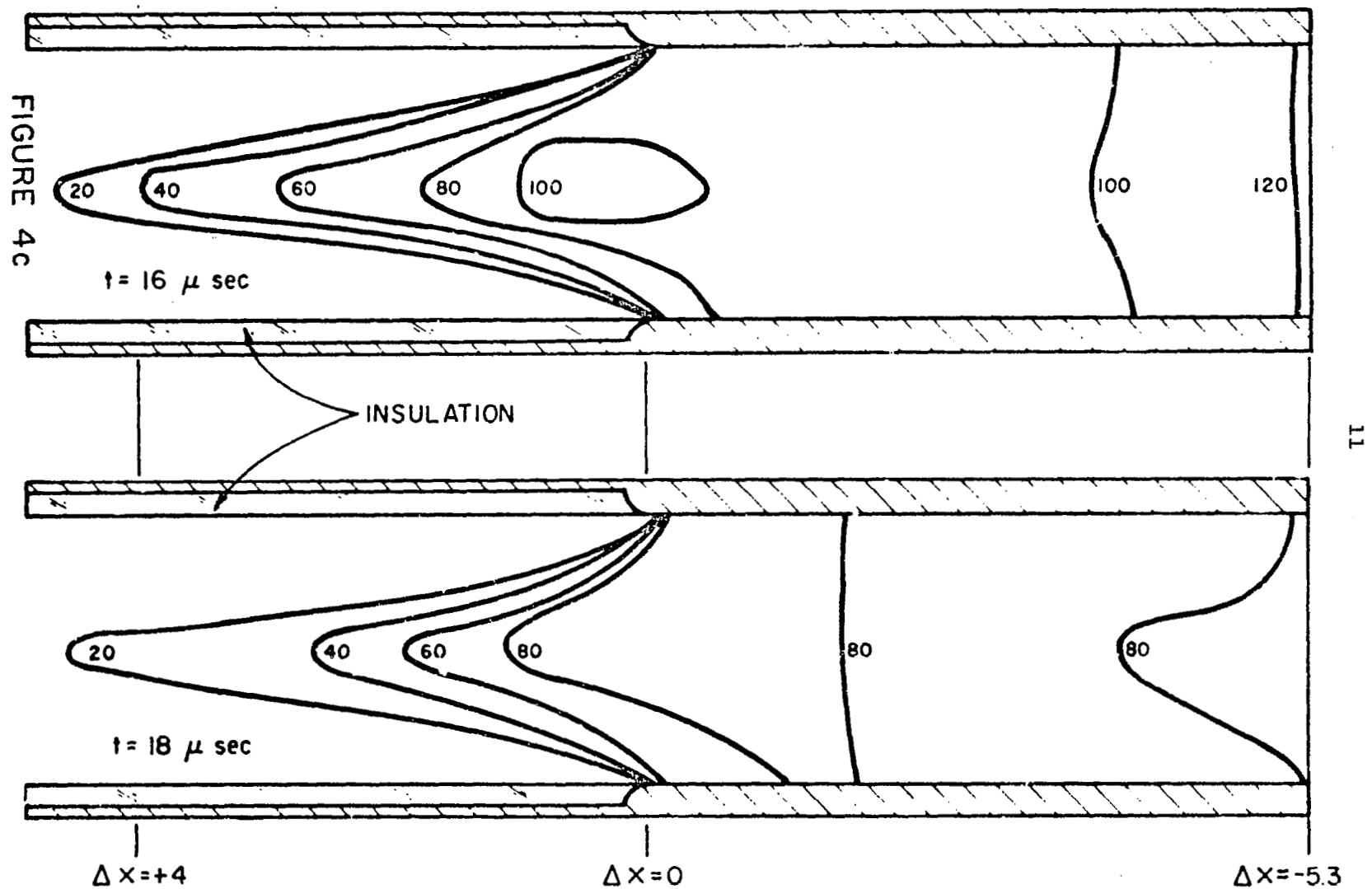
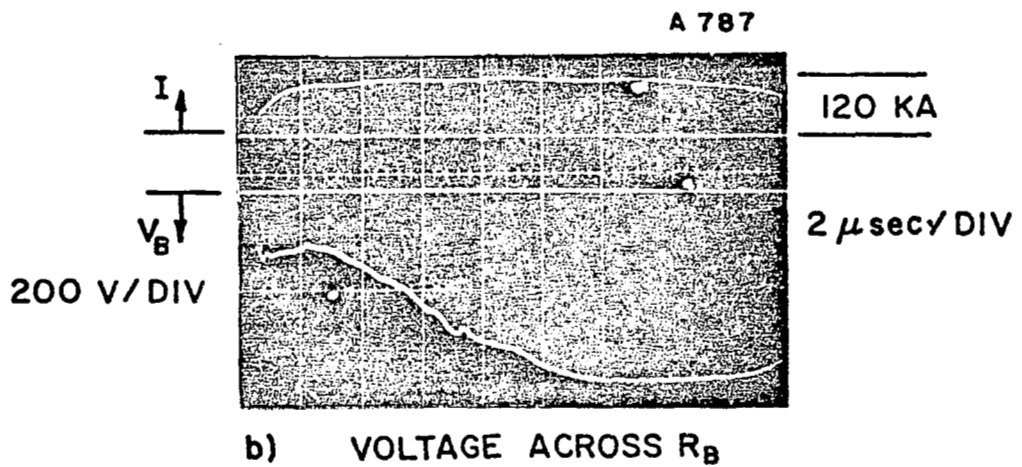
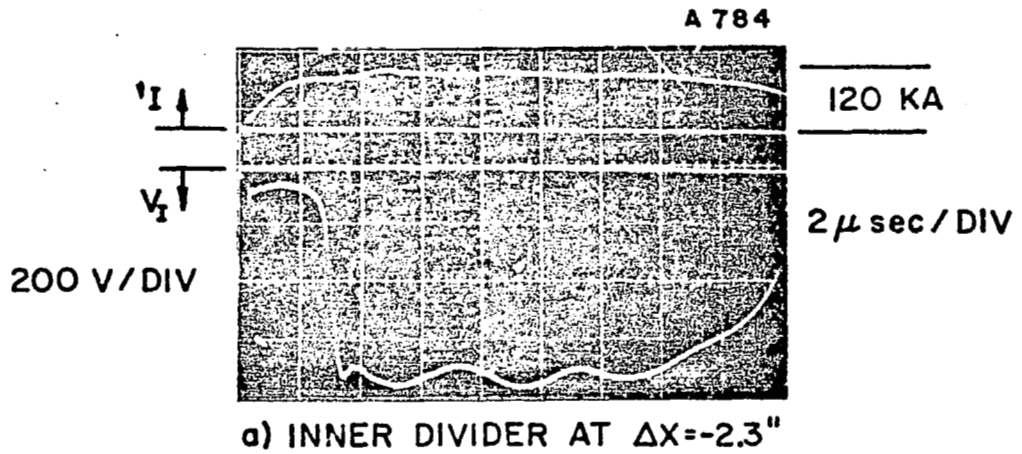


FIGURE 4b

ENCLOSED CURRENT CONTOURS (K-Amp) IN PARALLEL PLATE ACCELERATOR



ENCLOSED CURRENT CONTOURS (K-Amp) IN PARALLEL PLATE ACCELERATOR



VOLTAGE SIGNATURES OF CURRENT
SHEET STABILIZATION

FIGURE 5

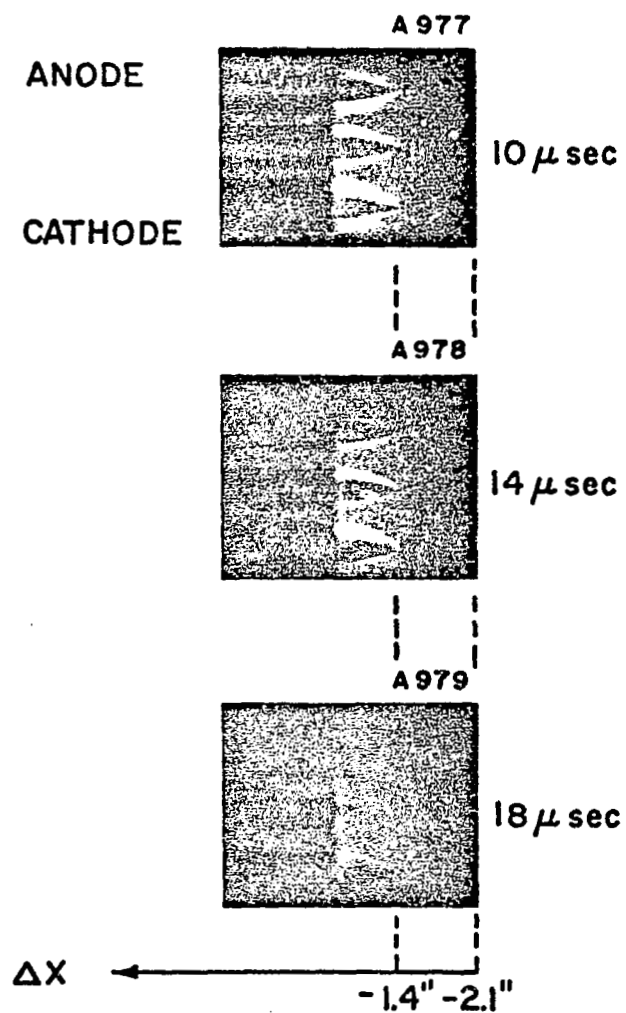
60 V, is monitored. This corresponds to a plasma resistance of approximately 0.0005Ω . As the sheet sweeps by the probing location, the inductance change due to the motion of the sheet is added bringing the total voltage to about 700 V. As the sheet stabilizes, however, this changing inductive contribution should vanish. Note, however, that the voltage signature remains nearly constant. It is hypothesized that the declining flux change contribution is supplemented by the generation of a back $\vec{u} \times \vec{B}$ emf as the stabilizing current begins to accelerate gas through itself. This hypothesis is verified by monitoring the voltage at the far downstream end of the accelerator where it is impossible to enclose any flux change contribution. The response of the voltage probe at this position is shown in Fig. 5b; initially only the resistive drop is recorded but as stabilization of the current sheet occurs, the back emf contribution is also added.

It thus appears that a new and rather powerful electromagnetic inertial mechanism is operating, i.e., that when the motion of the convecting current sheet is arrested at the electrode discontinuity, the back emf generated in opposition to this change is just sufficient to maintain the terminal voltage at its previous level. The impressive feature of this effect is that the gasdynamic processes involved in its accomplishment are fundamentally quite distinct; that is, there has been a transition from the familiar unsteady mode of gas "sweeping" in a propagating sheet to the equally familiar but rather different steady mode of gas "blowing" through a fixed current pattern, with no observable change in terminal voltage.

Although the current has ceased to propagate, acceleration of the gas by the stabilized current distribution appears to continue. The most vivid demonstration of flow acceleration is a photographic sequence of the luminous patterns over small 15° half angle wedges set in 3 planes,

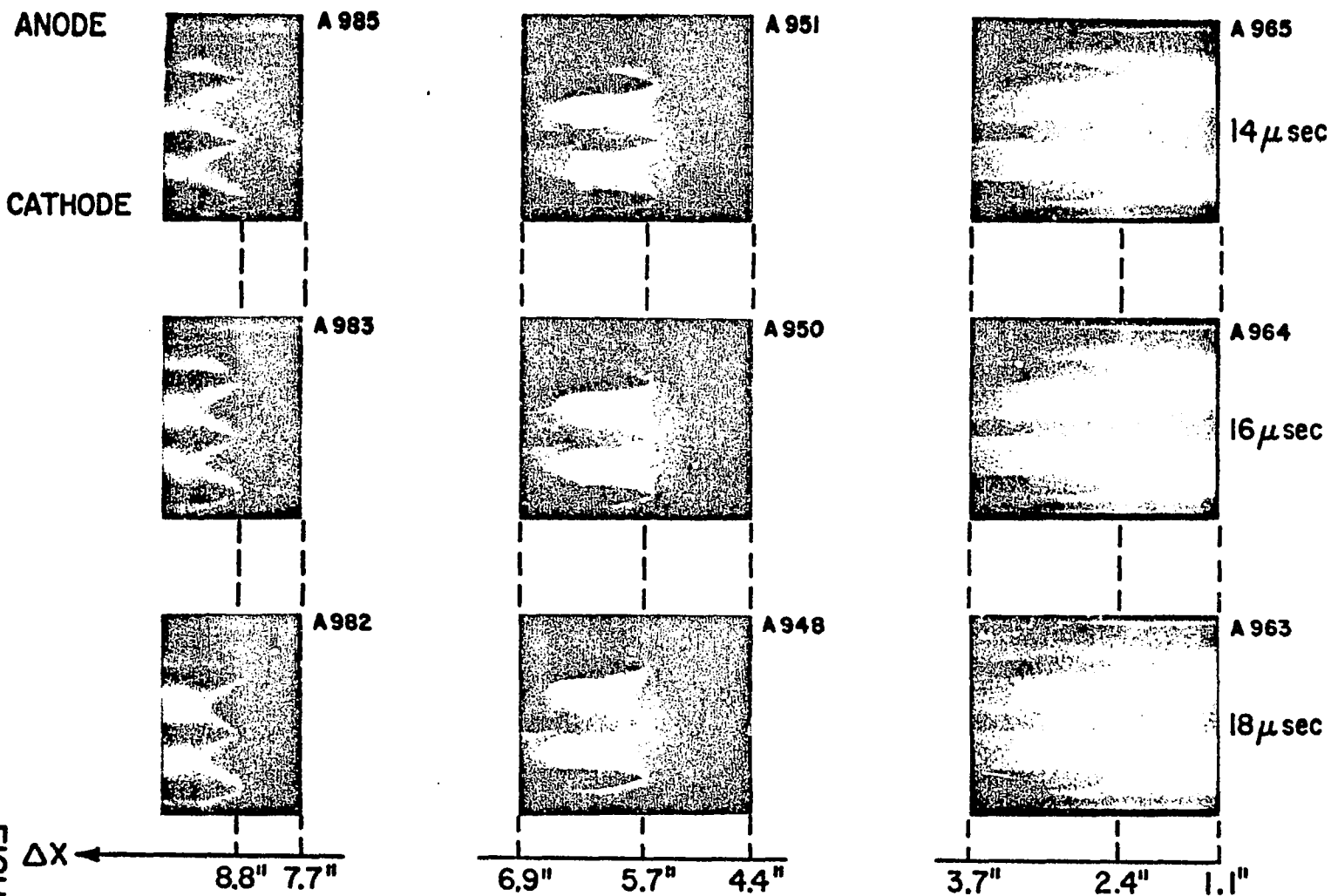
1/4 in. off the anode and cathode and in the midplane, at various axial positions along the channel. For example, the state of the inlet flow to the stabilized current zone can be observed by placing the wedges upstream of the current stabilization region, $\Delta x < 0$. Such a series of pictures taken at 10, 14, and 18 μsec , respectively, is shown in Fig. 6 where the wedge tips are located at approximately $\Delta x = -1 \frac{3}{8}$ inches. Shocks are visible at each of these times indicating that the inflow is supersonic over the stabilized portion of the current pulse. The luminosity of these shocks, however, decreases with time suggesting that the mass flow into the stabilized zone is decreasing. This is to be expected since no external source of mass is available to the discharge. Figure 7 displays the flow over the wedges at $\Delta x = +2 \frac{3}{8}$ in., $+5 \frac{5}{8}$ in., and $+8 \frac{3}{8}$ in. at 14, 16, and 18 μsec into the pulse. Comparing these positions with the patterns of enclosed current shown in Fig. 4 one sees that the above positions correspond respectively to the middle of the stabilized zone, to the downstream edge of the zone and to a completely exterior position. At the three times shown, it is apparent that the Mach number of the flow increases downstream through the stabilized current zone. At the first position, the shocks are somewhat detached; at the second, the shocks are attached, and at the third, they are yet more inclined to the flow. Further interpretation is somewhat ambiguous since either a flow acceleration or a decrease in local sound speed could produce the observed Mach number increase. However, since the effect of joule heating in the current zone would tend to raise rather than lower the sound speed, and since the similarity in probe responses at the three transverse positions speaks against major transverse gradients and excessive wall cooling, a valid flow acceleration through the current zone seems the more likely alternative.

In an effort to unravel a bit more of the mechanisms of



AIRFOIL VISUALIZATION OF GAS FLOW
INTO STABILIZED CURRENT DISTRIBUTION

FIGURE 6

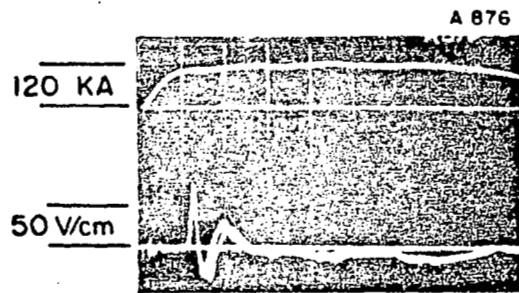
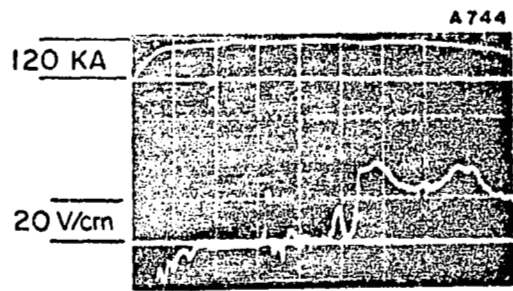
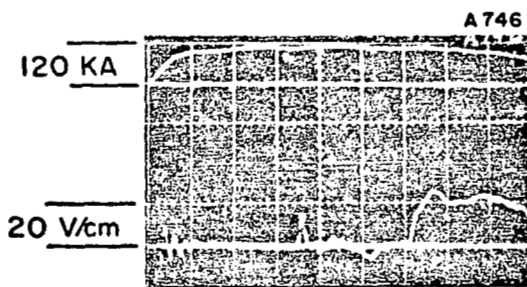
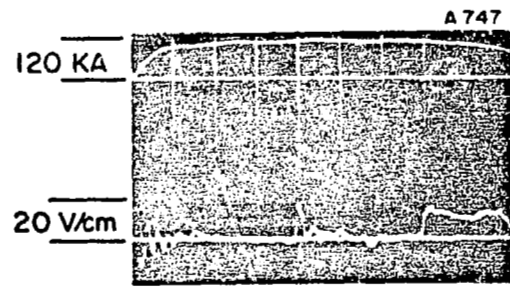
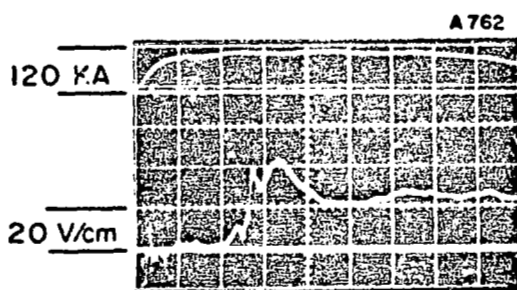
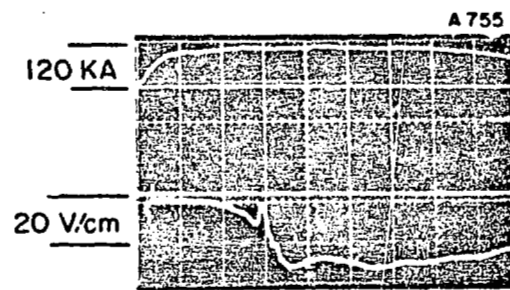


AIRFOIL VISUALIZATION OF GAS FLOW THROUGH
STABILIZED CURRENT DISTRIBUTION

gas acceleration in the two phases, the patterns of streamwise and transverse electric field, E_x and E_y , respectively, within the current-carrying region of the plasma are mapped using floating double electric field probes. The E_x fields are monitored using a coaxial-lead, conically shaped probe similar to that of Burkhardt and Lovberg. The transverse fields, E_y , are measured with a twisted or coaxial lead, straight-tipped probe.

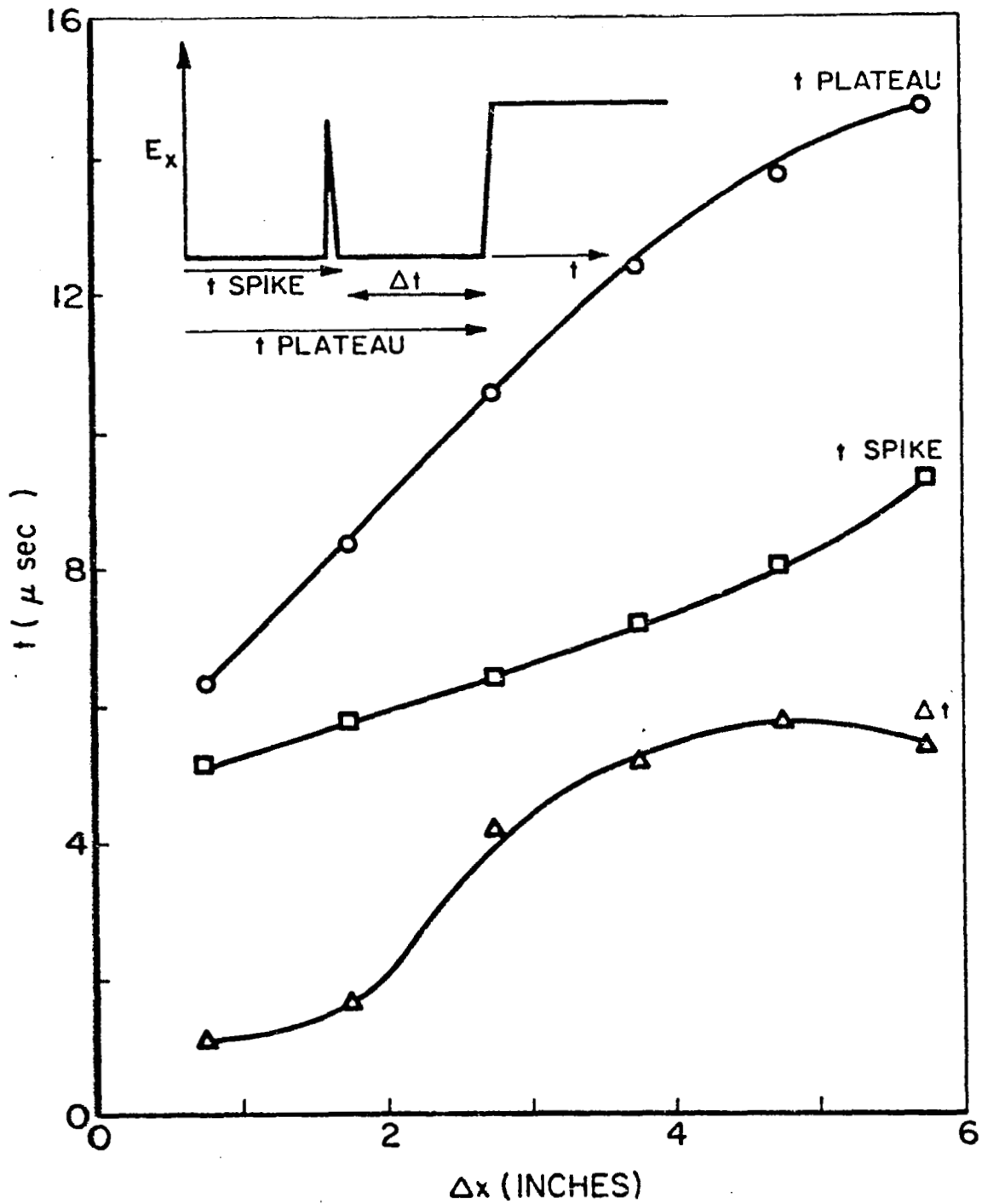
The streamwise probe response along the metal electrode portion, shown in Fig. 8a corresponds to that commonly observed for a propagating current sheet [42,A-1] namely a "spike" of forward facing electric field. In contrast, E_x probe signatures obtained within the stabilized current region, downstream of the metal-to-insulation junction, Figs. 8b,c,d consist of a vestige of the current sheet spike followed by a null period, followed by an abrupt rise to a plateau which lasts nearly to the end of the pulse. The amplitudes of the vestigial spike and of the plateau decrease with distance downstream of the electrode discontinuity. The former tends to decelerate once beyond the discontinuity but the leading edge of the plateau seems to maintain a uniform speed or even to accelerate somewhat as displayed in the trajectories of Fig. 9.

One may speculate that the first spike of E_x recorded by the probe announces the arrival of the snowplowed plasma accumulated by the propagating sheet upstream in the conducting portion of the accelerator, now continuing on its own inertia as the current sheet is arrested at the discontinuity and diffuses into the stabilized current conduction pattern. The plateau of electric field prevailing over the latter portion of the response presumably reflects the quasi-steady flow acceleration process in operation, possibly as a Hall voltage component of the total electric field. The rather well-defined null time between these two signals is somewhat puzzling,

2 μ sec/DIVa) $\Delta x = -3.3''$, MIDPLANEb) $\Delta x = 2.8''$, MIDPLANEc) $\Delta x = 3.8''$, MIDPLANEd) $\Delta x = 4.8''$, MIDPLANEe) $\Delta x = 0.75''$, 0.25" FROM ANODEf) $\Delta x = 0.75''$, 0.25" FROM CATHODE

ELECTRIC PROBE SIGNATURES OF CURRENT SHEET STABILIZATION;
STREAMWISE ELECTRIC FIELD, E_x .

FIGURE 8



TRAJECTORIES OF CHARACTERISTIC FEATURES
OF ELECTRIC PROBE SIGNATURES

FIGURE 9

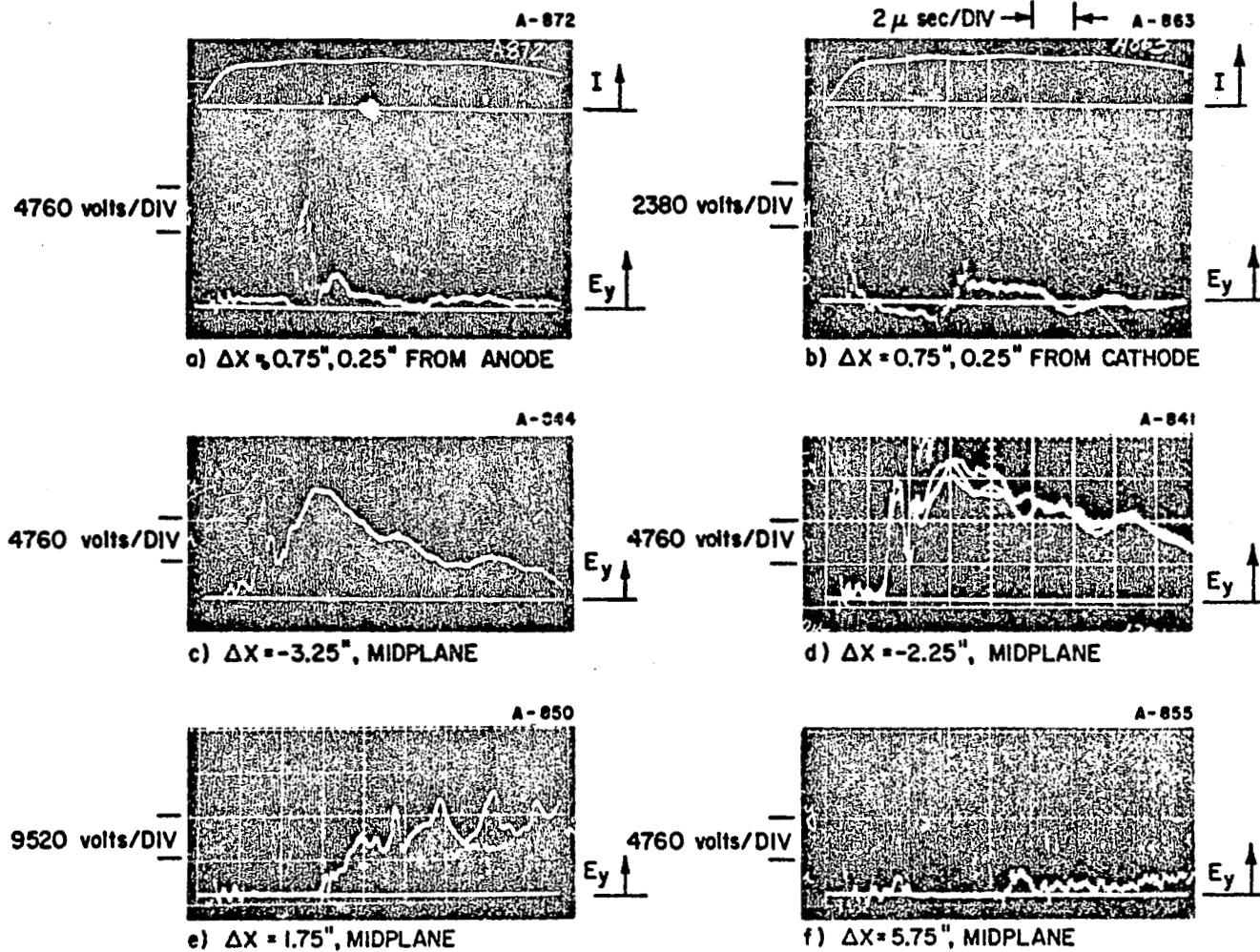
particularly since no correspondingly abrupt processes are evident in the development of the discharge current distribution in this region.

Figure 8e,f display records of E_x obtained by a probe immersed in the conduction bands near the anode and cathode surfaces. Here the E_x field is essentially parallel to the current vector and hence is primarily a resistive component, nearly constant over the lifetime of the steady current pattern and opposite in sign near the anode and cathode. In the stabilized conduction bands, $t > 10 \mu\text{sec}$, E_y virtually vanishes as seen in Fig. 10a,b.

In Fig 10c,d E_y traces along the metal electrodes are shown; these traces rise as the sheet sweeps by and then fall off gradually during the remainder of the pulse. Figure 10e shows the E_y signal in the stabilized zone which, excepting fluctuations, remains relatively constant. The magnitude of E_y in the stabilized zone falls off with distance from the electrode discontinuity going to zero at the end of the stabilized current zone, Fig. 10f.

Magnetic and electric field data like that shown above can be employed in a simplified, but self-consistent one-dimensional model to yield estimates of the salient properties of the flow passing through the stabilized current zone. Details of this analysis are available in Ref. 59; briefly, it is found that the degree of ionization is about 80 percent, the outlet to inlet velocity ratio is somewhat greater than 2, and the mass flow rate over the stabilized phase integrates to about 15 percent of the ambient gas density in the interelectrode gap. The last figure is important in indicating a possible source of mass for the stabilized accelerator, namely gas which has escaped complete entrainment by the propagating current sheet. Current sheets of this intensity, with large anode feet, are known from earlier studies [50] to be "imperfect sweepers" a fact confirmed by the observed magnitude of the

120/20 PULSE, 100μ , $5\frac{1}{4}"$ ELECTRODE LENGTH



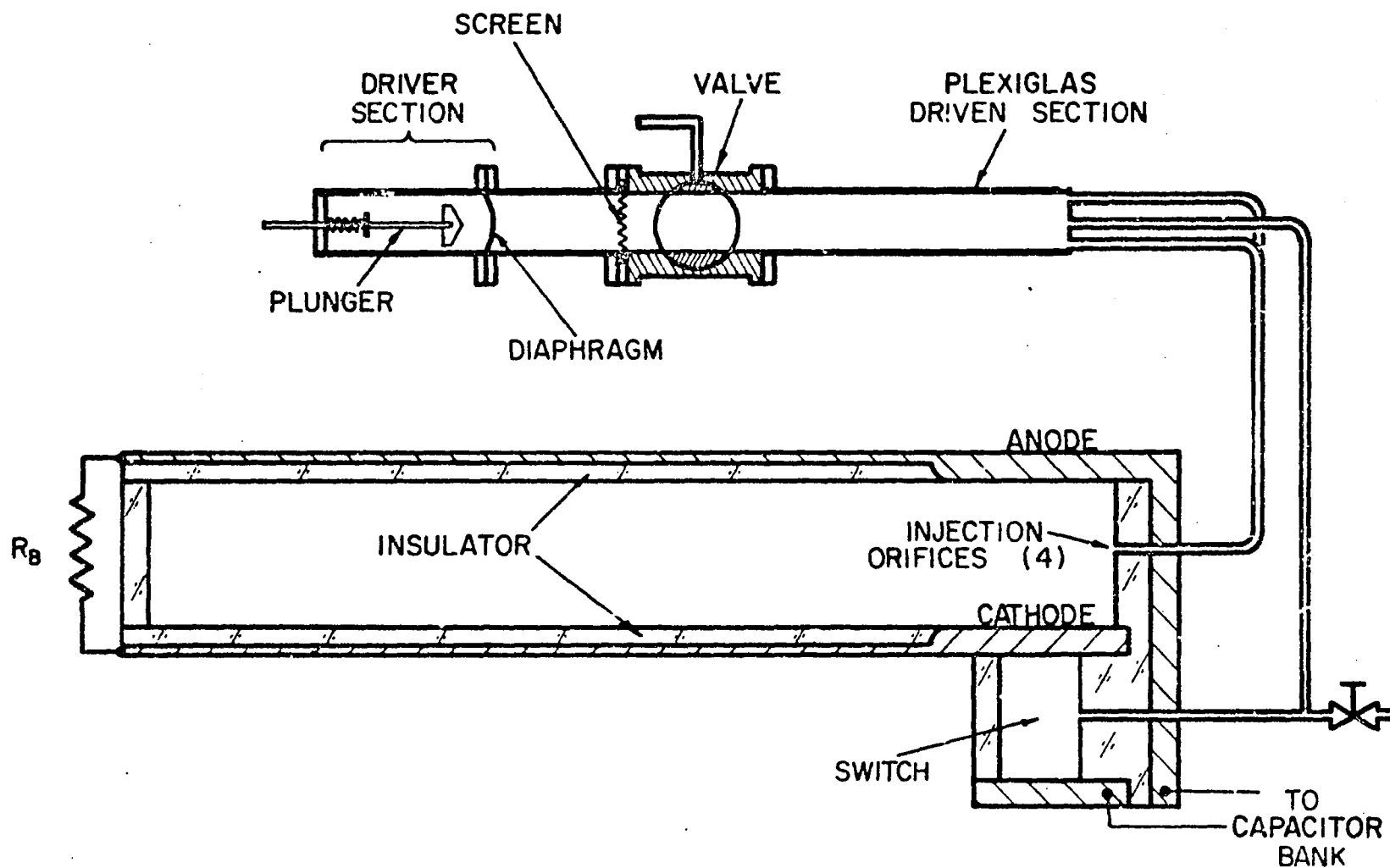
TRANSVERSE ELECTRIC FIELD SIGNATURES

E_x spike too small to account for full acceleration of the ions to sheet velocity. Thus, it appears that the propagating sheet only partially accelerates the ambient gas it passes over, which later surges into and is accelerated by the stabilized current pattern.

Clearly this particular source of mass flow can suffice for only a limited time before becoming exhausted. For longer driving pulses, evidence of a decay in this source should appear in the outflow, and such a tendency is indeed observed in wedge flow studies of a 30/80 current pulse. As this supply is depleted, the discharge impedance should rise and/or new sources of mass must be activated. Evidence is presented below that under these circumstances the discharge increases its voltage to a point where it can ablate sufficient electrode and insulator material to sustain itself on these vapors.

To relieve this mass starvation condition, one naturally turns to an external gas supply of some sort, but here one encounters the inherently slow gasdynamic time scale. Figure 11 displays the shock tube gas injection system developed for the parallel-plate accelerator. Despite the substantially superior rise time of such a system over any mechanical gas valve, it is incapable of getting significant mass to the discharge zone until well over 100 μ sec. For example, although discharges driven by 30/80 current pulses show clear evidences of mass starvation toward the end of their flows, no convincing differences in voltage signatures can be observed between discharges in 100 μ ambient argon, and those provided with shock tube gas injection at the same initial pressure. The interpretation is simply that the available time scale (80 μ sec) is too short for the injection flow to become properly established. Before the externally supplied gas can provide a quasi-steady inflow to the acceleration zone, it must first fill the channel void created by the sweeping current sheet as it propagates to its stabilized position.

FIGURE II



SHOCK TUBE GAS INJECTION SYSTEM

This filling process must require a time of the order of the channel length involved divided by the sound speed of the injected gas, i.e., hundreds of microseconds.

In other words, while it appears that the electrodynamic aspects of steady plasma acceleration, i.e., current pattern stabilization, can be simulated on a time scale of tens of microseconds, attainment of the corresponding quasi-steady gas flow from an external source will require an order of magnitude longer test time. Experiments directed toward achievement of this quasi-steady mode of plasma acceleration are described in the following section.

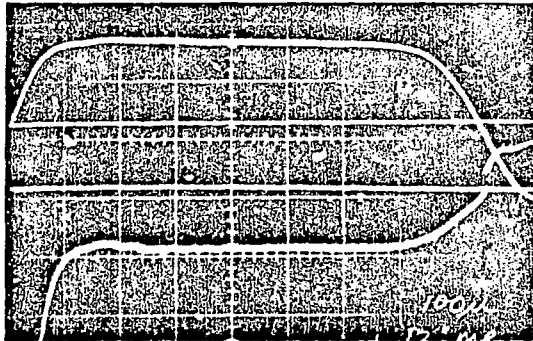
Quasi-steady Plasma Acceleration

Prior to selecting a pulse shape and shock tube configuration for detailed quasi-steady acceleration experiments, a series of tests was performed to determine the minimum time scale over which the appearance of externally injected gas in the discharge could be established. To reduce the interelectrode cavity upstream of the discharge, the electrodes were shortened from 5 1/4 to 2 in., and downstream terminal voltage signatures were recorded for various current pulse lengths in both the ambient fill and injection modes. Figure 12 compares typical ambient and injection responses for three pulses, 20/125, 10/250 and 5/500. The voltage signatures for the 20/125 pulse in the shock tube and ambient cases are nearly identical, indicating that while the shock tube is properly simulating 100 μ initially, it does not succeed in supplying additional mass to the discharge over the balance of the pulse time. For the 10/250 case, however, a difference in the voltage level between the ambient and shock tube cases can be noticed over the latter half of the pulse. The effect is more evident for the 5/500 pulse where the shape of the entire signature is markedly different, and near the end of the pulse the shock tube voltage is nearly 50 percent lower than the

100 μ ARGON

A-1412

I
↑
↓
V



20 μ sec/DIV

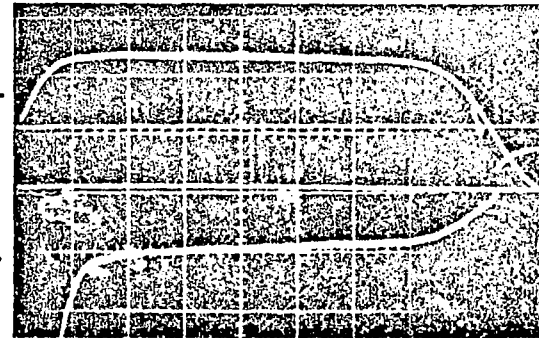
← 20/125 PULSE →

← 100 V/DIV →

SHOCK TUBE INJECTION

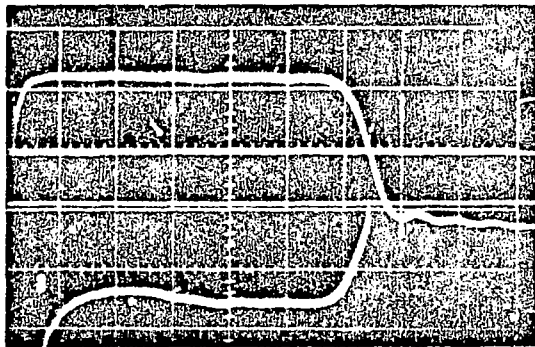
A-1415

I
↑
↓
V



A-1279

I
↑
↓
V



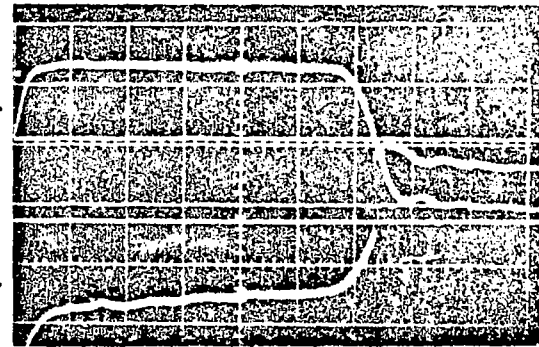
50 μ sec/DIV

← 10/250 PULSE →

← 50 V/DIV →

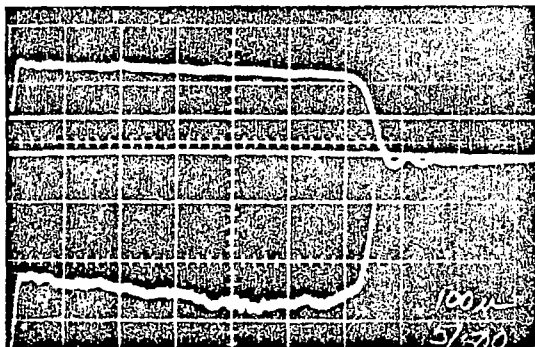
A-1303

I
↑
↓
V



A-1427

I
↑
↓
V



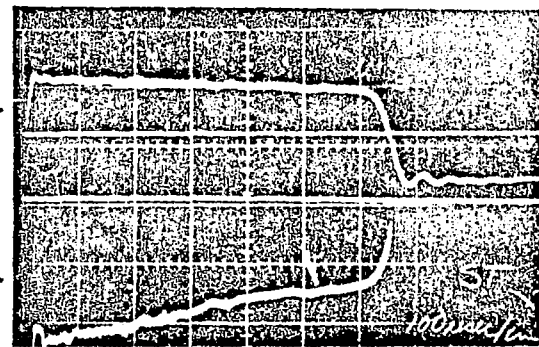
100 μ sec/DIV

← 5/500 PULSE →

← 20 V/DIV →

A-1432

I
↑
↓
V



25

FIGURE 12

VOLTAGE SIGNATURES FOR 2" ELECTRODE LENGTH

ambient value. It seems qualitatively reasonable that the ambient signals should increase with time due to a mass starvation of the discharge, while the shock tube signatures decrease as the injected flow increases the pressure in the discharge region. Based on a series of such studies, it is concluded that an externally supplied gas flow from the existing shock tube injection system can be established at the discharge region for pulse times of 150 μ sec or greater.

To verify that the external flow, which on the basis of the voltage measurements appears to be feeding the discharge, is indeed being accelerated, a small 15° half angle wedge is again placed 2 1/4 in. downstream of the metal-to-insulation discontinuity, hopefully to generate visible bow shocks. Now, however, for the relatively low discharge current amplitudes predicated by the long pulse requirement, the flow luminosities are much less intense, and this technique becomes marginal, at best. For the 5/500 pulse, the luminosity of the flow is too weak to be photographed even with a 5 μ sec Kerr-cell shutter. For the 10/250 waveform, visible bow shocks are found, but only for a narrow range of injected mass flow rate. Above and below this range, and even with 100 μ ambient prefill, no shocks are observed. At their best, the shock waves are rather diffuse, suggesting that the flow is quite rarified in this region. Using highly sensitive piezocrystal pressure transducers and a simple volume filling procedure the mass flow rate to the discharge for which shocks are most discernible is estimated to be 3.6 grams/sec.

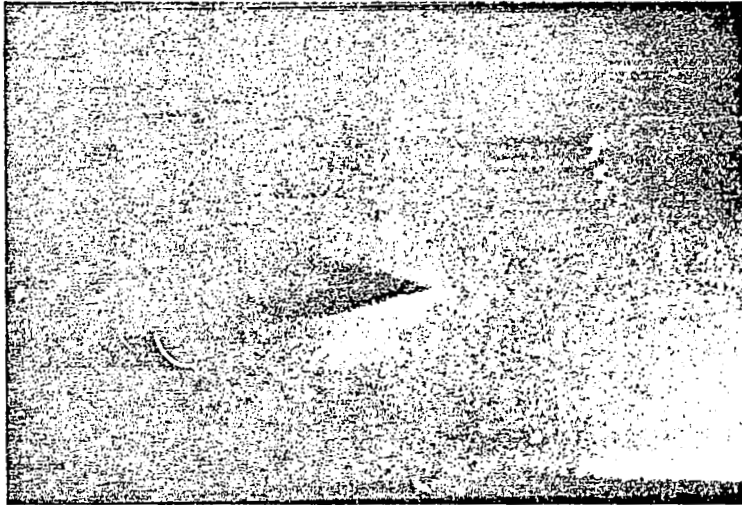
It is apparent from these results that the relatively low current amplitudes available from the fixed energy bank for the long pulse times required for flow establishment are really inadequate to drive this size accelerator in the desired mode and density range. That is, as the injected mass flow, and corresponding gas density in the discharge region are increased into the desired range of operation, the mass overload becomes

too great for the prevailing ionization and electromagnetic acceleration mechanisms, and no viable supersonic outflow is achieved. Various narrower breadth channels have been tried in attempts to increase the discharge current density, but these introduced undesirable field fringing and discharge constriction effects which more than counterbalanced their discharge intensification. Clearly an order of magnitude larger energy source is needed to conduct this experiment properly, and this is presently under construction.

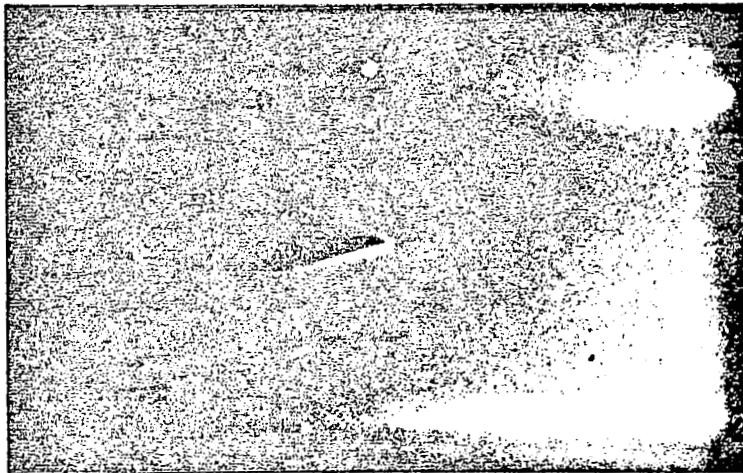
Nevertheless, in the one particular range of mass flow mentioned above, the desired effect has been demonstrated; namely, the device has succeeded in accomplishing the transitions from its initial propagating sheet phase, through an interim phase where it accelerates overrun ambient gas and/or electrode-insulator material, to the quasi-steady phase where it accelerates an externally injected gas flow. To examine this latter phase in more detail, a series of electric and magnetic probe studies have again been performed to map the prevailing field and current distributions. Details of this work, and of the analysis based on it are available in Ref. 59 briefly, it is found that unlike the high-current patterns, which are bowed far downstream, the 10/250 current distribution is nearly one-dimensional, and the streamwise electric field falls to zero upstream of the current density maximum. The analysis then indicates a velocity ratio of about 2.5 across the acceleration zone, and a degree of ionization of about 20 percent within it.

One interesting by-product of the otherwise meager Kerr-cell results of the long pulse discharges has been the revelation of greatly increased luminosity in the anode and cathode jets emanating from the electrode-insulator discontinuities as the mass flow decreases (Fig. 13). It is hypothesized that as the mass flow decreases, the discharge is starved for mass and ablates electrode and/or insulator

$t = 200 \mu \text{sec}$



3.6 g ARGON/sec



1.4 g ARGON/sec

KERR-CELL PHOTOS SHOWING INCREASE IN
INTENSITY OF ANODE AND CATHODE JETS
WITH DECREASING MASS FLOW

FIGURE 13

material to feed itself, with a resulting intensification of the luminosity near the electrode discontinuity. To check this hypothesis, the discharge has been examined spectroscopically for the various mass flow rates available. As the external flow is reduced, there is observed to be a major increase in the intensity of the molecular carbon bands, an increase in the intensity of aluminum lines, and a decrease in the argon line radiation. If one associates the carbon with the organic insulator material, the hypothesis seems at least qualitatively confirmed.

Summary

Based on the experiments described here, the detailed analyses developed in Ref. 59 and earlier work, we may piece together the following picture of the metamorphosis of the plasma acceleration process in the parallel-plate, partial-electrode channel driven by a long current pulse: At breakdown a current sheet is formed near the upstream end of the electrode channel, of width and intensity determined by the rise time and amplitude of the driving pulse. Driven by its own magnetic field, this sheet propagates into the ambient gas, entraining a large fraction of it, but leaving some profile of slower gas in its wake. Upon reaching the electrode-insulator discontinuity, the sheet decelerates rapidly to a stabilized discharge configuration, while some of the gas originally entrained on it continues down the channel on its own inertia. The stabilized discharge, whose particular configuration again depends on the amplitude of the driving current, is now fed from the upstream side by the slower gas left behind the current sheet, which gas it accelerates through itself in the classical self-field Lorentz mode to a velocity that maintains the terminal voltage the same as the transient-phase value. In the absence of another source of mass, the discharge eventually exhausts this reservoir of overswept gas,

and begins to vaporize insulator and/or electrode material to maintain itself, much like a "vacuum arc." This phase is characterized by increased luminosity of the anode and cathode jets, and an increase in arc voltage. If an external mass source is provided, it must first refill the channel upstream of the stabilized discharge before any quasi-steady inlet flow to the discharge region can be established. This is a relatively slow process, and depending on particular channel dimensions and injection procedures, may take 100 μ sec or more. Once such inlet flow is established, however, the discharge voltage drops, erosion luminosity is sharply reduced, and the accelerator operates on the injected mass flow in the same quasi-steady, self-field mode.

III. QUASI-STEADY PLASMA ACCELERATION (Clark)

Stabilization of the discharge current patterns of pulsed plasma accelerators into steady diffuse phases for pulse lengths above a few microseconds has been demonstrated for several electrode geometries both in this laboratory, and elsewhere [57,A-2]. Study of this "quasi-steady" phase for an electrode configuration resembling the steady state magneto-plasmadynamic arcjet is attractive from several points of view. First, such quasi-steady operation permits application of transient diagnostic techniques within the arc chamber and exhaust plume, environments normally too hostile for detailed study in the steady state. Second, the quasi-steady experiment permits extension of MPD operation to multi-megawatt power levels inaccessible in steady state experiments because of heat transfer, power supply, and gas handling limitations. Such high power operation is of basic interest because the overall efficiency of the MPD arc has been observed to improve as the power level is increased, and may also be instructive for advanced mission studies. For example, certain projections of manned missions to the near planets favor propulsion system power in the range of 1 - 10 MW; quasi-steady MPD studies may provide an initial hint on the feasibility of single thruster operation in this range. Finally, and perhaps most important, the quasi-steady acceleration mode may prove to be an interesting propulsion technique in its own right. In particular, it is possible that intermittent long-pulse operation may combine the benefits of high power MPD operation with tolerable average power consumption and simple variable thrust capability via duty cycle adjustment.

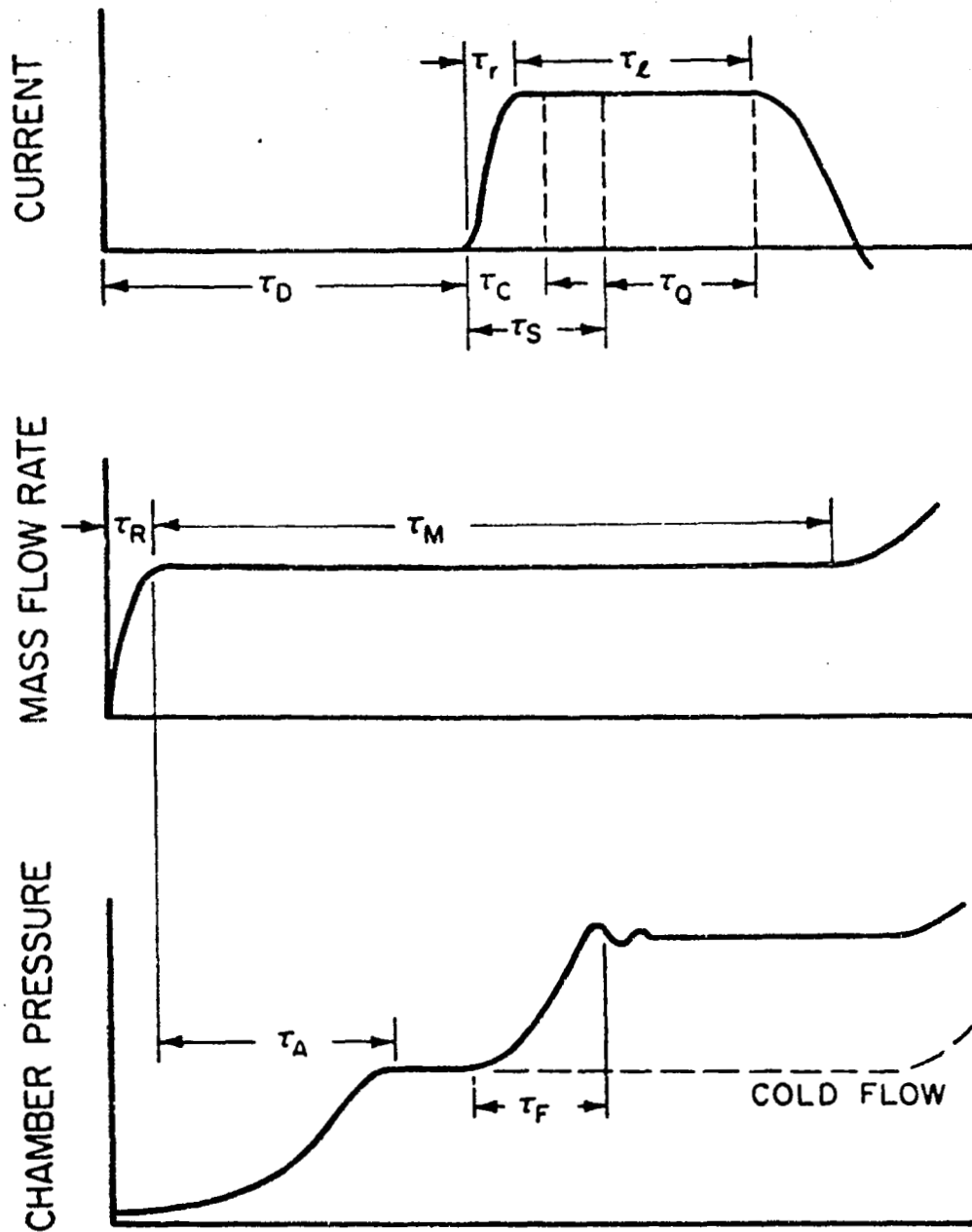
Experimental Design

Proper quasi-steady operation requires rather precise correlation of the injected mass pulse with the applied current

pulse. With reference to Fig. 14 the injected mass pulse must rise quickly (τ_R) to a steady value, and remain as that value until after the current pulse has been completed (τ_M). The current pulse cannot be initiated until the chamber pressure has reached a steady value corresponding to the injected mass flow rate, (τ_A), but this time must be sufficiently short that the vacuum tank back pressure is not compromised by the pre-discharge flow. After the appropriate delay (τ_D) the current pulse is triggered, rising quickly (τ_r) to some steady value, and lasting for a time characteristic of the current source (τ_I). Before the arc discharge can be considered to be operating as a true quasi-steady accelerator, the chamber pressure must readjust to its "hot" operating condition, (τ_F), the exhaust plume must reach some stabilized current density pattern (τ_s) and the cathode must attain steady thermionic emission (τ_C). If these several time constants are of commensurate magnitudes and the various events are properly synchronized, there remains an interval (τ_Q) during which reasonable simulation of steady operation should prevail.

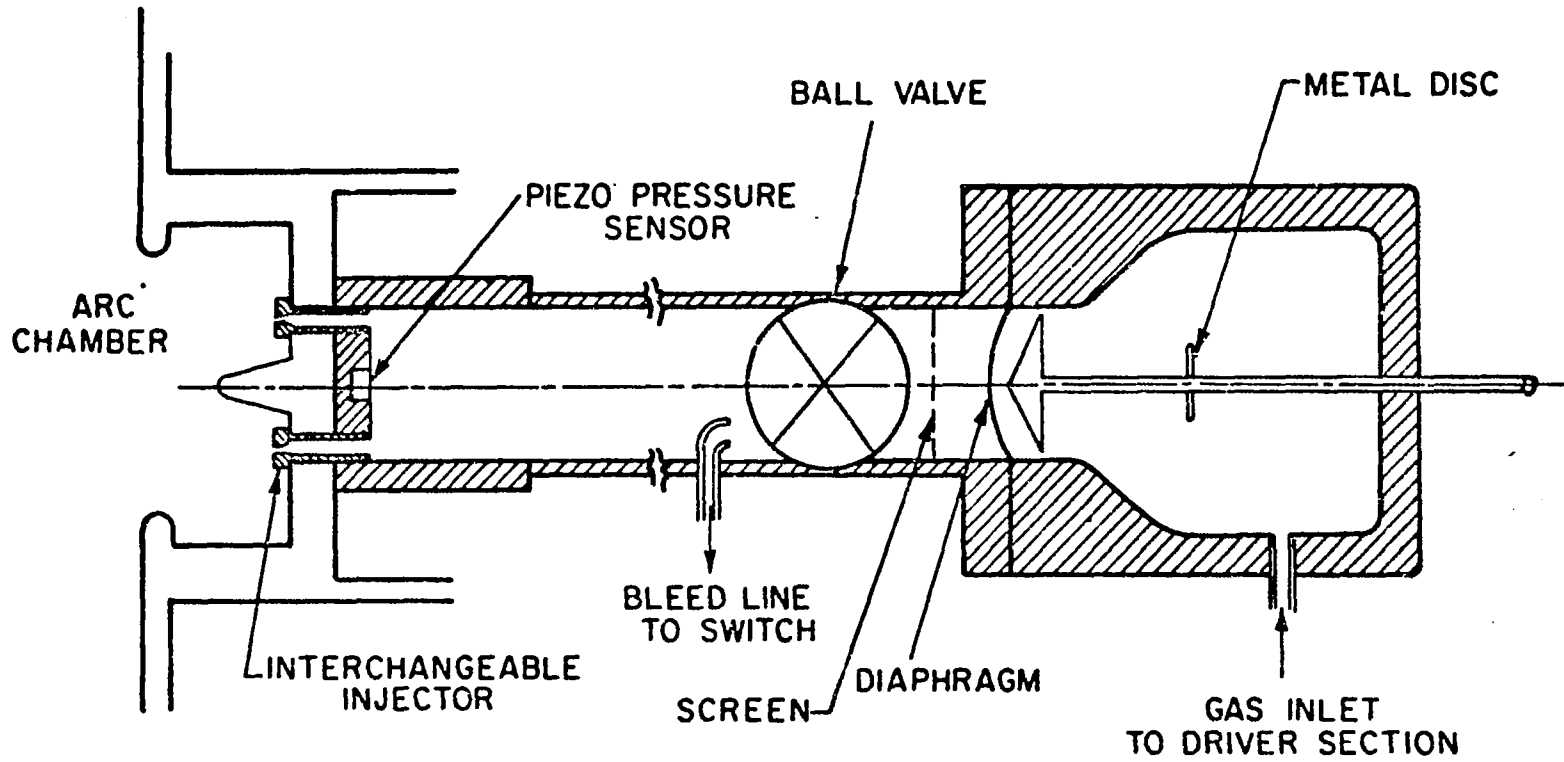
In the experiment described here, the driving current pulse is provided by a bank of 40 x 3.2 μ F capacitors arranged in an LC ladder network. Varying the interstation inductance yields a variable amplitude, variable length pulse covering the range from 140 kA x 20 μ sec to 4.4 kA x 600 μ sec. A separate gas-triggered, closed-chamber discharge switch [16] transfers the 10 kV bank voltage to the electrode assembly.

A shock tube is used to provide the tailored mass injection pulse. As seen in Fig. 15 this tube is mounted directly behind the arc chamber with six interchangeable injection tubes connecting the end of the Plexiglas driven section to the discharge chamber. The tube is not operated in the conventional manner in the sense that the driven section is not maintained at a continuum pressure level, but is pumped out to the back pressure of the vacuum tank (about 10^{-5} torr).



CHARACTERISTIC TIMES FOR CURRENT
PULSE AND MASS FLOW

FIGURE 15



34

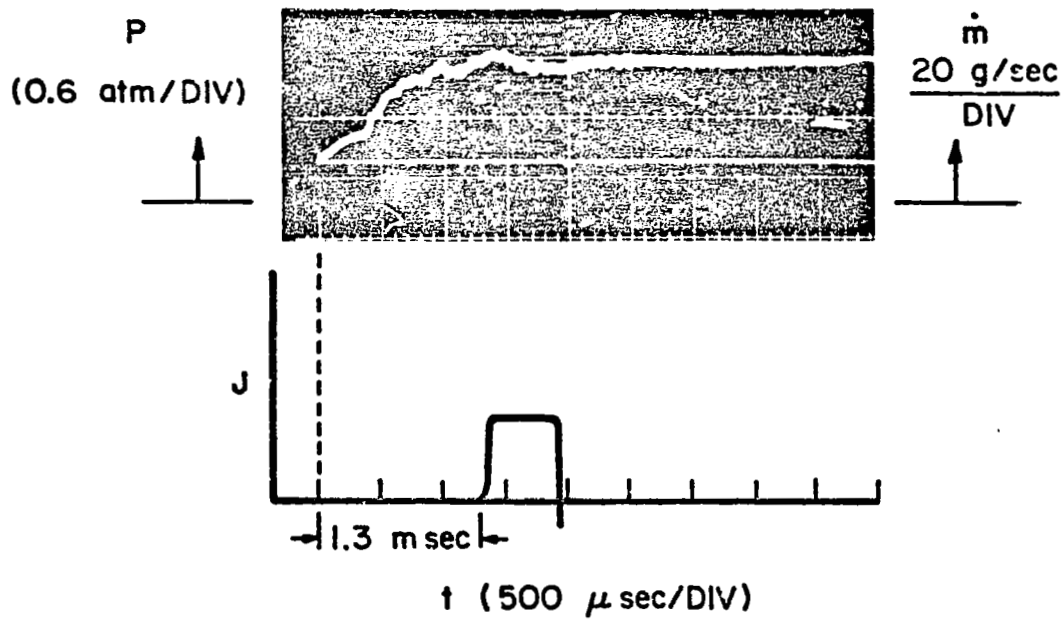
SCHEMATIC OF MASS INJECTION SYSTEM

The driver section is normally pressurized to 35 psia. Upon rupturing the diaphragm, the pressure history at the driven section end wall and thus the mass injection history, is formed by the superposition of the initial diffuse compression, the rear portion of the initial rarefaction wave which is convected downstream, and the reflection of the rarefaction head off the driver end wall. The tube length is therefore kept relatively short to reduce the time to attain steady end wall pressure. The particular configuration shown, consisting of a driven section 30-in. long by 2 3/8-in. i.d., and driver section 6-in. long by 4 3/4-in. i.d. is capable of providing mass flow rates up to 50 g/sec for 3 msec, with a rise time of about 1 msec.

A piezoelectric pressure sensor is mounted in the driven section end wall to monitor end wall pressure time history and to provide a time mark for synchronizing the mass and current pulses. The gas-triggered switch is supplied by a bleeder tube from the upstream portion of the shock tube channel. Adjusting the length and size of this line controls the discharge delay time (τ_D).

Figure 16 shows a typical trace of the end wall pressure history compared with the arc current. In this particular case, the mass flow rate reaches a level of about 36 g/sec after 1 msec. The discharge is triggered at roughly 1.3 msec, a time verified to be sufficiently long to allow the chamber pressure to reach an equilibrium value. Although the capacitor line rings down in a fashion characteristic of its mismatch to the load, only the first half-cycle is employed in this experiment.

Proper simulation of steady MPD operation also involves replication of the essential features of the arc chamber geometry. Based on the typical configuration of a central, conically-tipped cathode, a pierced anode slightly downstream and coaxial with it, and axial gas injection upstream of the electrode gap, there remains only the choice of absolute dimensions



SYNCHRONIZATION OF CURRENT PULSE
TO INJECTED MASS PULSE

FIGURE 16

on the basis of some appropriate scaling criterion. For this purpose, one might require duplication of the thrust density, which for a given specific impulse implies equal power density and mass flux density, or, alternatively, a magnetic interaction parameter might be invoked. Actually, these two approaches yield essentially the same conclusion, by virtue of the familiar relation between the arc current and the total electromagnetic thrust [53]

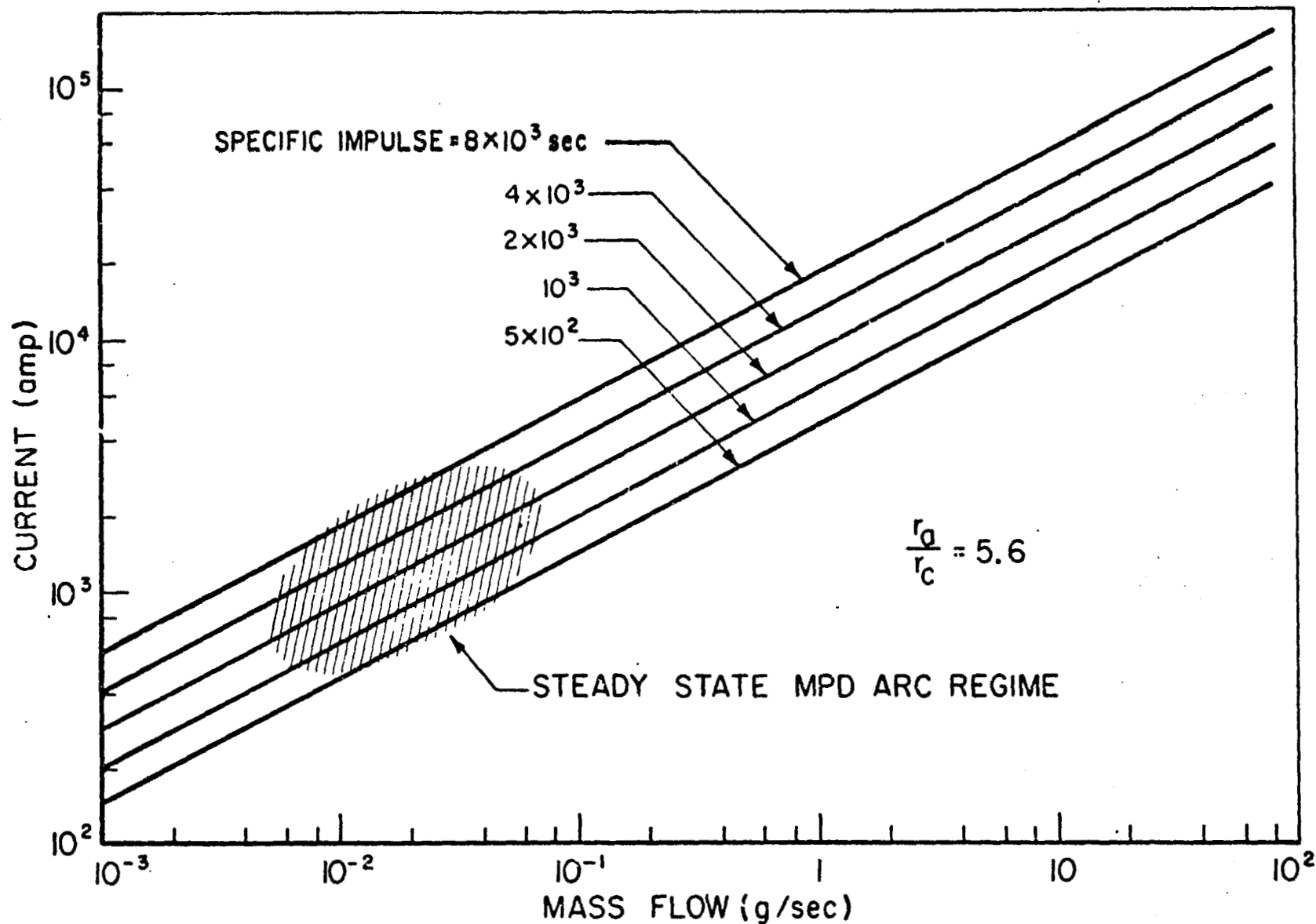
$$T = \frac{\mu J^2}{4\pi} \left[\ln \left(\frac{r_a}{r_c} \right) + \frac{3}{4} \right] = \dot{m} I g \quad (3-1)$$

where T = thrust
 J = total current
 r_a, r_c = effective radii of discharge attachment
 on anode and cathode
 \dot{m} = mass flow rate
 I = specific impulse
 g = sea level gravitational acceleration

That is, for a given specific impulse, the thrust density, mass flux density, and power density all scale as $(J^2/A) \ln(r_a, r_c)$. Presuming the insensitive logarithmic factor to be approximately matched by retaining the same ratio of anode orifice to cathode diameters, the absolute values of these radii should thus be scaled linearly with the discharge current. Since we choose to cover the current range from 4,000 to 140,000 amp, compared to the 2,000 to 4,000 amp range of steady devices, their typical anode orifice radius of 1/4 in. should here be increased by about one order of magnitude. The selected value of 2 in. actually permits study of substantially higher ranges of thrust density than attainable in the steady accelerators.

The thrust relation (3-1) is plotted in Fig. 17 in a slightly different form to display the corresponding mass flow rates required to achieve the interesting specific impulse range for these large currents. For the chosen anode radius,

FIGURE 17

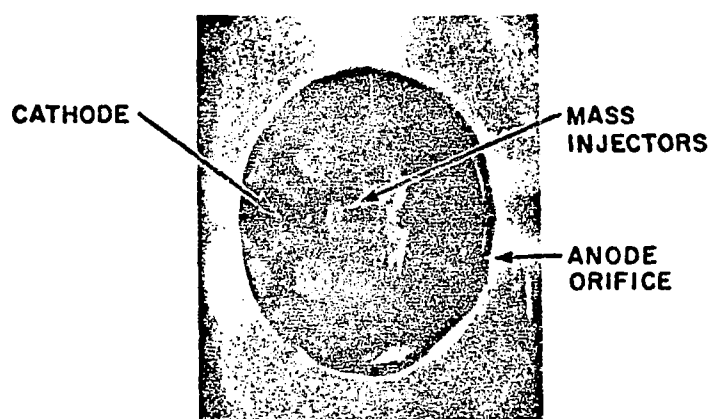


MASS FLOW FOR PURELY ELECTROMAGNETIC THRUST

these transcribe into mass flux densities from 0.10 to 4.30 $\text{kg/m}^2 \text{ sec}$, a range which overlaps and extends the steady flow range of 0.15 to 2.00 $\text{kg/m}^2 \text{ sec}$.

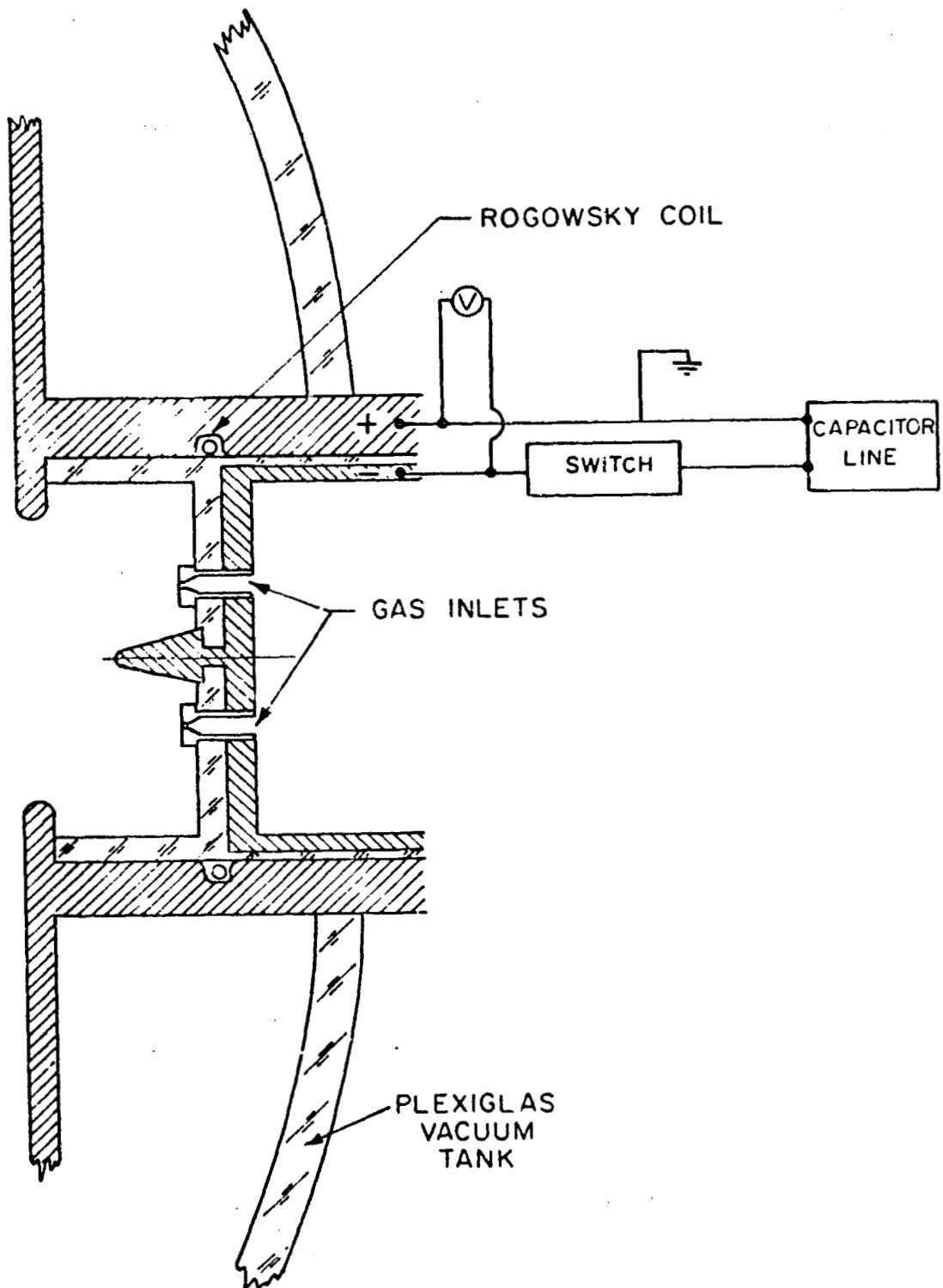
The outer face of the anode is allowed to extend almost to the vacuum tank wall, a radius of 17 in., so as not to inhibit the exhaust plume growth and thus raise the anode fall voltage [54]. The 2 percent thoriated tungsten cathode has a 3/4-in. diameter base and extends 1 in. into the arc chamber. A photograph of the chamber showing the cathode, injector plugs, and part of the anode is displayed in Fig. 18. The assembled chamber and mass injection system are installed in a 3-ft. diameter x 6-ft. long Plexiglas vacuum tank [40]. Before each shot the tank is evacuated to less than 10^{-5} torr, at which pressure the mean free path of the resident particles is considerably larger than the tank dimension.

The operation sequences of the system begin with pressurization of the shock tube driver to 35 psia, and charging of the capacitor line to 10 kV. The diaphragm is then ruptured with a springloaded blade. The pressure wave propagating down the tube is first sampled by the small bleed tube which begins filling of the gas-triggered switch, and then is recorded by the end wall piezocrystal. This signal triggers an oscilloscope to display the delay time until switch break down and discharge initiation on a record of the integrated response of a Rogowski coil enclosing the chamber as shown in Fig. 19. A typical oscillogram is shown in Fig. 16. The Rogowski coil also triggers a second oscilloscope which sweeps at a much faster rate and monitors other diagnostic measurements, such as the electrode voltage, magnetic probe signatures, etc., during the first half-cycle only. To prevent spurious electromagnetic noise from distorting these traces, the oscilloscopes are enclosed in a screen room which is grounded to the anode by a 3-ft. wide by 15-ft. long copper ground plane. All leads from the Rogowski coil, voltage probe, and piezocrystal are dressed closely to this ground plane.



DISCHARGE CHAMBER

FIGURE 18



ELECTRICAL SCHEMATIC

FIGURE 19

Luminosity Patterns

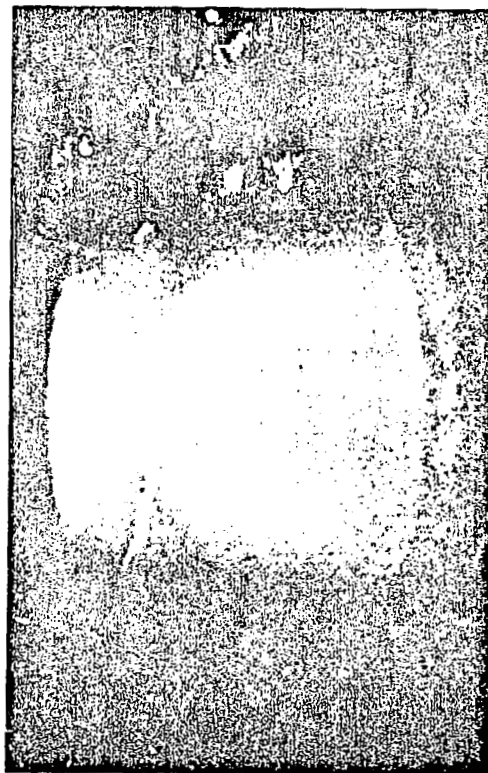
Sample photographs of quasi-steady discharges in argon are shown in Fig. 20. These photographs, taken through a 5 μ sec Kerr-cell shutter, display luminosity patterns for three different mass flow rates at a common current level of 17.5 kA. With reference to Fig. 17 these discharges represent conditions of mass starvation ($\dot{m} = 1.2$ g/sec), mass overfeed ($\dot{m} = 36.0$ g/sec), and mass flow approximately appropriate to the anticipated specific impulse for argon ($\dot{m} = 5.9$ g/sec). Just as in these photographs, over the entire range of conditions tested (mass flow rate from 1.2 g/sec to 36.0 g/sec and current from 4.4 kA to 138 kA), the discharge is invariably axisymmetric with no evidence of spoking. Note also the sharp demarcation between dark and light at the upstream edge of the luminous patterns, particularly in the tightly confined portion near the cathode tip. The effect is most pronounced for the low mass flow rate, and is not readily correlated with any features of the current density patterns discussed later. In general, it is found that the characteristics of such photographs are typical of the mass starvation or overfeed conditions, regardless of the current level, i.e., it is the combination of current and mass flow rate which influences the discharge appearance rather than either separately.

Terminal Voltage

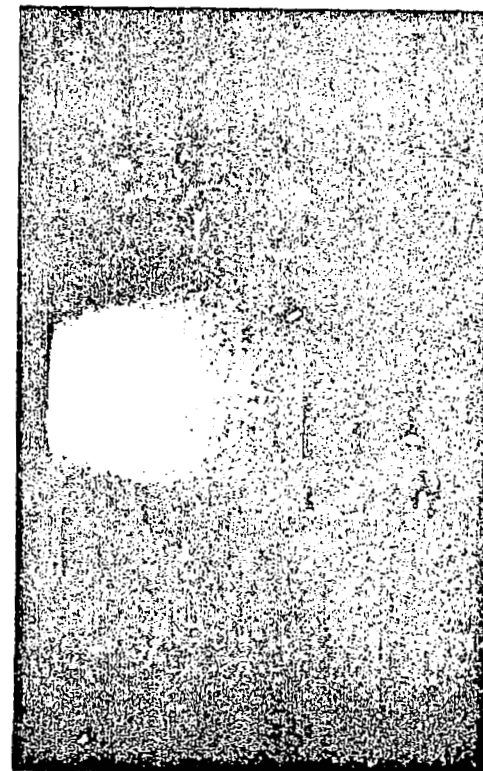
The measurement of total voltage across the discharge chamber is instructive for several reasons: first, the effectiveness of the electromagnetic acceleration process should be reflected in a $\vec{u} \times \vec{B}$ or back emf component. Second, little is known about the resistive component of discharge voltage at current levels above 10^4 amp. In the past, voltage measurements have been used extensively in steady state experimentation to compare arc performance with theoretical acceleration models. Figure 21 displays a typical voltage-current trace for the 17.5 kA



$\dot{m} = 1.2 \text{ g/sec}$



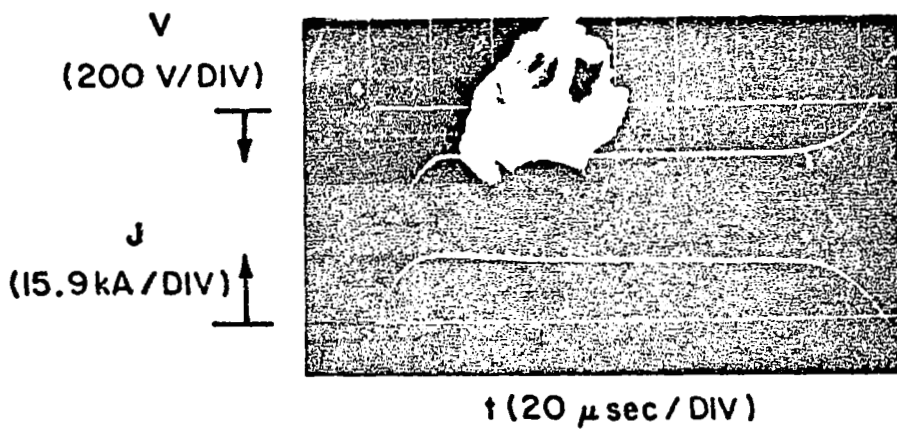
$\dot{m} = 5.9 \text{ g/sec}$



$\dot{m} = 36.9 \text{ g/sec}$

STABILIZED EXHAUST LUMINOSITY AT 17.5 kA

FIGURE 20



TYPICAL VOLTAGE AND CURRENT TRACES

pulse and an argon mass flow rate of 3.8 g/sec. The slight droop in the current is due to the time constant of the integrating circuit; larger time constants yield perfectly flat profiles, but have less sensitivity. Note the sharp drop in the voltage signal at the beginning of the pulse from the applied 10 kV to about 180 volts. This is interpreted as signifying the attainment of thermionic emission by the cathode, since any other mechanism would require substantially higher voltages to support this current density. Steady voltage traces of this sort are observed over the entire range of current and mass flow operation. Figure 22 summarizes these data. The reproducibility for each point is indicated by a small vertical line, if this exceeds the symbol size.

These raw voltage data show the general trends of decrease with mass flow, and increase with discharge current anticipated from the electromagnetic thrust model. Precise correlation is difficult because of inadequate knowledge of the various power loss mechanisms acting in the discharge. Specifically, the measured voltage must reflect not only the electromagnetic acceleration process, but also the energy transfer to the electrode surfaces via their respective falls, and the electrothermal deposition into the gas stream via joule heating in the body of the discharge, i.e.,

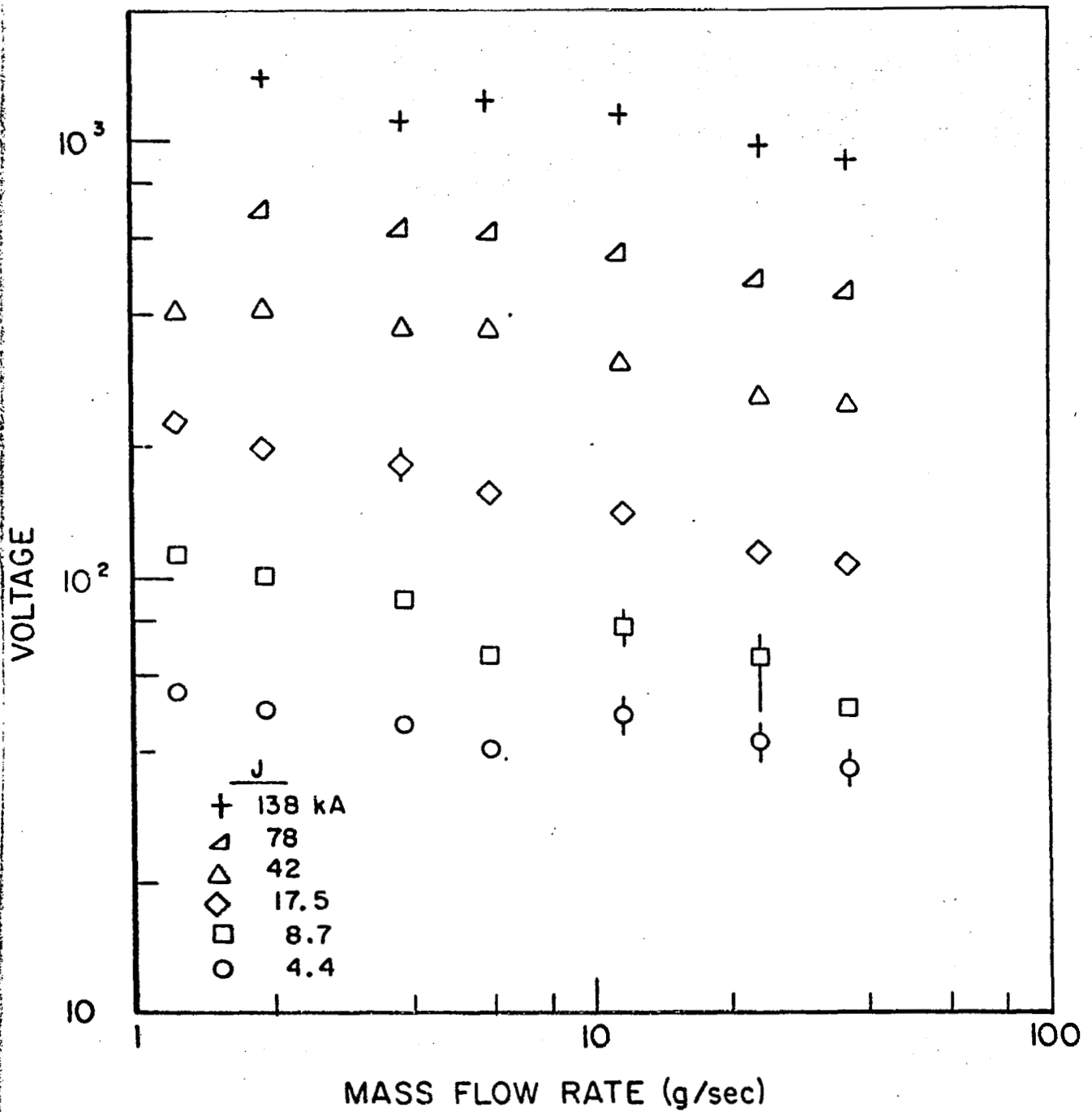
$$V = V_b + V_a + V_c + V_t \quad (3-2)$$

where $V_b = \frac{\text{electromagnetic thrust power}}{\text{discharge current}} =$

$$\frac{T^2}{2mJ} = \frac{\mu^2 J^3}{32\pi^2 m} \left(\ln \frac{r_a}{r_c} + \frac{3}{4} \right)^2 \quad (3-3)$$

$$V_a = \frac{\text{power to anode}}{\text{discharge current}} \quad (3-4)$$

$$V_c = \frac{\text{power to cathode}}{\text{discharge current}} \quad (3-5)$$



SUMMARY OF VOLTAGE MEASUREMENTS

FIGURE 22

$$V_t = \frac{\text{electrothermal power to gas}}{\text{discharge current}} \quad (3-6)$$

The magnitudes of V_a , V_c , and V_t , and their dependence on \dot{m} and J are poorly known. It seems reasonable that V_c should be slightly higher than the work function of tungsten, say ~ 5 volts, a value consistent with electric probe studies of similar discharges in this laboratory (cf. Sec. VI). These same studies indicate anode falls in the vicinity of 15 volts up to currents of 300 kA. The dependence of V_a and V_c on \dot{m} and J , although not yet studied in detail, appears to be weak.

The electrothermal power input encompasses the ionization of the flow, and all internal excitation, random thermal, and radiation processes which attend it. Some of this input may be recovered as useful thrust by electrothermal conversion in the exhaust plume and the remainder constitutes a frozen flow loss; the distinction is immaterial so far as the contribution to the terminal voltage is concerned. It is common practice in estimating the electrothermal voltage to assume that the ionization potential effectively limits the temperature of the particulate species in the plasma, and even to make the approximation that the sole significant energy sink is the single ionization of each incoming particle:

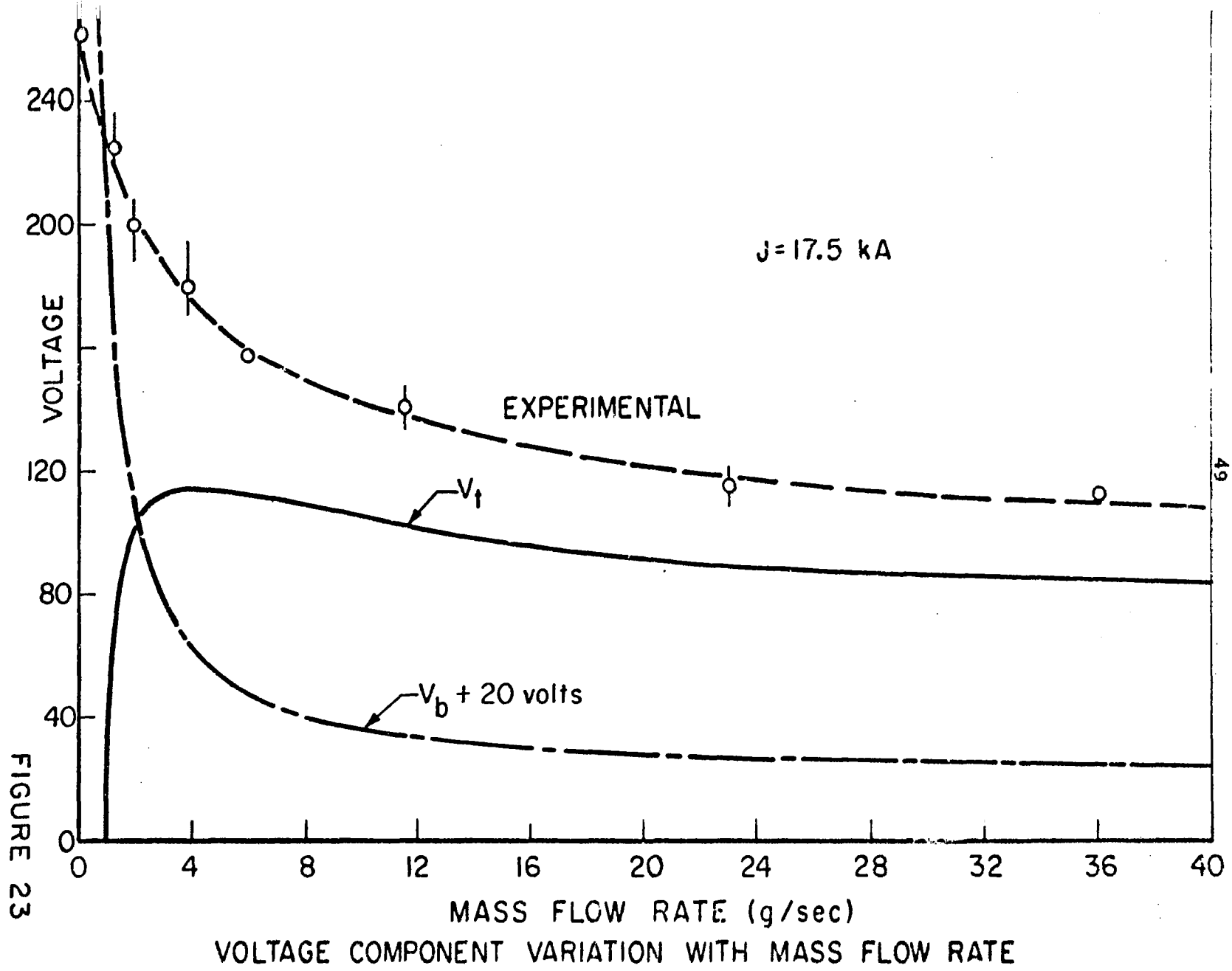
$$V_t \approx \frac{\dot{m}}{M} e \epsilon_I / J \quad (3-7)$$

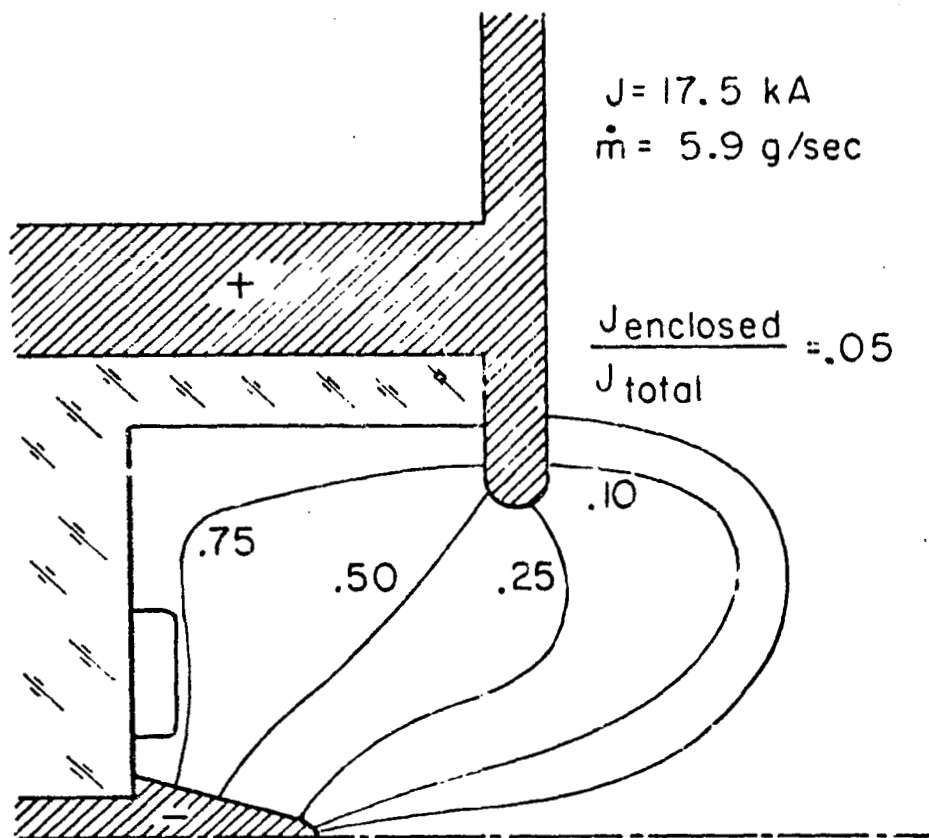
where M is the atomic mass, e the electronic charge, and ϵ_I the first ionization potential. A second approximation to this approach inserts a constant factor to cover the excitation, radiation, and random thermal modes that accompany this ionization level. The significant element in either formulation is the linear coupling of V_t to the mass flow, and this feature is clearly denied by the total voltage data of this experiment.

Figure 23 shows the experimental data for $J = 17.5$ kA compared to calculated values of V_b , corrected by $V_a + V_c = 20$ volts. The difference curve, which must be V_t , rather than increasing linearly with \dot{m} , reaches a constant asymptote, \hat{V}_t , implying no further thermal input regardless of the increase in mass flux. Similar behavior is found at all other currents studied, with \hat{V}_t increasing linearly with current at a slope of 4.5 volts/kA, i.e., in this domain the plasma has become ohmic, with a fixed resistance of 0.0045 ohm.

Current Density Distribution

Enclosed current contours in the exhaust plume and discharge chamber are mapped with standard magnetic probes of #38 Formvar wire, oriented in the r, z plane. Their integrated signatures present local time histories of the azimuthal magnetic field; cross plotting then yields the spatial distribution of the field at any given time, which, presuming azimuthal symmetry, is directly proportional to the fraction of the discharge current enclosed by a circle at the given radius. In operation, four probes, mounted on a movable carriage within the exhaust tank, are positioned remotely between each of a sequence of discharges to accumulate the necessary matrix of data. Figure 24 displays a typical map of the enclosed current contours in the chamber and near-exhaust for a quasi-steady condition. Although all of the stabilized current distributions closely resemble that shown in Fig. 24 a few characteristic tendencies are noted. First, for conditions of mass overfeed, regardless of the level of current or mass flow rate individually, given contours are withdrawn slightly upstream into the chamber; for mass starvation, the contours are slightly more extended downstream into the plume. Second, no more than 50 percent of the total current ever projects outside the orifice; except for starvation cases, only about 25 percent extends out the orifice. In all quasi-steady conditions, no significant amount of current extends farther than





STABILIZED CURRENT DISTRIBUTION

FIGURE 24

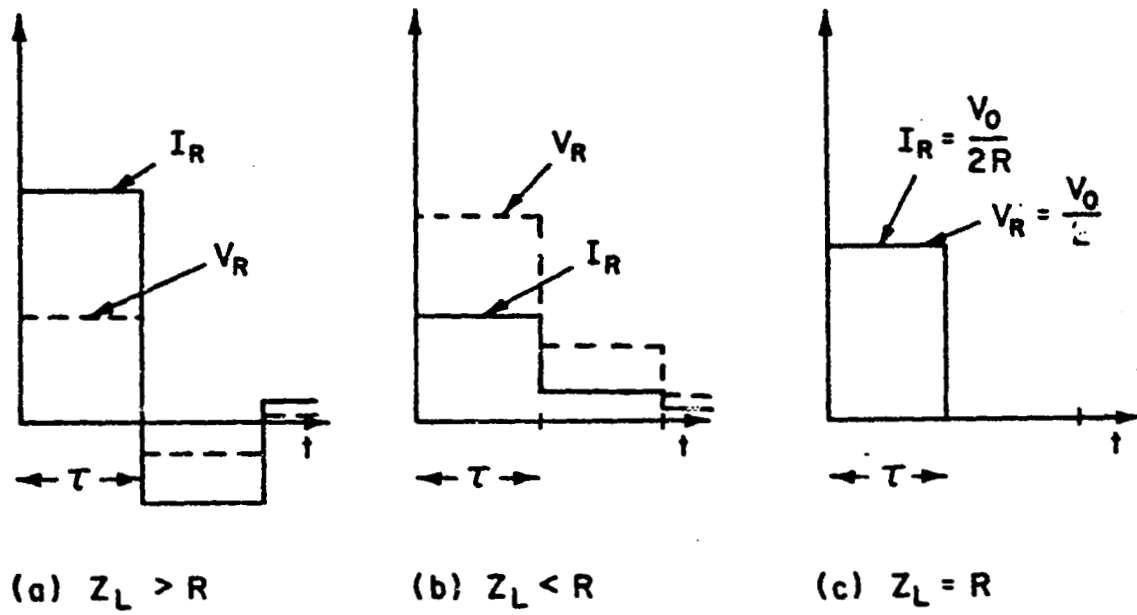
one orifice diameter outside of the orifice, either radially or axially. Third, the bulk of the current does not coincide with the luminosity patterns, such as those shown in Fig. 20. This is in contrast to most pulsed plasma accelerators where the luminosity provides a very good indication of the maximum current density location. Fourth, in all cases studied, the current attachment on the cathode completely covers the surface, i.e., the effective radius of attachment for purposes of relation (3-1) is the maximum material radius. Finally, for all cases of normal mass flow or mass overfeed, the current distribution on the cathode is approximately uniform; for conditions of mass starvation, this distribution becomes more peaked toward the cathode tip.

IV. ENERGY TRANSFER FROM A PULSE NETWORK TO A PROPAGATING CURRENT SHEET (Wilbur)

The purpose of this study is to identify and examine certain factors affecting the efficiency of conversion of electrical energy into thrust energy for a pulsed plasma accelerator. Within the scope of this investigation, no attempt has been made to deal with realistic space hardware, or to optimize overall system performance. Rather the effort has been confined to matching a particularly simple and well understood accelerating discharge, the large radius linear pinch, with a pulse power source of conveniently variable characteristics, in this case a lumped element, low impedance pulse line.

In most conventional power systems, optimum energy transfer efficiency is achieved when the impedance of the load is equal to that of the power source. For example, consider the transfer of energy from an ideal transmission line, initially charged to a voltage V_0 , to a resistance connected across its terminals. The transmission line may be characterized by an impedance $Z_L = \sqrt{L'/C'}$, and a pulse duration $\tau = 2l\sqrt{L'C'}$, where L' is the inductance per unit length and C' the capacitance per unit length of a line of total length l . The qualitative behavior of the current through and voltage across the resistor is shown in Fig. 25 for three relative magnitudes of resistance and characteristic line impedance. For $Z_L > R$, current oscillates back and forth through the load, and several characteristic times are required to achieve substantial energy transfer to the load. For $Z_L < R$, charge is only incompletely removed from the line in the first pulse increment, and several additional wave reflections from the line terminals are needed to complete the energy transfer. Only in the matched case, $Z_L = R$, is all of the energy initially stored in the transmission line transferred to the resistor in one pulse time τ .

FIGURE 25



TRANSMISSION LINE DISCHARGING THROUGH
A RESISTIVE LOAD

If the simple resistive load is replaced by a pulsed plasma accelerator, one might similarly expect optimum energy transfer when the discharge impedance is equal to the driving line impedance, provided also that the pulse duration is properly matched to some characteristic acceleration time. However, the impedance implicit in the dynamical development of a gas-accelerating discharge is not adequately represented by an equivalent resistance, and this complication reflects itself into substantial distortion of the simple impedance-match criterion.

Theoretical Analysis

The dynamics of the current sheet motion can be most simply described by a "snowplow" relation which expresses a balance between the $\vec{j} \times \vec{E}$ body force and the time rate of change of momentum associated with the accumulation and acceleration of mass on the current sheet. For example, the equation in linear pinch geometry takes the form

$$r \frac{d}{dt} \left[\left(r_1^2 - r^2 \right) \frac{dr}{dt} \right] = - \frac{\mu_0 I^2}{4\pi^2 \rho} \quad (4-1)$$

where μ_0 is the permeability of free space, I is the total current flowing through the discharge chamber, and ρ is the ambient gas density in the discharge chamber of radius r_1 . The radius of the cylindrical current sheet, r , through which I is assumed to flow, also defines an inductance of the discharge through the relation

$$L_D = \frac{\mu_0 h}{2\pi} \ln \left(\frac{r_0}{r} \right) \quad (4-2)$$

The voltage drop across the discharge is given by:

$$V_{CH} = I R_D + \frac{d\phi}{dt} = I R_D + \frac{d}{dt} (I L_D) \quad (4-3)$$

where R_D is the resistance of the discharge, ϕ is the magnetic flux linked by the discharge, and L_D is the inductance defined by Eq. (4-2).

In these experiments the circuit also contains a switch, which to a good approximation may be represented as a fixed resistance and inductance, R_s and L_s . The switch and discharge chamber comprise the total load driven by the pulse line, and the voltage across this load may therefore be written:

$$V_T = (R_D + R_s) I + L_s \frac{dI}{dt} + \frac{d}{dt} (L_D I) \quad (4-4)$$

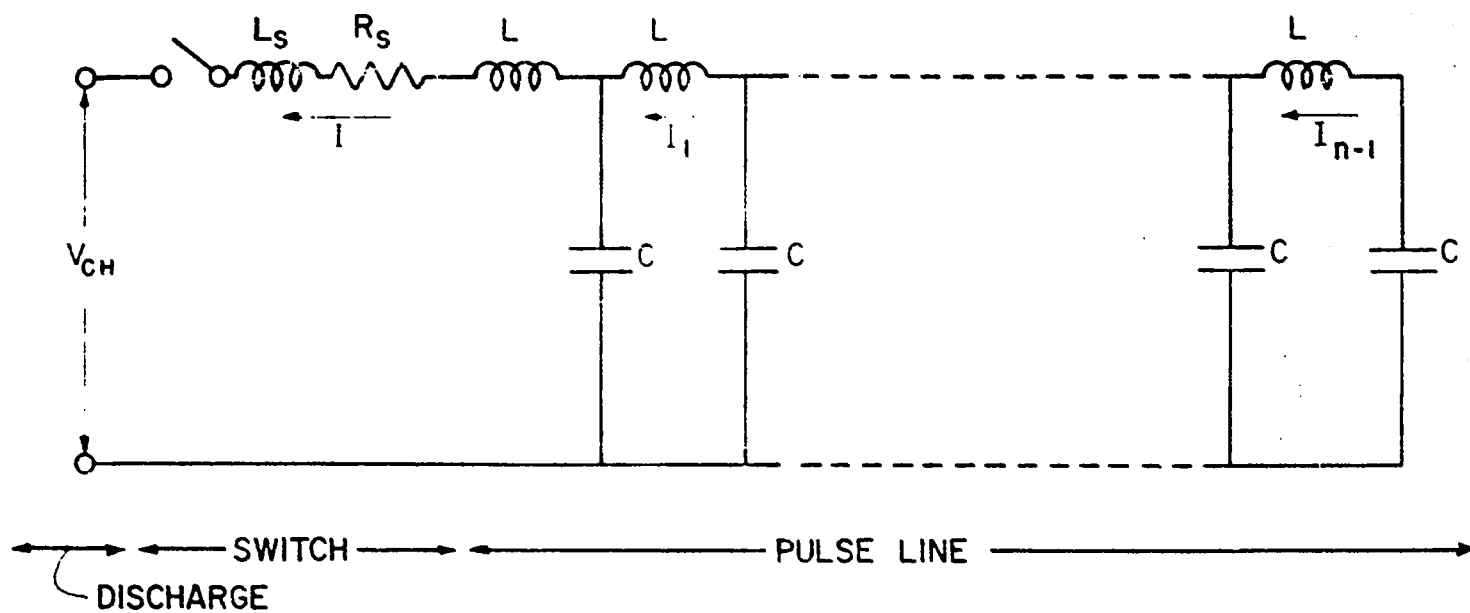
The pulse line power source may be described by Kirchhoff's equations applied to each loop and node in the pulse network (Fig. 26).

$$\left. \begin{aligned} \frac{dQ_1}{dt} &= I_1 - I \\ &\vdots \\ \frac{dQ_i}{dt} &= I_i - I_{i-1} \\ &\vdots \\ \frac{dQ_n}{dt} &= -I_{n-1} \end{aligned} \right\} \begin{array}{l} (n \text{ equations}) \\ (4-5) \end{array}$$

and

$$\left. \begin{aligned} \frac{dI}{dt} &= \frac{V_T - Q_1/C}{L} \\ &\vdots \\ \frac{dI_i}{dt} &= \frac{Q_{i+1} - Q_i}{LC} \\ &\vdots \\ \frac{dI_{n-1}}{dt} &= \frac{Q_n - Q_{n-1}}{LC} \end{aligned} \right\} \begin{array}{l} (n \text{ equations}) \\ (4-6) \end{array}$$

where Q_i represents the electrical charge on the i^{th} capacitor.

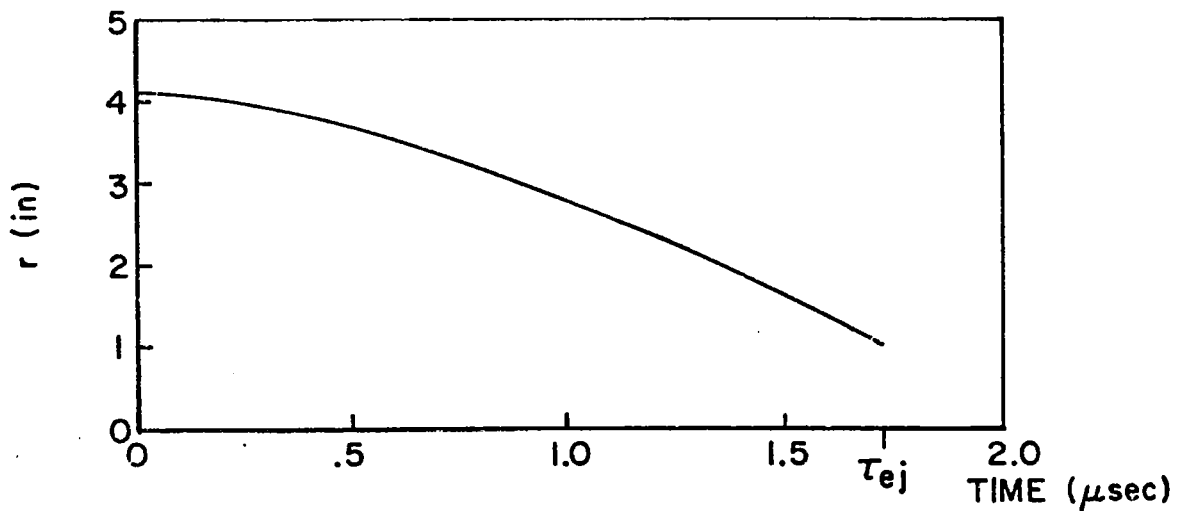
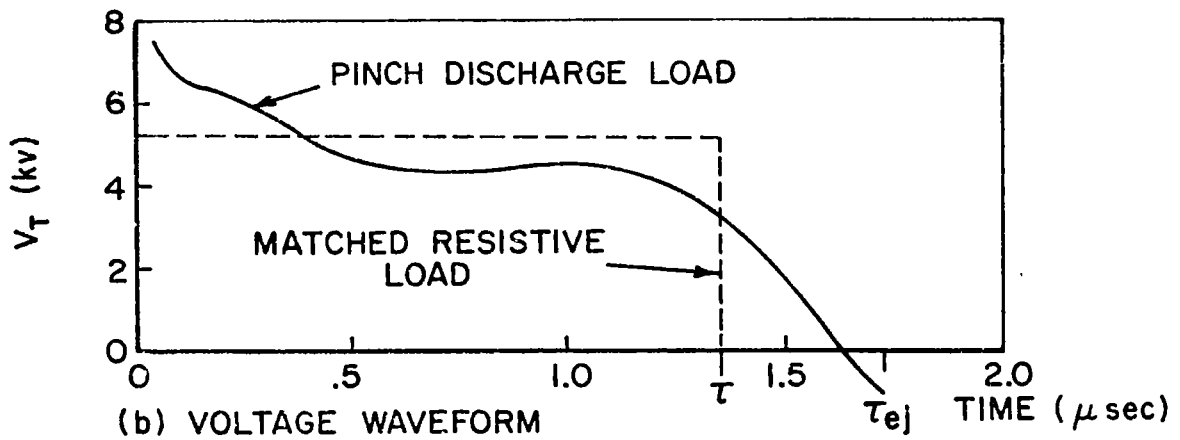
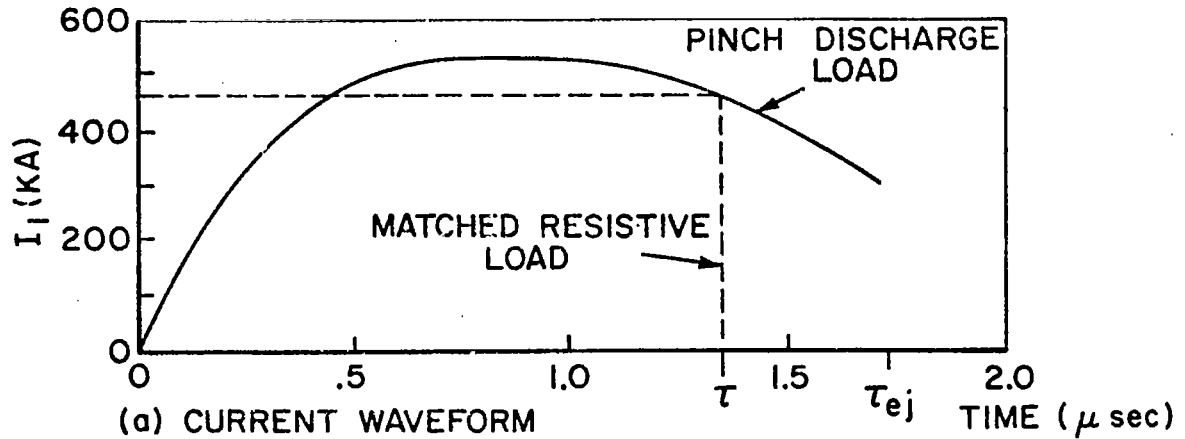


SCHEMATIC OF PULSE LINE ACCELERATOR SYSTEM

This n station LC ladder network may also be described by a nominal line impedance and a pulse duration corresponding to those given for the ideal transmission line, i.e., $Z_L = \sqrt{L/C}$ and $t = 2n \sqrt{LC}$.

Equations (4-1), (4-2), (4-4), (4-5) and (4-6) are $2n + 3$ equations in $2n + 3$ dependent variables (n pulse line currents, n pulse line capacitor charges, V_T , r , and L_D) and the independent variable time which describe the behavior of the pinch discharge-pulse line system. They have been solved here on the digital computer using a Runge-Kutta technique. Figure 27 shows current and voltage waveforms and the current sheet trajectory computed for a set of input parameters typical of those prevailing in the experiments. Figure 27a shows the total current flowing through the switch and pinch chamber as a function of time, compared with that for an ideal pulse line discharged through a matched resistance. The time τ_{ej} shown on all of the ordinates of Fig. 27 is the characteristic time over which the acceleration of the current sheet occurs. In an actual thruster τ_{ej} would be the time of ejection of the plasma, determined by the length of the thruster, but for the closed chamber geometry considered here the plasma is considered "ejected" when the sheet reaches a 1-in. radius. One inch was selected because accurate experimental investigation is difficult at lesser radii and yet the acceleration process should be allowed to occur over as large a distance as possible in order to prevent the initiation effects from dominating the behavior of the system. Figure 27b shows the voltage across the end of the pulse line (i.e., across the switch and discharge chamber) as a function of time compared with the corresponding matched impedance voltage waveform for a purely resistive load.

The evident distortions of the current and voltage waveforms from the idealized case can be assigned to the



COMPUTED CURRENT, VOLTAGE WAVE FORMS
AND SHEET TRAJECTORY

FIGURE 27

following causes:

1. The initial inductance associated with the switch and discharge configuration constrains the current to a finite rise time.

2. Unlike the constant resistive load, the impedance of the discharge varies with time. An expression for this discharge impedance can be obtained by dividing the voltage developed across the discharge chamber [Eq. (4-3)] by the total current flowing through the discharge.

$$Z_D = \frac{V_{CH}}{I} = R_D + \frac{dL_D}{dt} + \frac{L_D}{I} \frac{dI}{dt} \quad (4-7)$$

Since the plasma resistance is small and the current pulses are nearly flattopped, the second term dominates this expression, yielding, from Eq. (4-2),

$$Z_D \approx \frac{dL_D}{dt} = \frac{\mu_0 h}{2\pi r} \frac{dr}{dt} \quad (4-8)$$

The current sheet trajectory of Fig. 27c shows an increasing velocity with decreasing radius, both of which contribute to an impedance that increases with time. This effect causes the voltage to rise and current to drop once the initial rise time has elapsed.

3. Since the inductance of the discharge, which is small initially, increases to a relatively large value as the discharge proceeds, a considerable amount of energy is stored in the magnetic field of the discharge at the time the pulse begins to decay. This causes the current to continue to flow after the voltage across the discharge chamber reverses. If the characteristic ejection time, τ_{ej} , is long compared to the pulse length, τ , the energy stored in this field will be transferred, in part at least, back into the pulse network and will later produce a negative current through the discharge chamber. Even under conditions where the average

impedance of the discharge is much greater than that of the line, the negative current is observed. In such cases the current pulse is protracted far beyond the pulse duration time, t somewhat reminiscent of the stepwise decay of the overdamped resistive load (Fig. 25b), but the large inductive effects eventually force sufficient negative voltage onto the pulse line to cause the current reversal.

The analysis used to obtain the current and voltage also yields the distribution of energy in the pulse network, switch, and discharge chamber. This energy may appear in the following forms:

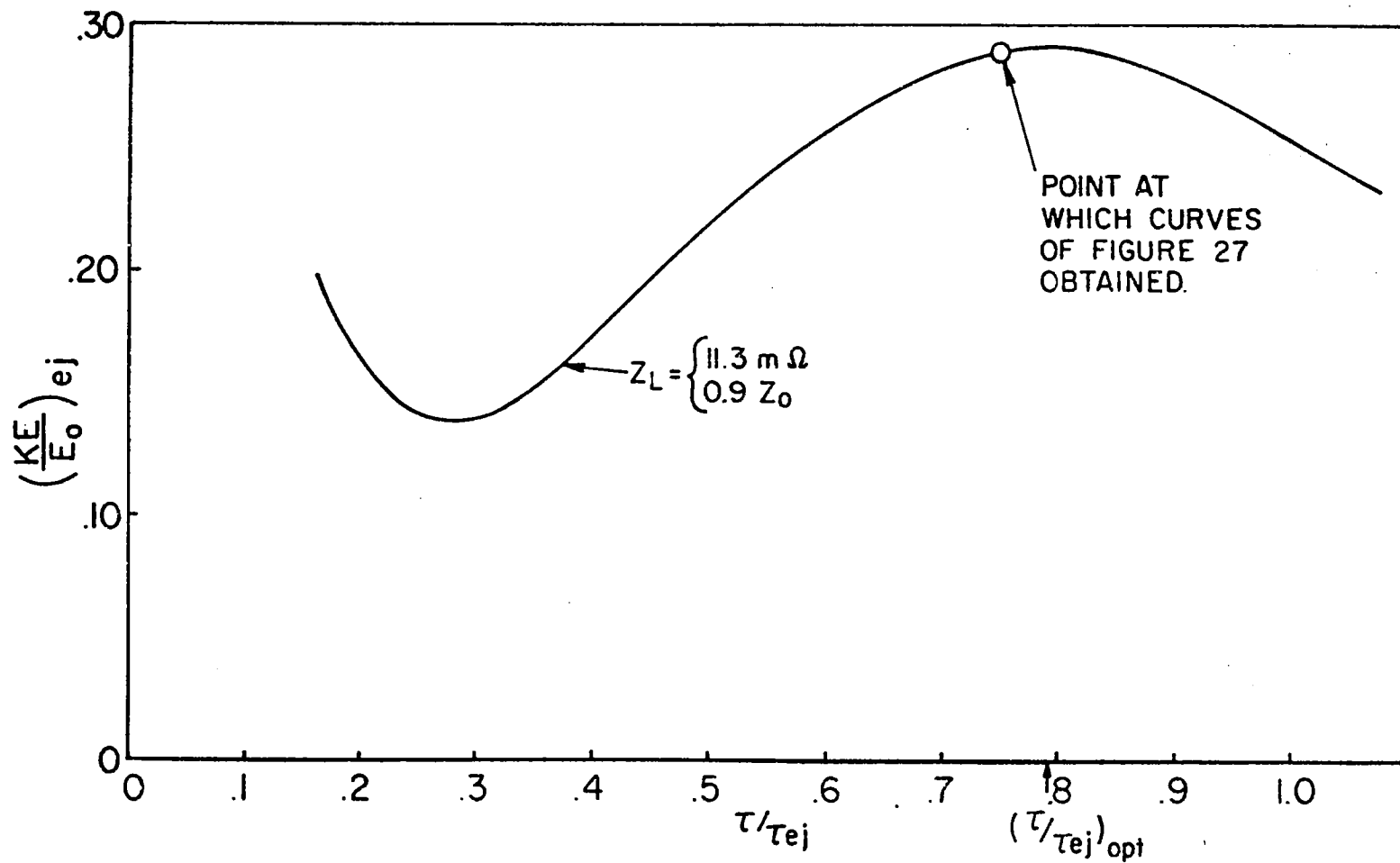
1. Energy stored capacitively in the electric fields and inductively in the magnetic fields of the pulse network.
2. Energy stored inductively in the magnetic field associated with the switch discharge.
3. Energy stored inductively in the magnetic field of the main discharge.
4. Kinetic energy of the mass accumulated on the propagating current sheet. In the spirit of this study, it is this organized streaming motion of the propellant mass which represents the thrust energy of the accelerator, and is the component to be optimized.
5. Energy invested in ionization, dissociation, excitation, and random thermal modes of the plasma. Energy input of this category can enter the theoretical model via the following two mechanisms: (a) the resistive heating input due to the plasma resistance R_p , and (b) the gasdynamic loss associated with acceleration of particles initially at rest to the current sheet velocity as a result of collisions with particles already collected. This loss, which is required to satisfy energy conservation under the constraint of momentum

conservation as expressed by the snowplow equation, is discussed in Ref. 22.

6. Thermal energy deposition in the switch plasma.

Although it is quite possible that thermal energy in an accelerated plasma may be converted into thrust energy by a suitable exhaust configuration, the efficiency of the pulsed plasma accelerator is defined conservatively here as the ratio of the organized kinetic energy measured at the characteristic time, KE_{ej} , to the initial energy stored in the pulse line, E_0 . The efficiency so defined is found to be a function of both the relative impedance match between the line and the load, and of the relative magnitudes of the pulse duration τ and the ejection time τ_{ej} . For example, variation of the pulse duration by changing the number of stations in the pulse line while holding the line impedance constant ($Z_L = 11.3 \text{ m}\Omega$) results in the efficiency curve shown in Fig. 28. The quantity Z_0 shown as a parameter is an average discharge impedance calculated using Eq. (4-8) and the sheet velocity at midradius. The time average of the impedance is approximately equal to the impedance at this radius, except for very short pulse durations, $\tau/\tau_{ej} < 0.5$, which are outside the range of primary interest.

For current pulse lengths substantially less than the optimum value of Fig. 23 the magnitude of the current is less than the maximum value over a large fraction of the acceleration time and hence the current sheet accelerates less vigorously and a proportionately smaller fraction of the initial line energy is transferred into kinetic energy of the sheet. As the pulse length is increased the current remains high for a larger fraction of the acceleration time and the current sheet acquires a larger fraction of the initial energy. Increases in pulse length beyond the optimum value result in a decrease in efficiency because a considerable fraction of the



EFFECT OF CURRENT PULSE LENGTH ON EFFICIENCY

initial line energy remains in the pulse line and in magnetic fields associated with the switch and the discharge at τ_{ej} .

For very short pulse lengths, the current waveform may go through two or more half cycles before τ_{ej} , and the efficiency will go through corresponding local maxima and minima. This analysis is not extended to the very short pulses producing these subsequent maxima because the theoretical model used here is known to break down when current reversal occurs because of the generation of secondary current sheets.

If one allows both the pulse length and the characteristic impedance of the pulse line to vary, a series of curves similar to Fig. 28 is obtained. A typical set of such curves is shown in Fig. 29 from which the optimum pulse length is seen to decrease as the characteristic impedance does. Of primary interest, however, is the locus of the maxima of the set of curves, shown in Fig. 30 as a function of the driving line impedance. Also plotted for comparison is the efficiency of energy transfer from a transmission line to a pure resistance within a time equal to the pulse duration of the line.

Note that while the maximum efficiency for the resistive load is achieved when the impedance of the line is equal to the resistance of the load, the efficiency of transfer to the pinch discharge load shows no such maximum as a function of driving line impedance. Rather there is a monotonic increase of efficiency with reduction of Z_L . This effect is attributable to the more vigorously accelerating current sheets produced by the lower impedance, higher current sources. Rapidly accelerating sheets are known to sustain less energy loss to thermal modes as a result of gasdynamic effects [22] and this gain more than balances the electrical inefficiency associated with the increasing impedance mismatch. The large

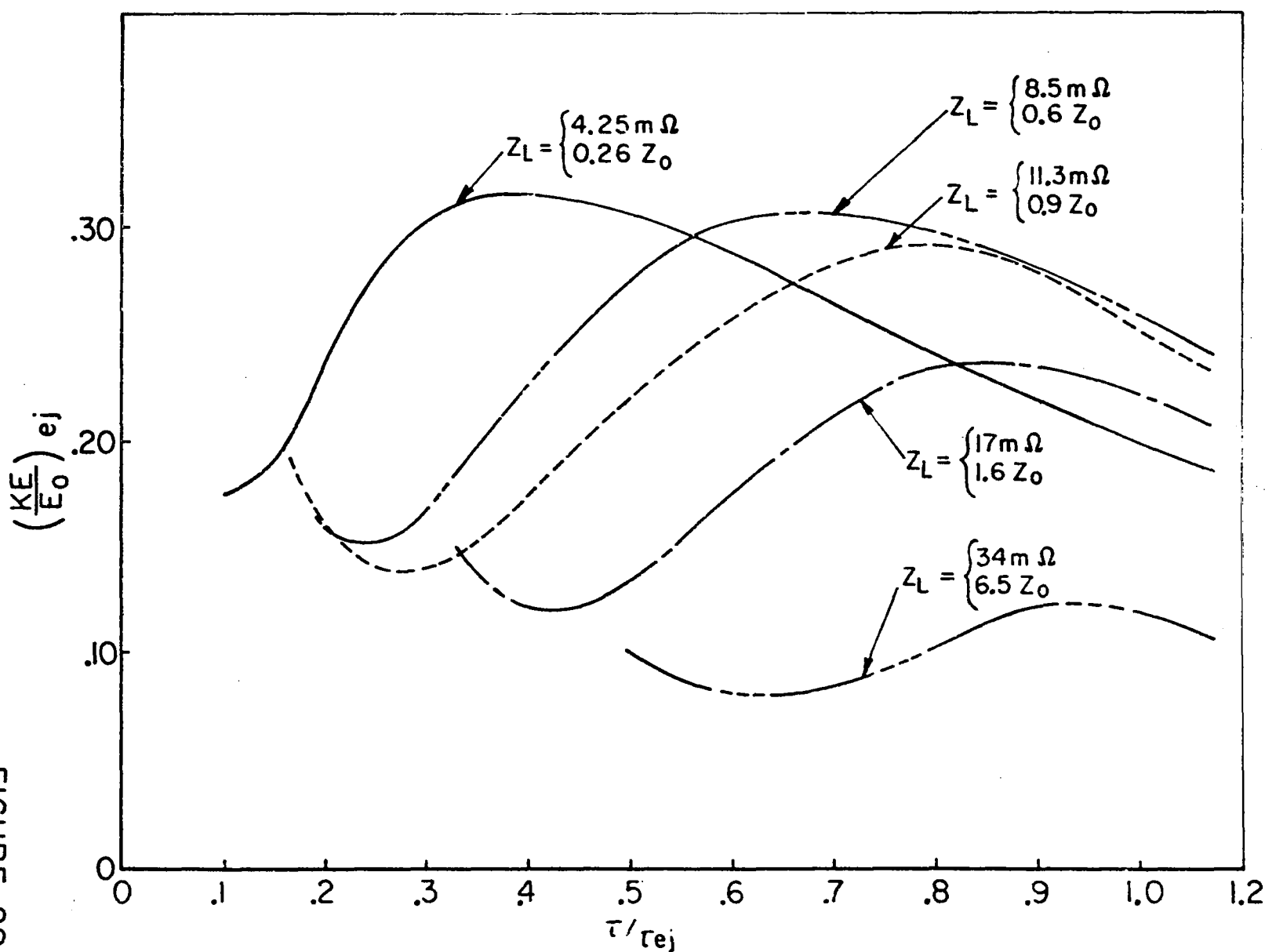
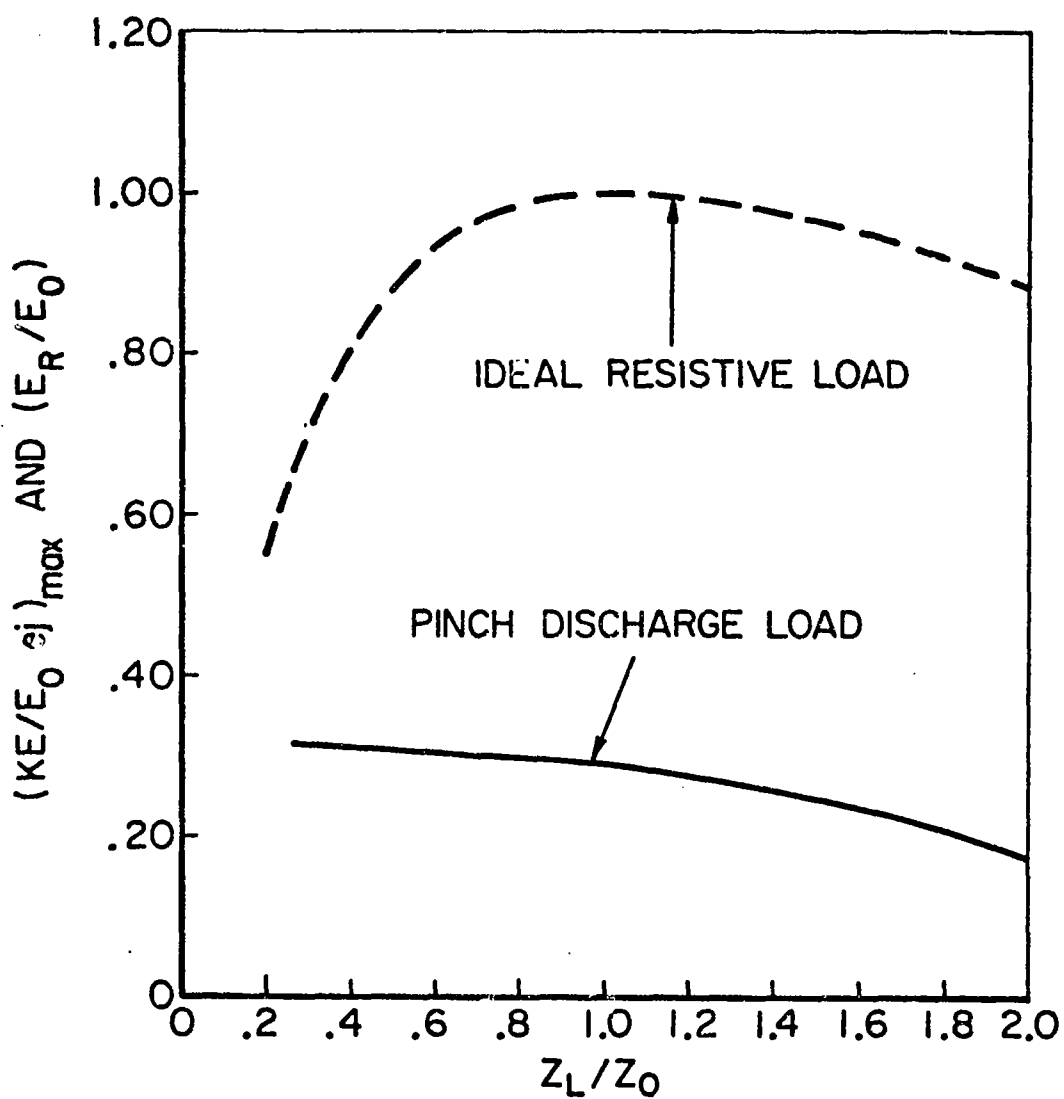


FIGURE 29

THE EFFECT OF PULSE LENGTH AND IMPEDANCE ON EFFICIENCY



EFFICIENCY VS PULSE LINE IMPEDANCE

AT 25 R 4474 C8

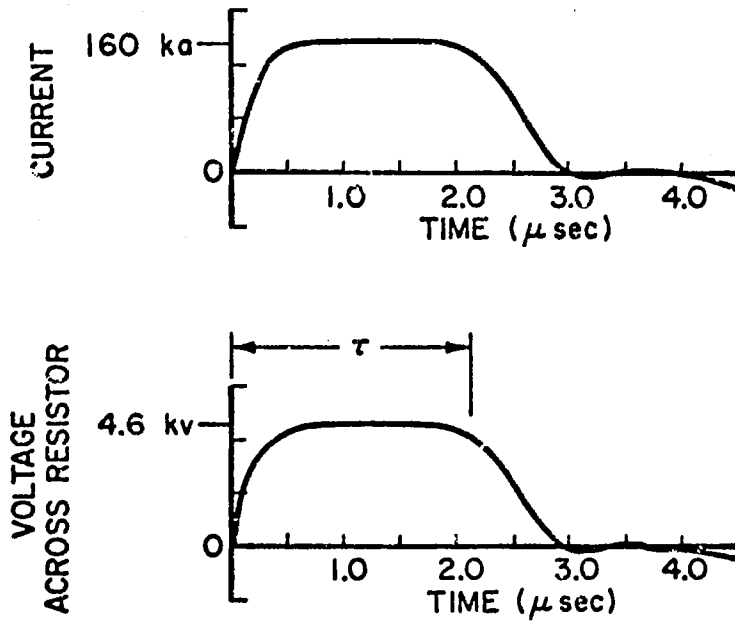
FIGURE 30

difference in magnitude of the two curves of Fig. 30 is due primarily to the method of defining efficiency for the accelerator, and maybe somewhat misleading. Much of the energy not transferred to directed kinetic motion of the plasma has been deposited in it in thermal form so that, in this sense, a major portion of the initial line energy has indeed been delivered to the "load." In addition, no effort has been made here to optimize the efficiency through selection of the discharge and switch characteristics; rather the calculations presented are those corresponding to the experimental conditions encountered in the laboratory equipment. In this equipment the losses in the switch are quite large, and they account for a significant reduction in the magnitude of the efficiency.

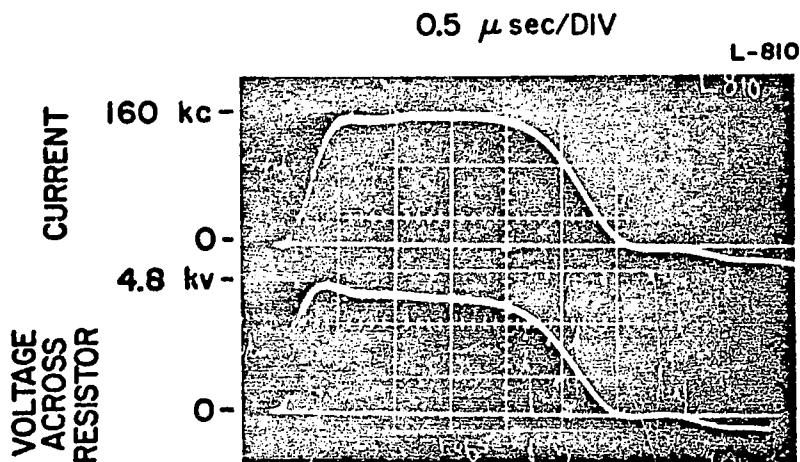
Experimental Behavior

In order to verify the mathematical description and characteristic properties of the pulse line without the complication of the pinch discharge, typical pulse line configurations were discharged through a resistor capable of withstanding the high currents and voltages produced when such a line is discharged from 10 kV. The mathematical model described in the preceding section was modified by substituting a resistance and fixed inductance for the equations describing the dynamics of the discharge. The extent of the agreement between the mathematical model and the actual pulse line is shown in Fig. 31. The waveforms differ from those of the ideal resistor discharging a transmission line (Fig. 25c) first because this line has lumped elements, rather than distributed parameters, and second because the included inductance associated with the resistor and switch restrain the rate of rise and decay of the current at the beginning and end of the pulse.

The measured capacitance and inductance of the average



(a) THEORETICAL RESULTS



(b) EXPERIMENTAL RESULTS

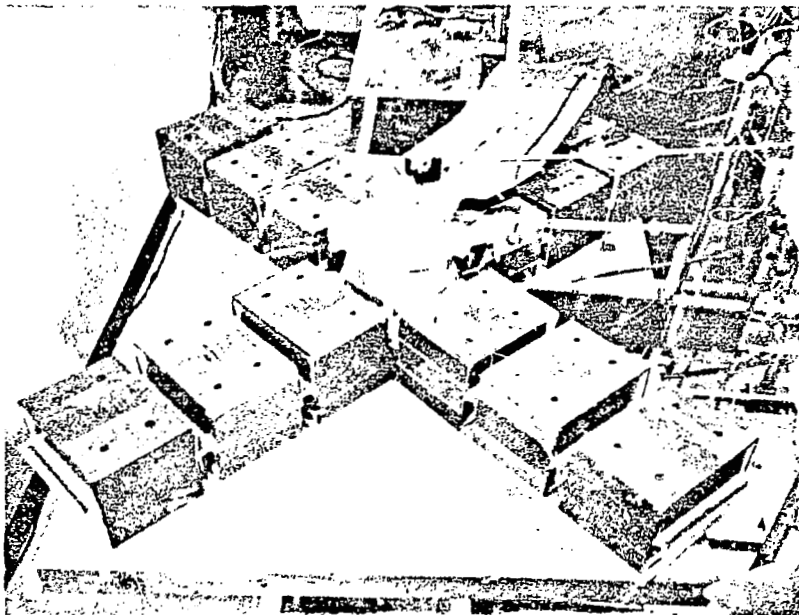
THEORETICAL AND EXPERIMENTAL WAVEFORMS
FROM MATCHED CAPACITOR LINE

FIGURE 31

unit used in these experiments are 6.35 ± 0.05 microfarads and 7.5 ± 0.4 nanohenries.⁺ They are designed to permit low inductance connection of adjacent units thereby facilitating variation of the pulse duration and the characteristic line impedance. Pulse duration is varied by changing the number of stations in a line of capacitors (i.e., the number of units connected in tandem). Line impedance is varied by changing the number of these lines connected in parallel across the discharge chamber. Figure 32 shows a typical configuration with 12 of the units arranged around the discharge chamber to produce a pulse three times the length (three units in tandem) and one-fourth the impedance (four lines of units in parallel) of the single unit pulse.

Experimental evaluation of the efficiency (KE_{ej}/E_o) requires the determination of organized kinetic motion of the current sheet mass, in ratio to the initial line energy, which is simply the product of charging voltage and total capacitance. Since direct measurement of the energy in organized kinetic motion of the current sheet is not feasible in a closed discharge chamber, this determination is based on the assumption that all of the mass the current sheet encounters is collected and accelerated, i.e., that the snowplow model is a valid representation of the physical process. This reduces the problem to measurement of the velocity of the mass associated with the current sheet as discussed in Sec. V of this report, the arrival of the current sheet as sensed by a magnetic field probe, precedes very slightly the arrival of the associated mass motion, sensed by the pressure probe, and this separation remains essentially constant over most of the trajectory. In view of this correlation, the physically smaller and simpler magnetic field probes were used to determine current sheet

⁺These prototype low inductance capacitors were developed in conjunction with the Corson Manufacturing Corp.



TYPICAL CAPACITOR ARRANGEMENT

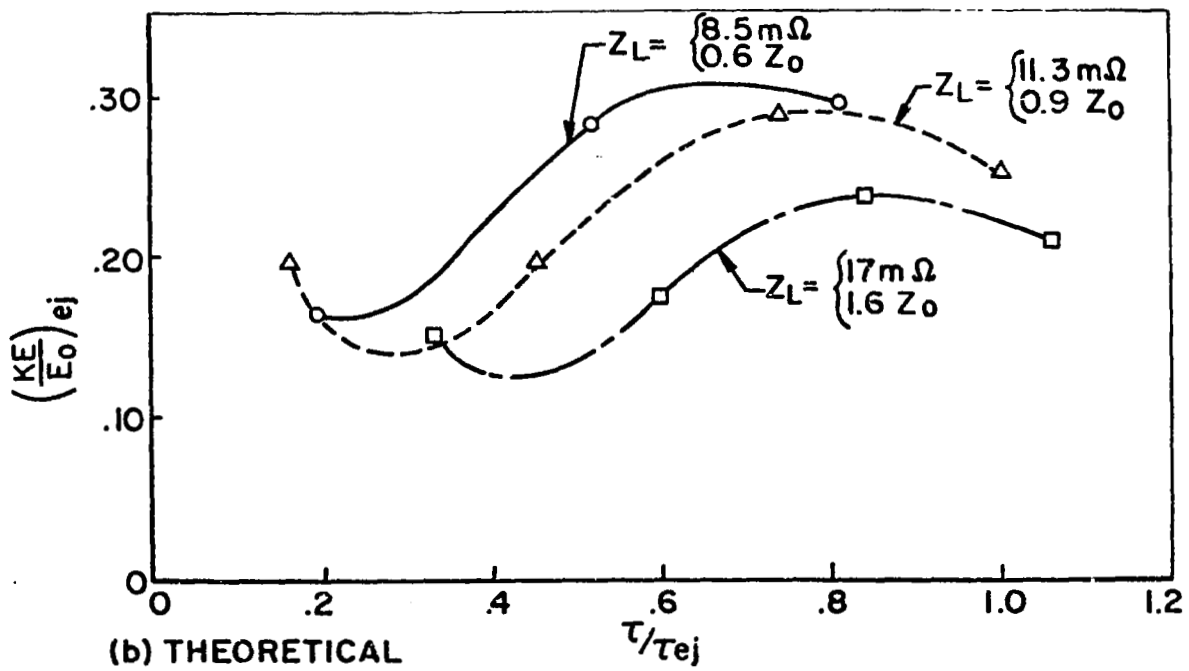
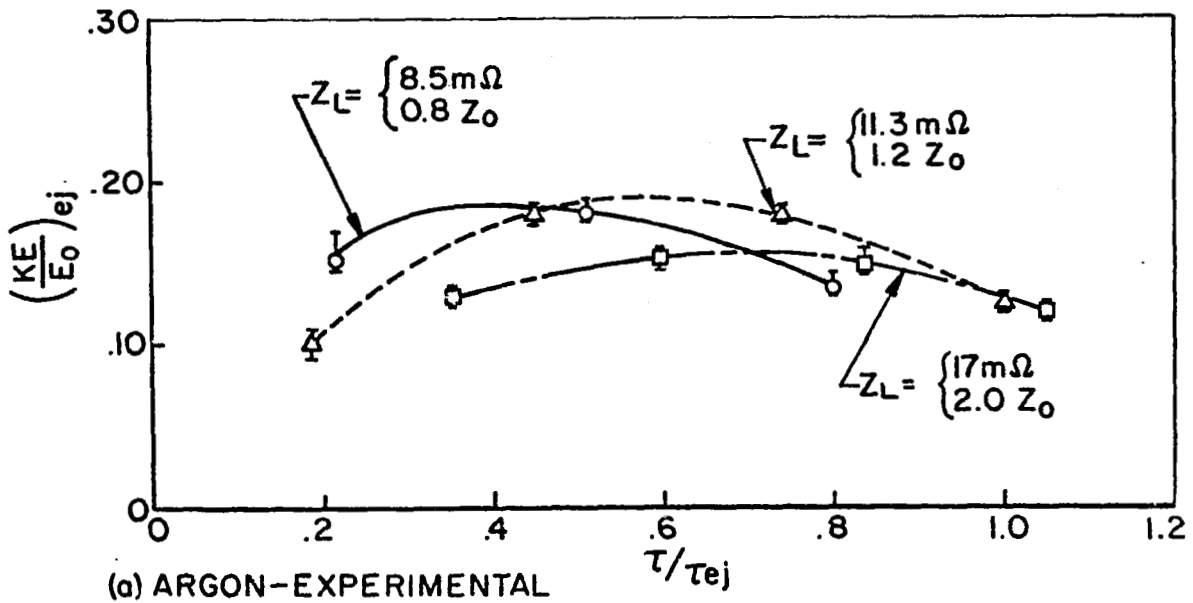
velocities and these are assumed to be the same as those of the mass trajectories. Probes were located along a common radius because errors in the measurement of current sheet velocity associated with probing in the wake of another probe were found to be far less than those due to azimuthal current sheet irregularities over sufficient angular separation to keep probes out of each other's wake.

The experimental measurements discussed above have been made in argon at an ambient density of $2.2 \times 10^{-4} \text{ kg/m}^3$ for various pulse durations and pulse line impedances, and efficiencies based on these measurements are presented in Fig. 33a. The corresponding theoretical curves are shown in Fig. 33b. The points on the theoretical curves correspond to data points similarly located on the experimental curves.

Although the snowplow model used in the theoretical calculations requires only the gas density as an input, it may be that other gas properties such as ionization potential, molecular weight, or conductivity play an important role in the acceleration process under the efficient energy transfer conditions at which these experiments were performed. In order to investigate possible effects due to gas properties, measurements were also made in nitrogen, krypton, and hydrogen. These measurements were made at the same ambient mass density as those in argon, and therefore the efficiency curves presented in Figs. 34a,b and c should also correspond to the theoretical curves of Fig. 33b.

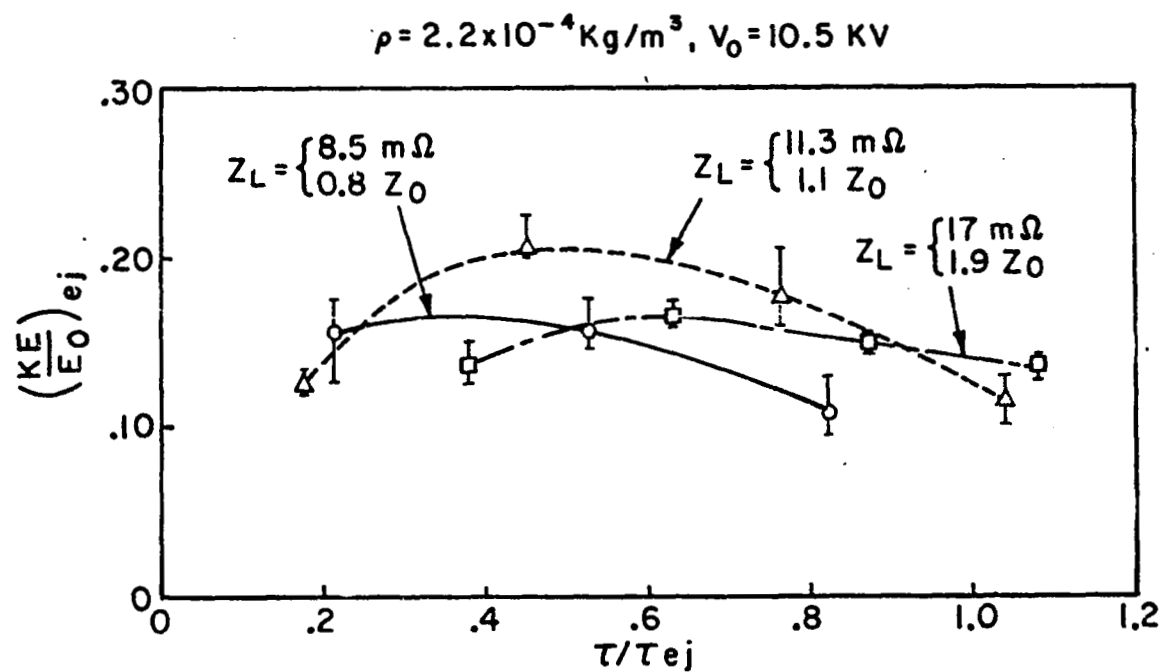
The following qualitative agreements between the experimental and theoretical results can be identified:

1. For a pulse line of a given impedance there is one length of line which gives an optimum efficiency.
2. As the impedance of the pulse line is decreased the corresponding optimum pulse length for the line also decreases.



EFFICIENCY PROFILES: $\rho = 2.2 \times 10^{-4} \text{ Kg/m}^3$, $V_0 = 10.5 \text{ KV}$

FIGURE 33

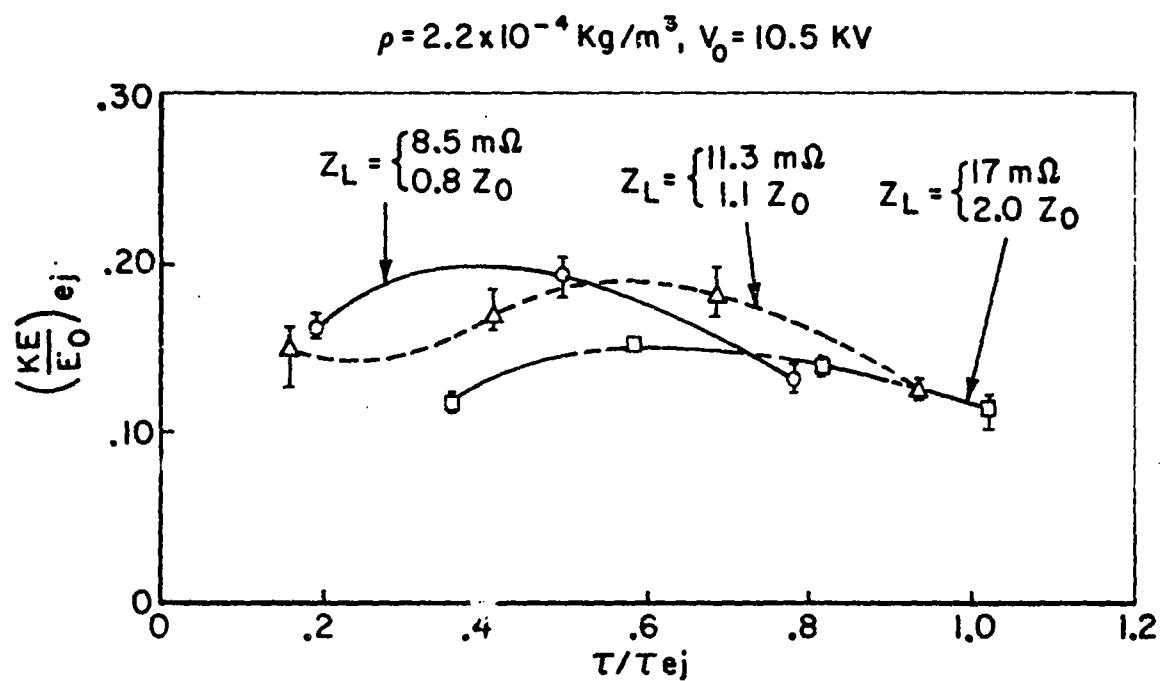


NITROGEN - EXPERIMENTAL

EFFICIENCY PROFILE

FIGURE 34 (a)

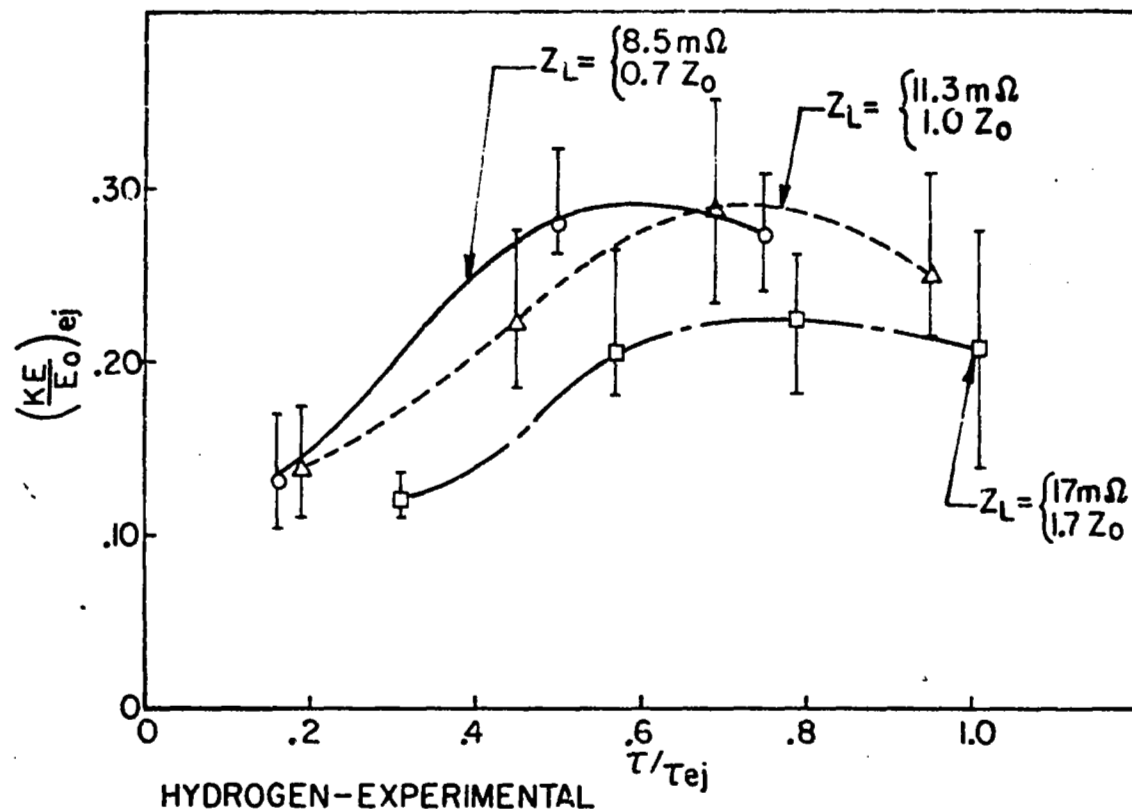
FIGURE 34 (b)



KRYPTON - EXPERIMENTAL

EFFICIENCY PROFILE

$$\rho = 2.2 \times 10^{-4} \text{ Kg/m}^3, V_0 = 10.5 \text{ KV}$$



74

FIGURE 34(c)

EFFICIENCY PROFILE

The following differences between the theoretical and experimental results obtained in argon, nitrogen, and krypton are, however, also apparent:

1. Rather than showing the theoretically predicted increasing optimum efficiency with decreasing pulse line impedance, the experimental curves show a leveling of this locus of the efficiency maxima near an impedance ratio of one.
2. The optimum pulse lengths for lines of given impedance are lower than the corresponding theoretical values.
3. Because the experimental velocities are somewhat lower than the calculated values, impedance ratios Z_L/Z_0 specified on the experimental curves are higher than those on the corresponding theoretical curves.
4. The magnitudes of the measured efficiencies are significantly less than those predicted theoretically.

The hydrogen data of Fig. 34c, unlike those of the other gases, show good agreement in both magnitude and qualitative behavior with the theoretical results. The improved correlation reflects the fact that current sheet velocities measured in hydrogen correspond much more closely to the theoretical velocities than the velocities measured in the heavier test gases. The greater experimental scatter in the hydrogen data occurs because dB/dt peaks used to determine current sheet velocities are not as reproducible or well defined in hydrogen as they are in the other test gases.

The discrepancies between theoretically predicted and measured velocities in the heavier gases which result in the lower experimental efficiencies can be assigned to a failure of all of the current flowing through the discharge chamber to concentrate in a thin sheet as the snowplow model assumes. Any current which flows in the region behind the advancing current sheet reduces the inductance [Eq. (4-2)] and the impedance [Eq. (4-8)] of the discharge, thereby predicating a lower

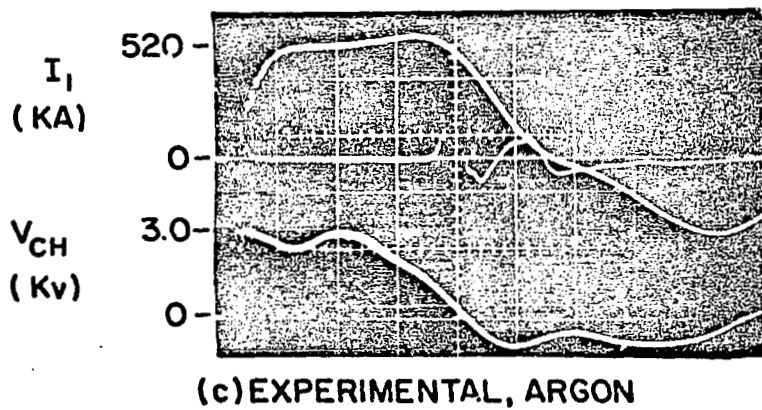
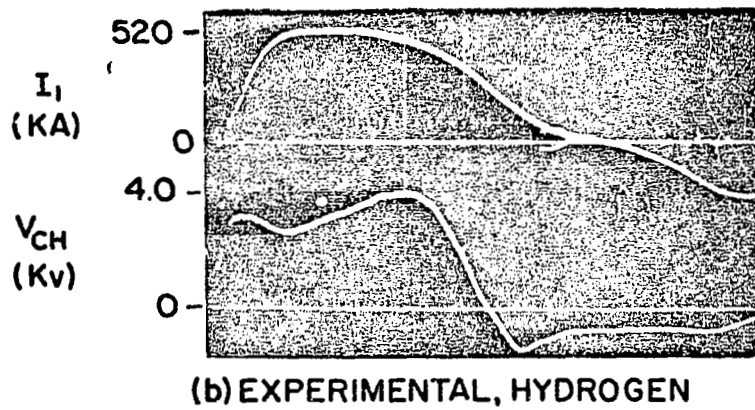
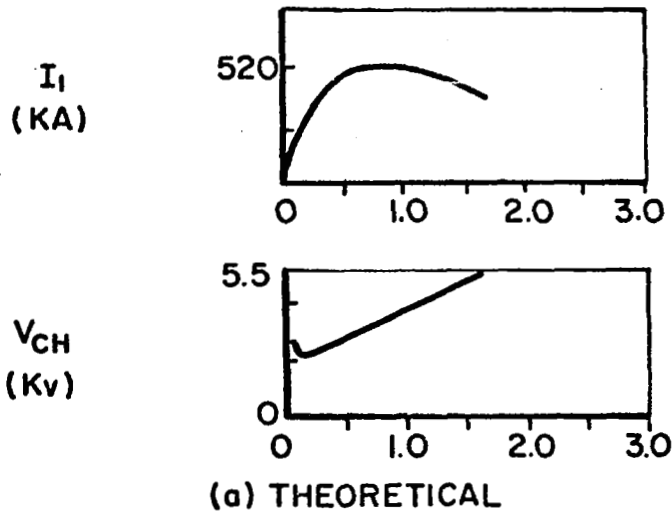
velocity sheet. Evidence that the current flowing in the discharge chamber is not confined to a thin sheet can be presented in the form of discharge chamber current and voltage oscillograms obtained in hydrogen, the corresponding theoretically predicted waveforms and the oscillograms obtained in a heavy gas (argon) shown in Fig. 35. The theoretical curves of Fig. 35a display the increase of discharge impedance with current sheet progress which forces the current magnitude to decrease and the discharge chamber voltage to rise after the initial characteristic current rise time. The experimental waveforms obtained in hydrogen (Fig. 35b) exhibit this same type of behavior, but the corresponding waveforms obtained in argon (Fig. 35c) show the discharge chamber voltage decaying and the current continuing to rise at a lesser rate, long after the characteristic rise time. Such behavior can exist only if the net load impedance is decreasing. Since measured trajectories show the current sheet is accelerating inward during this period (increasing load impedance), parallel current paths must exist which cause the decrease in net impedance observed in the argon waveforms.

This effect may be illustrated more directly by re-writing Eqs. (4-2) and (4-4) in the form

$$L_D(t) = \frac{\int_0^t (V_{CH}(\xi) - I(\xi)R_D) d\xi}{I(t)} \quad (4-9)$$

$$r(t) = r_0 \exp - \left[\frac{2\pi L_D(t)}{\mu_0 h} \right] \quad (4-10)$$

and applying them to the voltage and current data of Fig. 35 together with the measured resistance of the discharge ($R_D = 10^{-4}$ ohms), to obtain first the net inductance seen by the pulse line and then the trajectory of the mean current

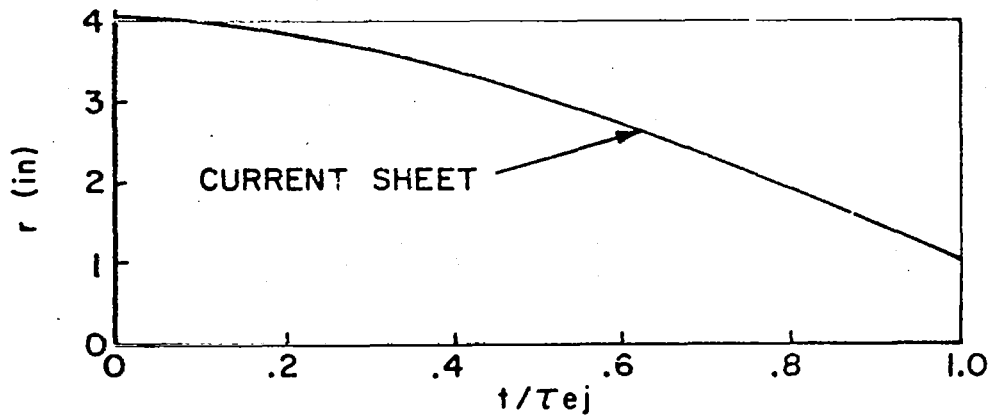


VOLTAGE AND CURRENT WAVEFORMS, $\rho = 2.2 \times 10^{-4} \text{ Kg/m}^3$,
 $V_0 = 10.5 \text{ KV}$, $\tau = 1.7 \mu\text{sec}$, $Z_L = 11.3 \text{ m}\Omega$

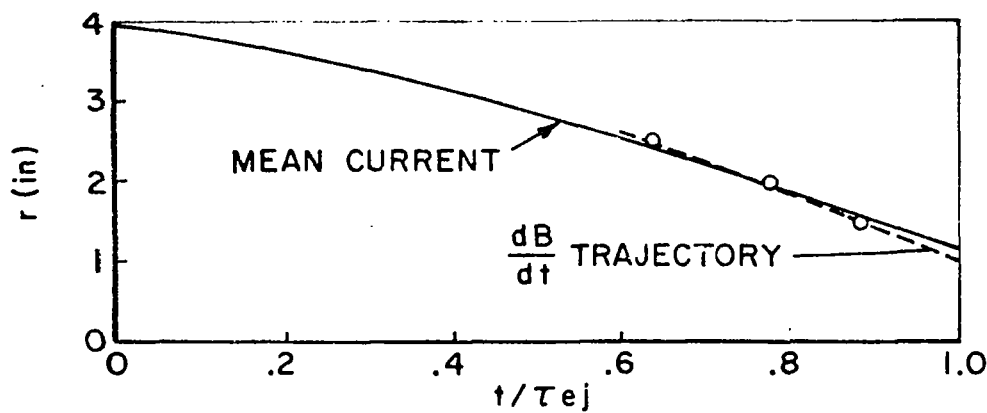
flowing in the discharge chamber which corresponds to this net inductance. These trajectories, which are shown in Figs. 36b and c for hydrogen and argon are labeled "mean current." The trajectory of the high-current density sheet, on the other hand, is determined experimentally by sensing the time of arrival of the peak of current density with a magnetic probe and is shown in Figs. 36b and c as " dB/dt trajectory." For the ideal snowplow model the mean current and peak current density trajectories are clearly identical (Fig. 36a) and for the hydrogen data they show a close correspondence, but for the typical argon discharge the mean current trajectory lags behind the trajectory of the maximum current density. This implies that the experimental inductance and time derivative of inductance are less than the ideal snowplow model predicts and thus that the discrepancy between the theoretical and experimental efficiency is due to the failure of the model to account for the diffuse current pattern set up in the discharge chamber behind the propagating high current density sheet. Additional evidence for the existence of a diffuse current pattern can be found in the magnetic probe records, but quantitative interpretation of these records is difficult because the probes produce local perturbations in the magnitude of the magnetic field under near impedance match conditions.

Summary

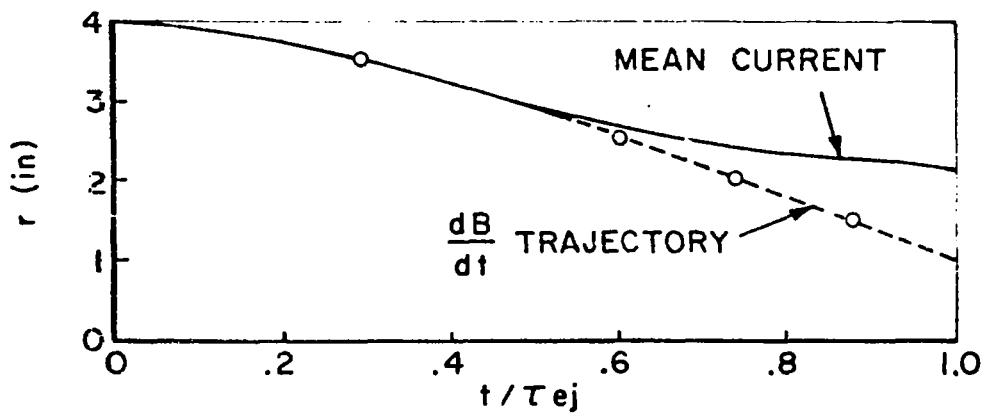
The efficiency of energy transfer from a current pulse network into organized motion of the mass associated with the propagating current sheet of a pulsed plasma accelerator has been studied theoretically and experimentally. The theory, which is based on a "snowplow" model, predicts maximum efficiency when the current sheet is driven by a pulse line that (1) has an impedance significantly below the average discharge impedance and (2) produces a pulse which exhibits cur-



(a) THEORETICAL



(b) EXPERIMENTAL - HYDROGEN



(c) EXPERIMENTAL - ARGON

CURRENT TRAJECTORIES: $\rho = 2.2 \times 10^{-4} \text{ Kg/m}^3$, $V = 10.5 \text{ KV}$

FIGURE 36

$\tau = 1.7 \mu \text{ sec}$, $Z_L = 11.3 \text{ m}\Omega$

rent reversal near the time when the mass would be expelled from the accelerator. The experimental results suggest the optimum efficiency will be realized when the line impedance is near the discharge impedance, but otherwise confirm the predicted qualitative variation of efficiency with pulse line impedance and pulse duration. The magnitudes of efficiencies in argon, krypton, and nitrogen are observed to be considerably less than the theoretical values, and these quantitative discrepancies have been related to the failure of the snowplow model to account for a fraction of the current which does not flow through the propagating high-current density sheet. Hydrogen data which correlate more closely with the theoretical results manifest a larger fraction of the current flow through the sheet.

V. PRESSURE DISTRIBUTION IN THE STRUCTURE OF A PROPAGATING CURRENT SHEET (York)

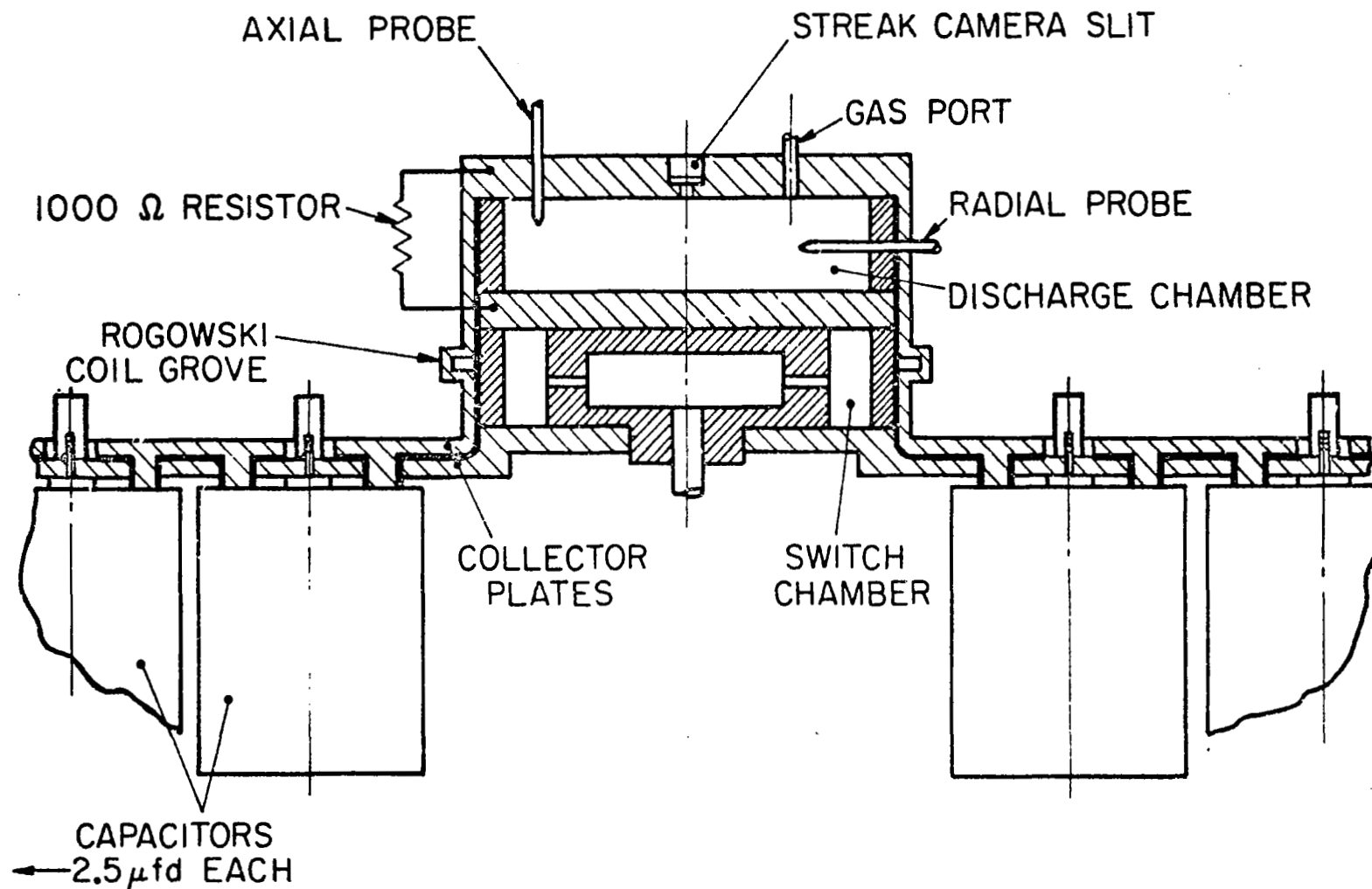
In a properly designed and operated pulsed plasma accelerator, the propagating current sheet entrains a large fraction of ambient gas, but the details of the entrainment process and the mass distribution within the sheet have so far evaded direct observation. This section describes a series of experiments to probe the interior of a current sheet in argon with a high-speed, high-resolution pressure transducer, correlated with other diagnostics, to determine the profile of gas-kinetic pressure and thereby to infer the distributions of mass density and related properties.

Apparatus and Current Sheet Observations

The propagating current sheet is generated in the closed-chamber linear pinch discharge device shown in Fig. 37 driven by a 50- μ f pulse-forming network charged to 10 kV. The discharge chamber is 8-in. in diameter, has a 2-in. electrode spacing and is initially filled with argon of a uniform pressure of 0.1 torr. The circuit current waveform, shown in Fig. 38a is tailored empirically to provide a constant velocity, constant current density sheet over its radial incursion.

Also shown in Fig. 38b,c,d is a series of radial-view Kerr-cell photographs, taken through the sidewall Pyrex insulator, via an opening in the outer return conductor. Magnetic probe records taken simultaneously with such data indicate that the visible luminous fronts correspond closely to the positions of the current sheet. Departure from the ideal cylindrical sheet configuration is evident, both as a diffusion of the structure near the anode and to a lesser extent near the cathode, and as a slight inclination of the sheet with respect to the axis. However, the current sheet in the mid-electrode region between radii of 3 in. and 1 1/2 in. is found to be

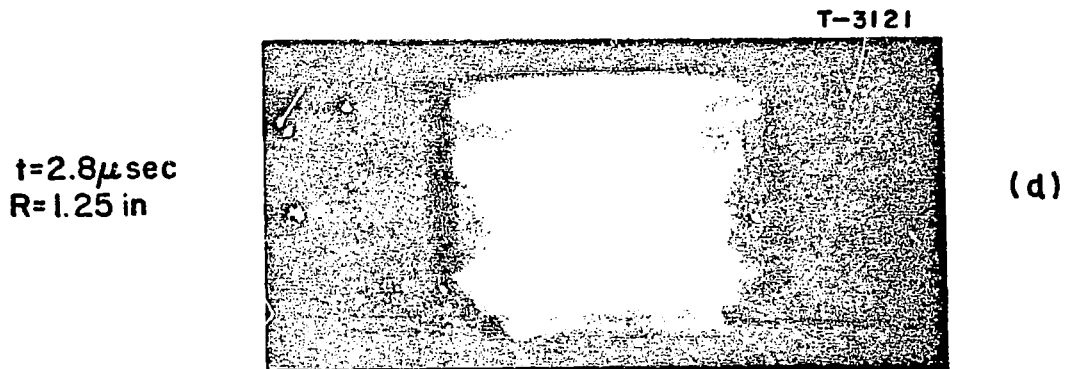
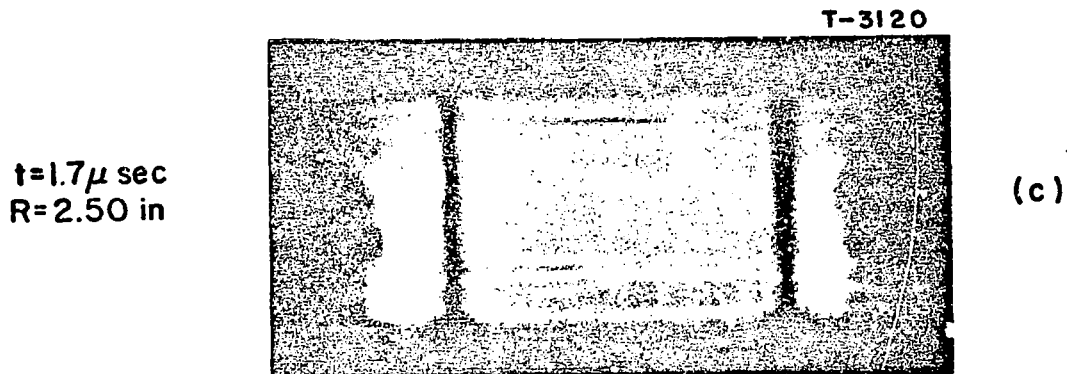
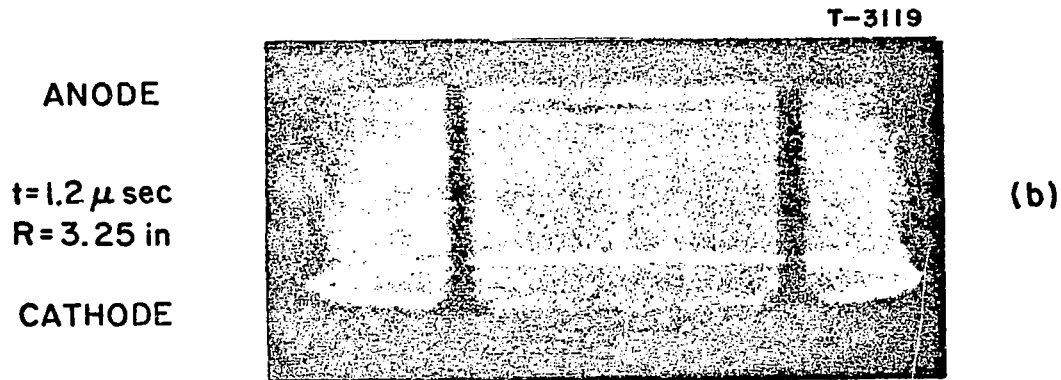
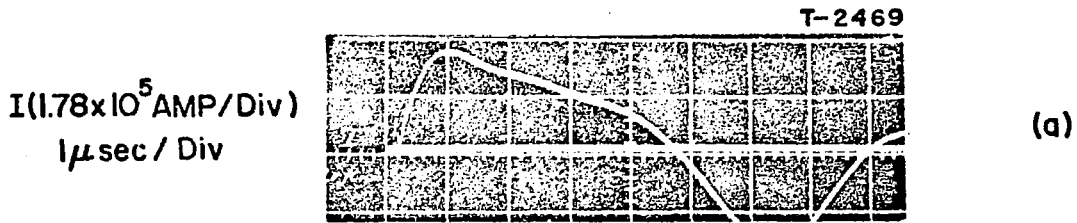
FIGURE 37



82

DISCHARGE CHAMBER ARRANGEMENT FOR PRESSURE PROBE STUDIES

AP25-4250-67



CIRCUIT CURRENT WAVEFORM AND RADIAL VIEW PHOTOGRAPHS
 OF PINCH DISCHARGE

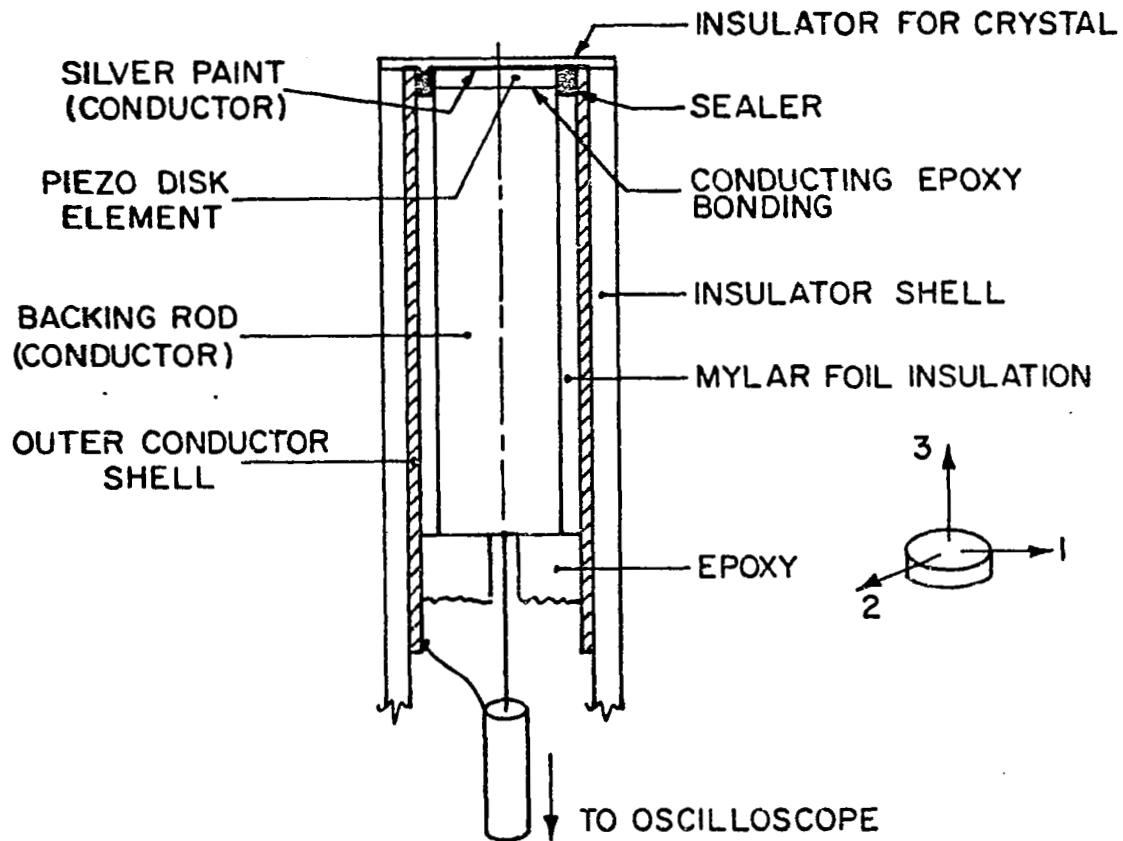
well-defined and stable, with a current density of about 10^8 amp/m², a thickness of about 1.5 cm, and a constant radial velocity of about 3×10^4 m/sec. All of the subsequent experiments are confined to this mid-electrode portion of the sheet.

Pressure Probe Development

An ideal probe for the designed measurement would faithfully respond to the profile of gas-kinetic pressure in the passing current sheet with a linear output, free of spurious signal, while negligibly disturbing the local sheet structure. For the sheet intensity, width, and velocity involved here, this translates into requirements of millimeter spatial resolution, tenth-microsecond (real-time) rise time, and a linear sensitivity of at least 0.1 mV/torr, uncompromised by the electromagnetic noise from the adjacent discharge.

The state-of-the-art performance of various existing pressure probes applicable to plasma studies, as recently surveyed by Jones and Vlases (A-3) does not meet the above requirements. Several attempts have been made to probe transient discharges of the present type with direct-contact piezoelectric devices (A-4, A-5) but these served only to define nominal time-of-arrival of relatively large pressure pulses. To follow exactly the pressure profiles on a submicrosecond time scale requires the development of a new, highly specialized probe.

Briefly, the probe concept found to be optimum for this application involves a piezoelectric ceramic separated from the plasma by a minimum of insulation, and suitably supported by a structure of backing rod, coaxial electrode connections, and an insulated housing as shown in Fig. 39. The most critical aspect of probe design affecting the linearity of its response is the proper matching of the backing rod to that of the piezoceramic. The common practice of matching the acoustic impedance,



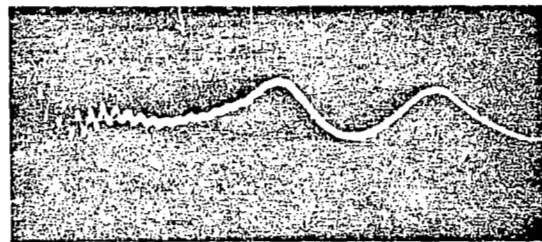
SCHEMATIC OF PIEZOELECTRIC PRESSURE TRANSDUCER

AP25 R 4933-68

FIGURE 39

$Z \equiv [E(\text{Young's modulus}) \times \rho(\text{density})]^{1/2}$, of the two elements to minimize the thickness oscillations was found to be inadequate. Specifically, using PZT 5-A ceramic elements (Clevite Corp., Cleveland, Ohio) with brass, tin, and nonpolarized PZT 5-A backing elements, the internal thickness oscillations changed little while the radial mode oscillations dominated the probe response. An analytical and experimental study of the stress conditions across the crystal-backing rod interface [61] indicated that the lateral strain, $\epsilon_R \propto \nu$ (Poisson's ratio)/ E (Young's modulus) would be critical, and that the radial wave distortion could be reduced by specifying $\epsilon_R(\text{backing rod}) \ll \epsilon_R(\text{ceramic})$, i.e., the backing rod should serve to damp the radial oscillations. Stainless steel was found to be the best common material from this standpoint.

The prototype transducers use ceramic elements 0.010-in. thick, 5/32-in. (4 mm) in diameter, encased in the insulated coaxial arrangement shown in Fig. 39. A 5/16-in. o.d. Pyrex encased unit is used for radial probing and a 1/2-in. o.d. nylon encased unit for axial probing. The electrical insulation on the crystal face consists of 1 layer of 1 mil thick Scotch #74 insulating tape covered with one thin layer of Zapon Aquanite (Glidden) lacquer. The response of this type probe to head-on reflection of a shock wave in a shock tube is presented in Fig. 40. The high-frequency oscillations are due to thickness mode stress propagation but do not inhibit evaluation of the real-pressure mean response. The onset of the more critical lower frequency radial mode oscillation is delayed until about 1.5 μsec , allowing reasonable measurements of pressure to be made within that interval. Calibration was carried out over a range of reflected shock waves in 0.5 torr to 1.0 atm argon, producing pressure differences up to 5.2 atm; over the entire range the probe response was linear with the pressure increase. To preserve the frequency response, the probing unit is coupled with a battery powered cathode follower when used within the discharge.



0.5 v/DIV

0.5 μ sec/DIV

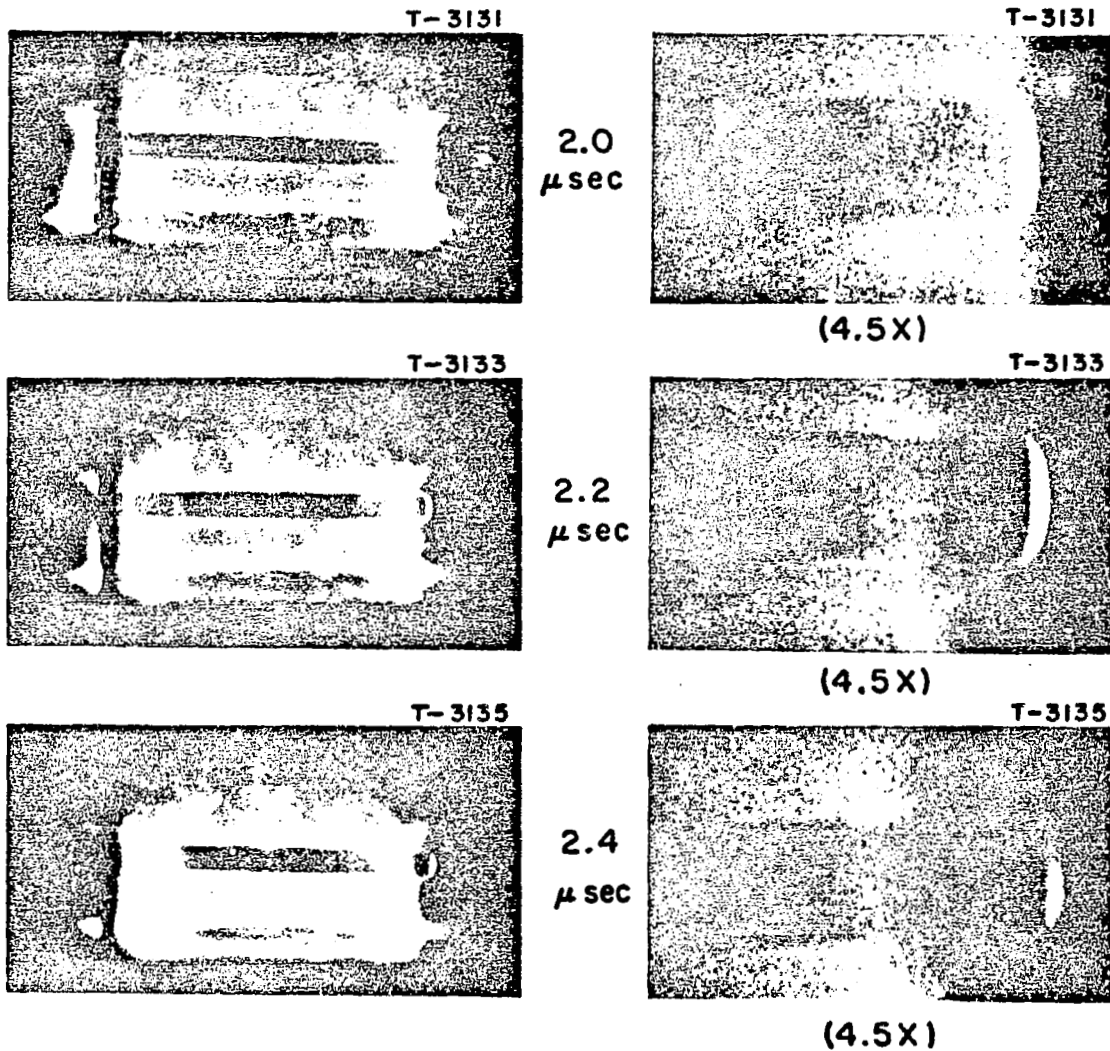
PRESSURE PROBE RESPONSE TO A
REFLECTED SHOCK IN SHOCK TUBE

FIGURE 40

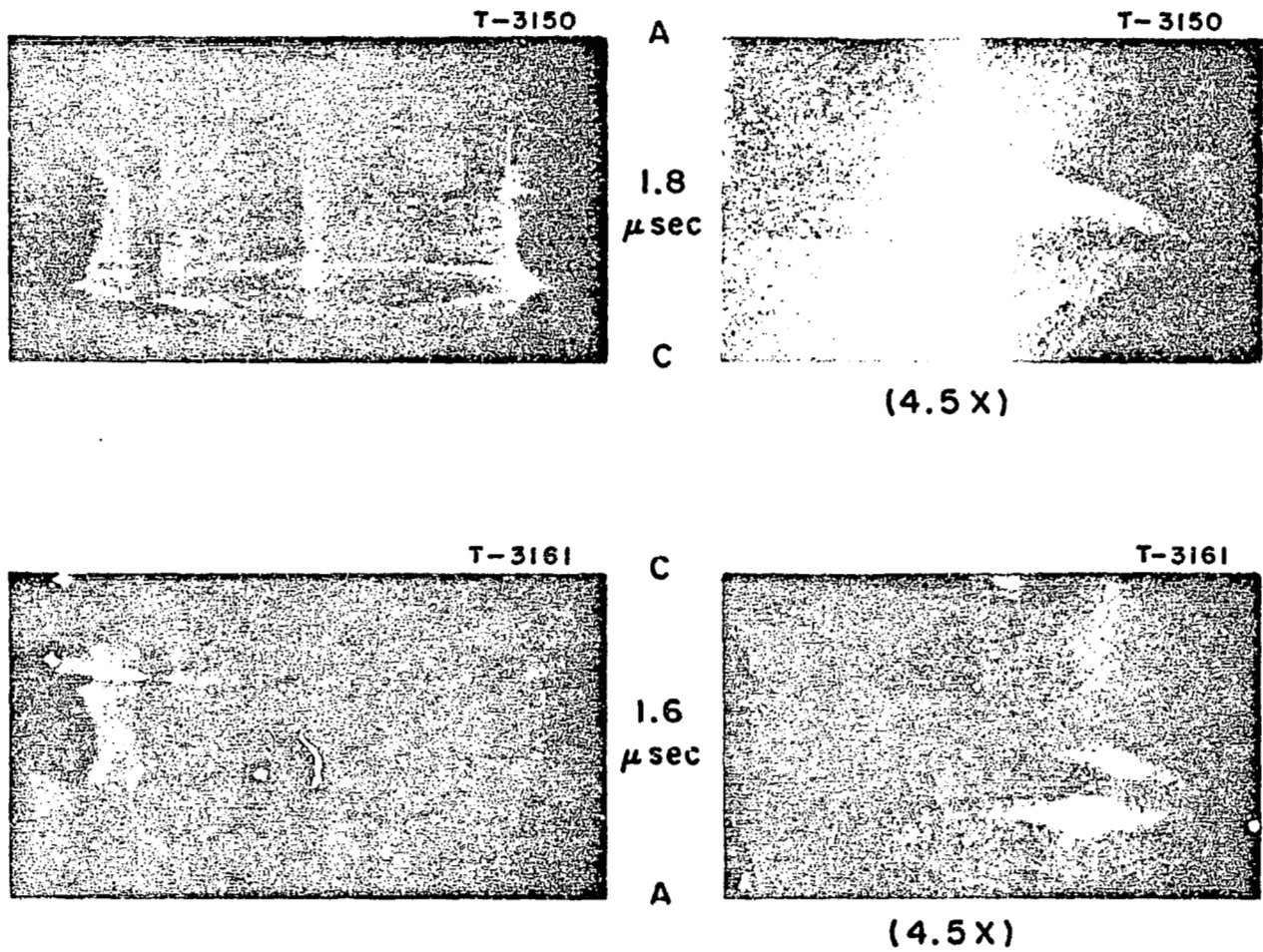
Pressure Probe - Current Sheet Interaction

To examine the current sheet away from the electrode surfaces, for the reasons discussed above, it is necessary for the body of the probe to project into the chamber. Interpretation of its response thus must be based on some understanding of the interaction of the current sheet with the probing body. Figure 41 displays Kerr-cell photographs of the luminosity patterns developed over the radial probing shape at $R = 2"$, mid-plane. After the passage of the well-defined rear surface of sheet luminosity, a form of detached "bow wave" appears shrouding the bluff probe end, perhaps indicative of a residual gas flow behind the sheet. Similar luminous waves are observed on the upstream (stagnation) side of the axial probe body. In the hope of reducing spurious diffraction signals on the sensing surface of the axial probe, it was fitted with a sharp-leading edge annular collar. Photographs of the sheet-induced flow over this configuration are shown in Fig. 42. Note that a luminous wave is still visible over the sensitive probe surface, and further, that the wave-surface angle is distinctly different for the probe mounted on the cathode than for that mounted on the anode. Such behavior suggests that flow deflection occurs at the leading edge in each case and is perhaps indicative of a flow inclination associated with the slightly tilted sheet.

A complementary factor to be considered is the effect of the probe body, and any appendages to it, on the distribution of current density within the sheet. Figure 43 shows simultaneous records of axial pressure and magnetic induction change, \dot{B}_0 , --here essentially proportional to local current density-- taken with several different probing shapes. Note that the distortion in current density profile caused by a "flow isolator" far outweighs any improvement in the pressure response, indicating that a bare probe, without isolator, is the optimum arrangement for obtaining undistorted, well-correlated measurements.

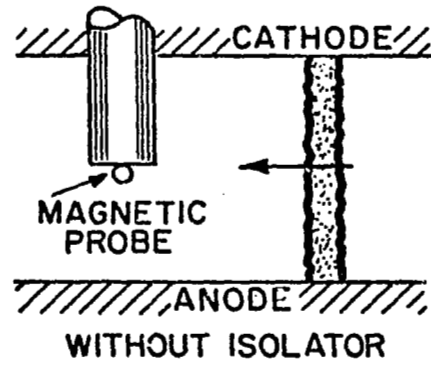
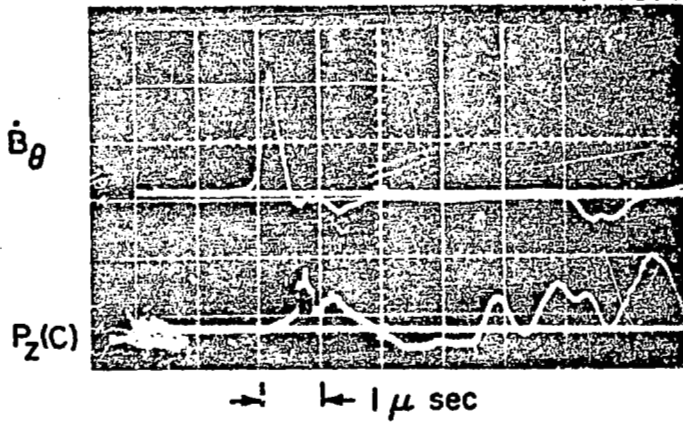


LUMINOSITY PATTERNS ABOUT RADIAL PROBE

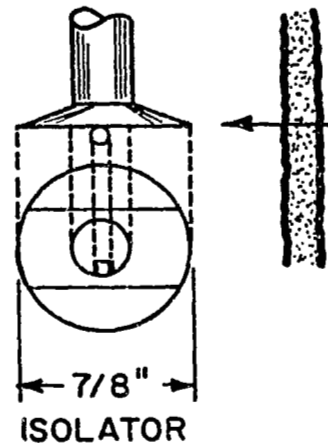
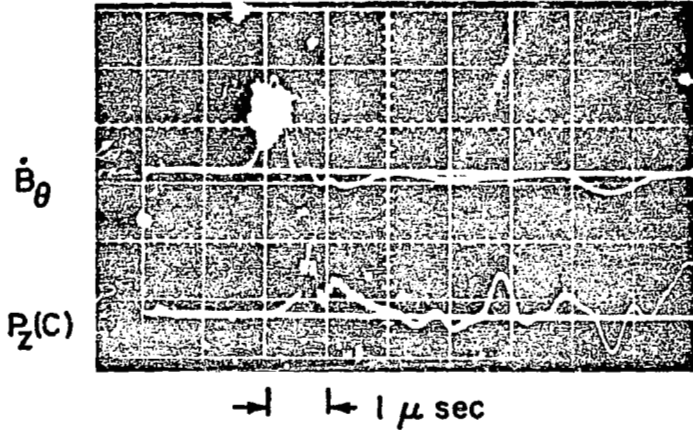


LUMINOSITY PATTERNS ABOUT AXIAL PROBE WITH
FLOW ISOLATOR

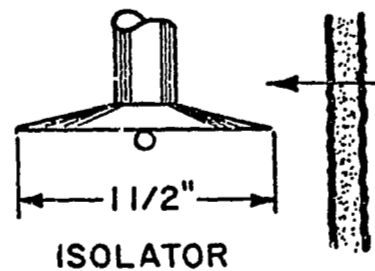
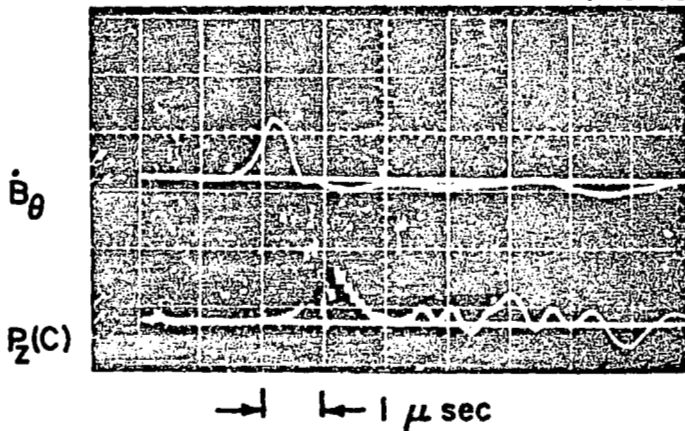
T- 3576



T- 3577



T- 3578



EFFECT OF FLOW ISOLATOR ON PROBE RESPONSE
($R = 2''$; $h = 1''$)

Experimental Determination of Current Sheet Profiles

The current sheet structure is probed with the pressure sensing instruments described above, with magnetic induction coils, and with double electric field probes. Circuit current is measured with an external Rogowski loop. The magnetic probes of Formvar-coated copper wire, 2.4 mm diameter, are mounted on the pressure probe body, directly adjacent to the pressure-sensing surface to insure exact time correlation. The electric field probes are conically shaped with a 2.5 mm diameter ring electrode separated by a 1.85 mm gap from a tip electrode of equal area. Data are recorded with the axial pressure probe mounted on the anode and on the cathode (Fig. 42). The axial and radial probes are separated by a 30° azimuthal angle to avoid mutual distortion; tests made with the probes arranged in several different relative positions confirmed that such a configuration allowed exact time correlation of the data. Three separate discharges are required to acquire complete data at any one point in the chamber; the magnetic probe measurement is repeated as a control:

Discharge 1: $P_R, E_Z, I, \dot{B}_\theta$

Discharge 2: $P_Z(C), E_R, B_\theta, \dot{B}_\theta$

Discharge 3: $P_Z(A), E_R, B_\theta, \dot{B}_\theta$

Typical results, time-correlated using the common \dot{B}_θ signal, are presented in Fig. 44.

On the basis of such data, we identify three segments of the current sheet structure:

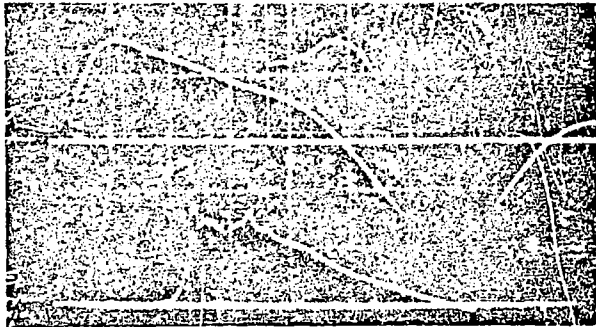
Region I, characterized by intense current conduction, isotropic pressure response of relatively small magnitude, and finite axial and radial electric fields.

Region II, characterized by relatively small current density, a strong, discontinuous radial

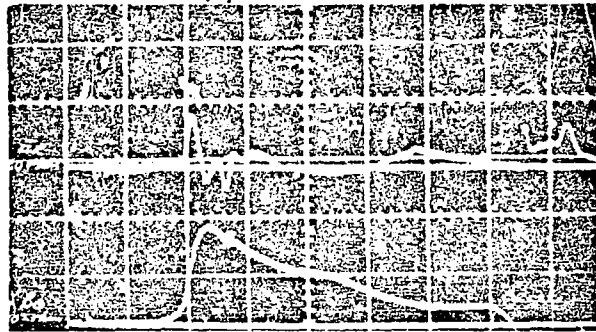
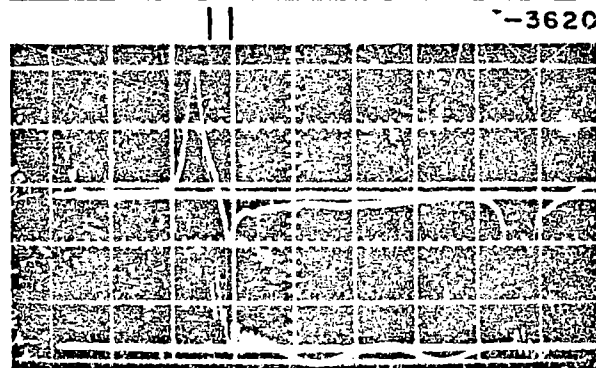
REGIONS: I II III

|| → ← 1 μ sec/DIV

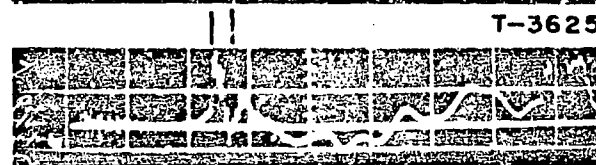
I

 E_z
(2. v/Div)

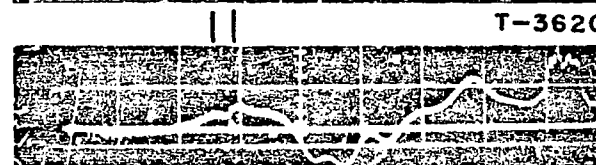
T-3625

 E_r
(2. v/Div) B_θ \dot{B}_θ P_R
(20. v/Div) $P_z(C)$
(.5 v/Div) $P_z(A)$
(.5 v/Div)

T-3620



T-3625



T-3620



T-3623

TYPICAL PROBE RESPONSES

 $R=2''$, $h=1''$

pressure response, and different magnitudes of axial pressure depending on the probe orientation.

Region III, characterized by negligible current density and radial pressure response, approximately equal axial pressures, and strong axial electric field and azimuthal magnetic fields.

Two features of this structural pattern are of particular significance: (1) there is a distinct delay ($\sim 0.2 \mu\text{sec}$) between the \dot{B}_θ peak and the sharp pressure rise, implying a corresponding spatial separation of 0.6 cm between the position of maximum current density, and the leading edge of the accumulated mass. (2) The abrupt pressure rise is quickly followed by a rapid expansion, implying that the accumulated mass is confined to a narrow layer, ~ 0.1 cm thick.

Similar data obtained at other radii between 3 in. and 1 1/2 in. indicate that all measured properties in each of the three regions remain virtually constant as the sheet implodes, with the exceptions of the radial pressure in Region II which increases with sheet progression, and the separation between \dot{B}_θ peak and pressure discontinuity, which increases.

Reduction of magnetic and electric probe records to profiles of current density and electric field proceeds in standard fashion, but extraction of gas-kinetic pressure profiles from the piezoelectric signatures involves consideration of both electrostatic sheath and gasdynamic effects [61]. Regarding the sheath effect, a momentum analysis of particles streaming between the plasma and the probe surface indicates that the pressures sensed by the piezo-element are equal to the gas-kinetic pressure in the plasma. An exact analysis of the gasdynamic interaction is not possible because of the

transient nonequilibrium nature of the event, but these effects can be estimated to establish approximate relationships. The transient character of the interaction, along with estimates of local plasma properties, indicate that effective "cold wall" conditions prevail, i.e., the characteristic time for thermal transport is of the order of that for fluid dynamic adjustments, suggesting that Newtonian analysis may be applicable. At worst such an approach should serve to correlate first-order effects. In this spirit, for example, in Region I, where $P_R \approx P_Z(C) \approx P_Z(A)$ implying negligible gasdynamic interaction, then $P_{STAT} \approx P_Z$. For Region II, where $P_R \gg P_Z(C) \gg P_Z(A)$, $P_R \approx nm_A V_s^2$ while $P_Z(C) \approx P_{STAT} + nm_A (V_s \sin \phi)^2$ when ϕ is the angle of sheet tilt and $P_Z(C)$ is corrected for the effects of zone (II) thickness relative to the element size. In Region III, $P_R > P_Z(C) \approx P_Z(A)$, and so $P_{STAT} \approx P_Z$. The sheet pressure profiles computed from these relations are presented in Fig. 45.

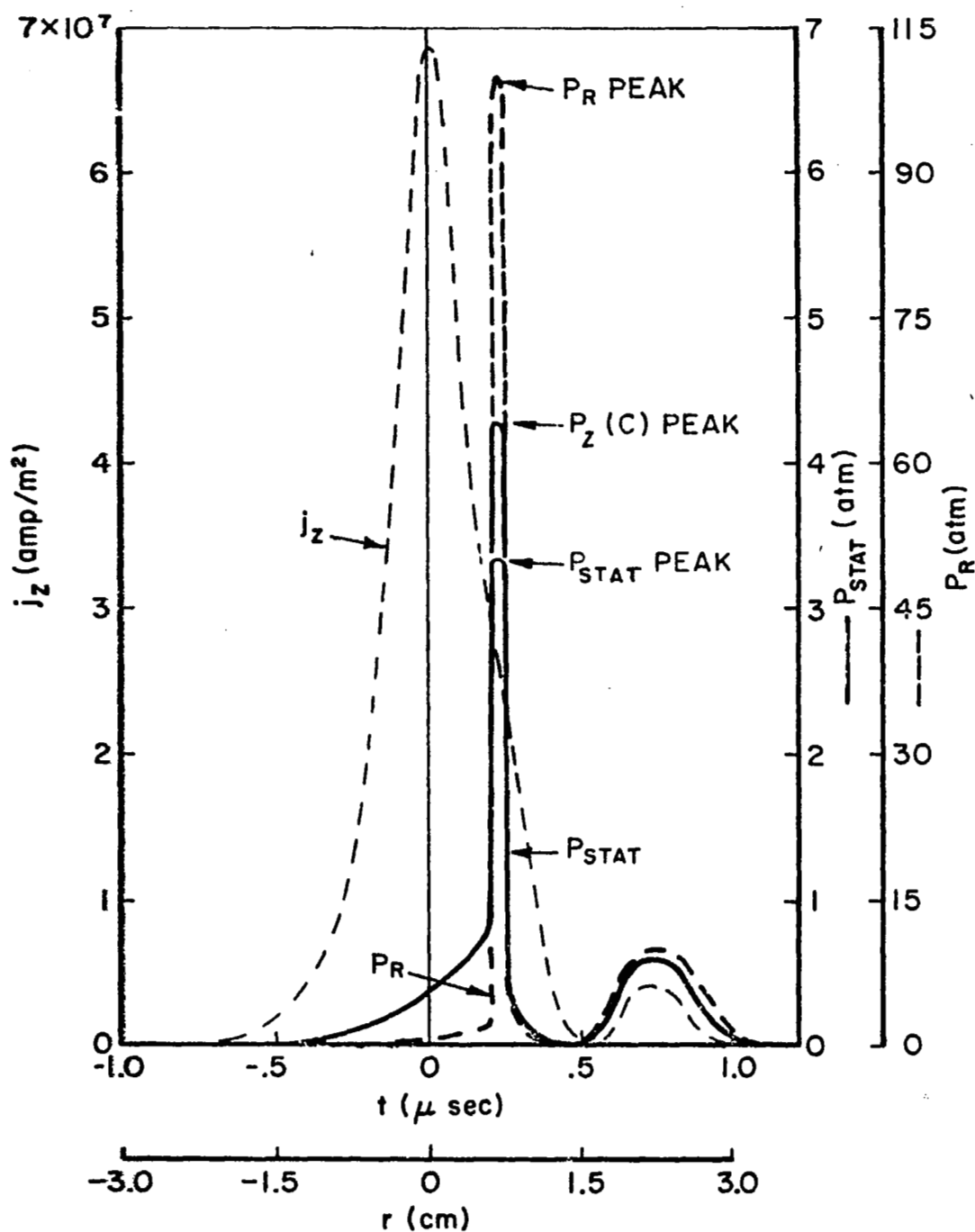
Current Sheet Structure and Dynamics

The degree of ionization within the current sheet can be estimated from measurements of voltage drop across the sheet discharge. Presuming electron current carriers, the corresponding energy increment is balanced with energy loss by inelastic collision to indicate a mean electron temperature of about 4 eV — a value compatible with an assumption of full single ionization near the sheet leading edge.

The intense current conduction in Region I; can be described by a generalized Ohm's law,

$$\vec{j} = C_0 \left[\vec{E} + \vec{v} \times \vec{B} + \frac{P_e}{n_e e} - \frac{\vec{j} \times \vec{B}}{n_e e} \right] \quad (5-1)$$

From experimental data, the electron pressure gradient is



$R = 2''$, $h = 1''$, $t \approx 2. \mu\text{sec}$

CURRENT DENSITY, RADIAL AND AXIAL PRESSURE PROFILES

FIGURE 45

negligible, and further $j_R \approx \phi j_Z \ll j_Z$, so that

$$j_{Ze} \approx \frac{n_e e E_R}{B_\theta} \quad (5-2)$$

estimating radial ion velocity from radial electric field energy arguments, and using measured values of E_R , B_θ it is found that the bulk of the current in Region I is carried by electrons:

$$j_Z(I) \approx j_{Ze} \quad (5-3)$$

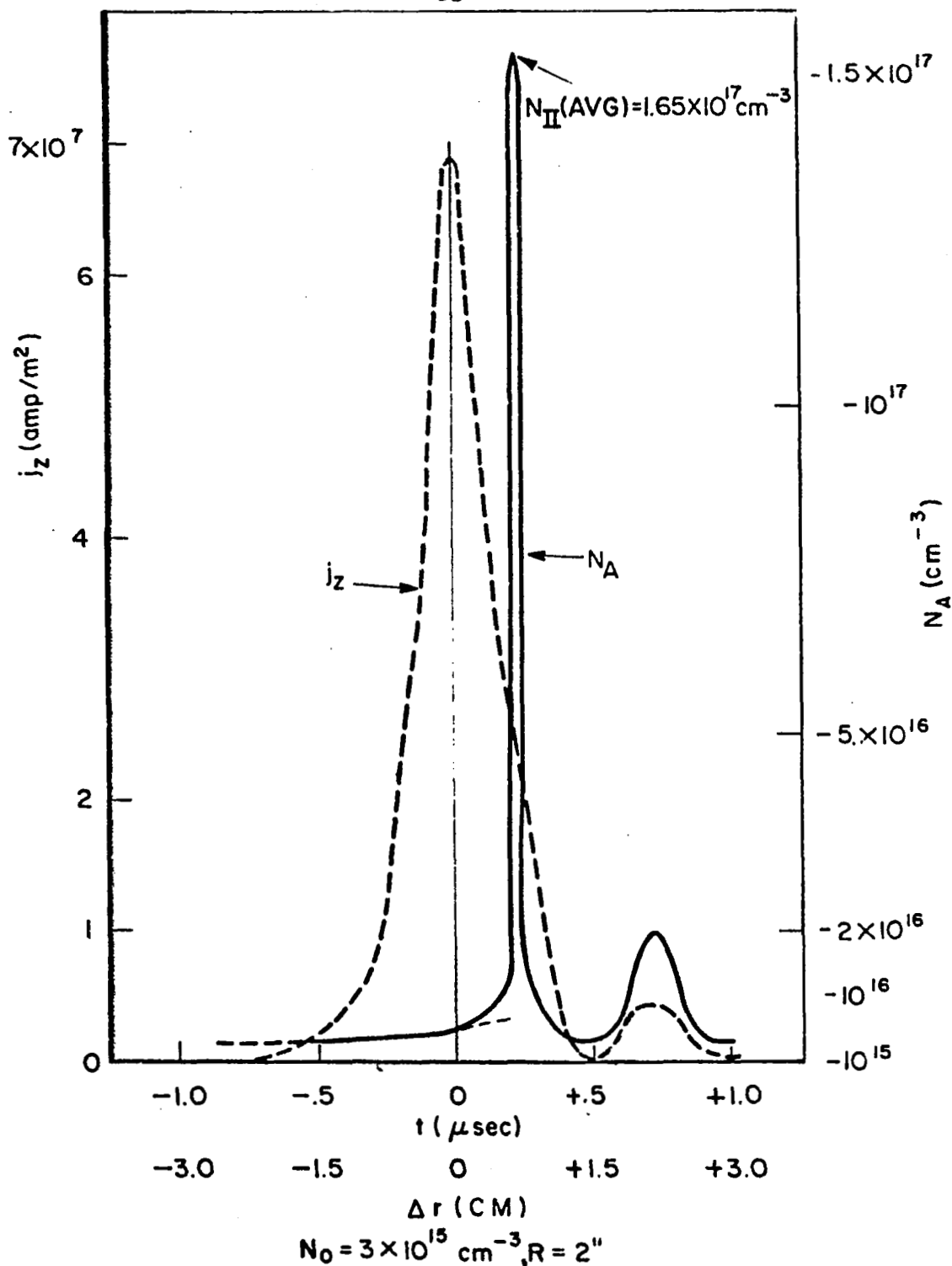
The radial electric field in Region I appears to be the mechanism for transfer of $j \times B$ force density from the electrons to the ions.

The pressure data can be incorporated into the sheet structure analysis in the following manner: the radial pressure is related to heavy particle number density (n) by $P_R = nm_A v_R^2$ and the axial (static) pressure is related to the gas-kinetic temperature (T) through the equation of state

$$P_{STAT} = \sum_j n_j k T_j \approx nk(T_A + T_e) \quad (5-4)$$

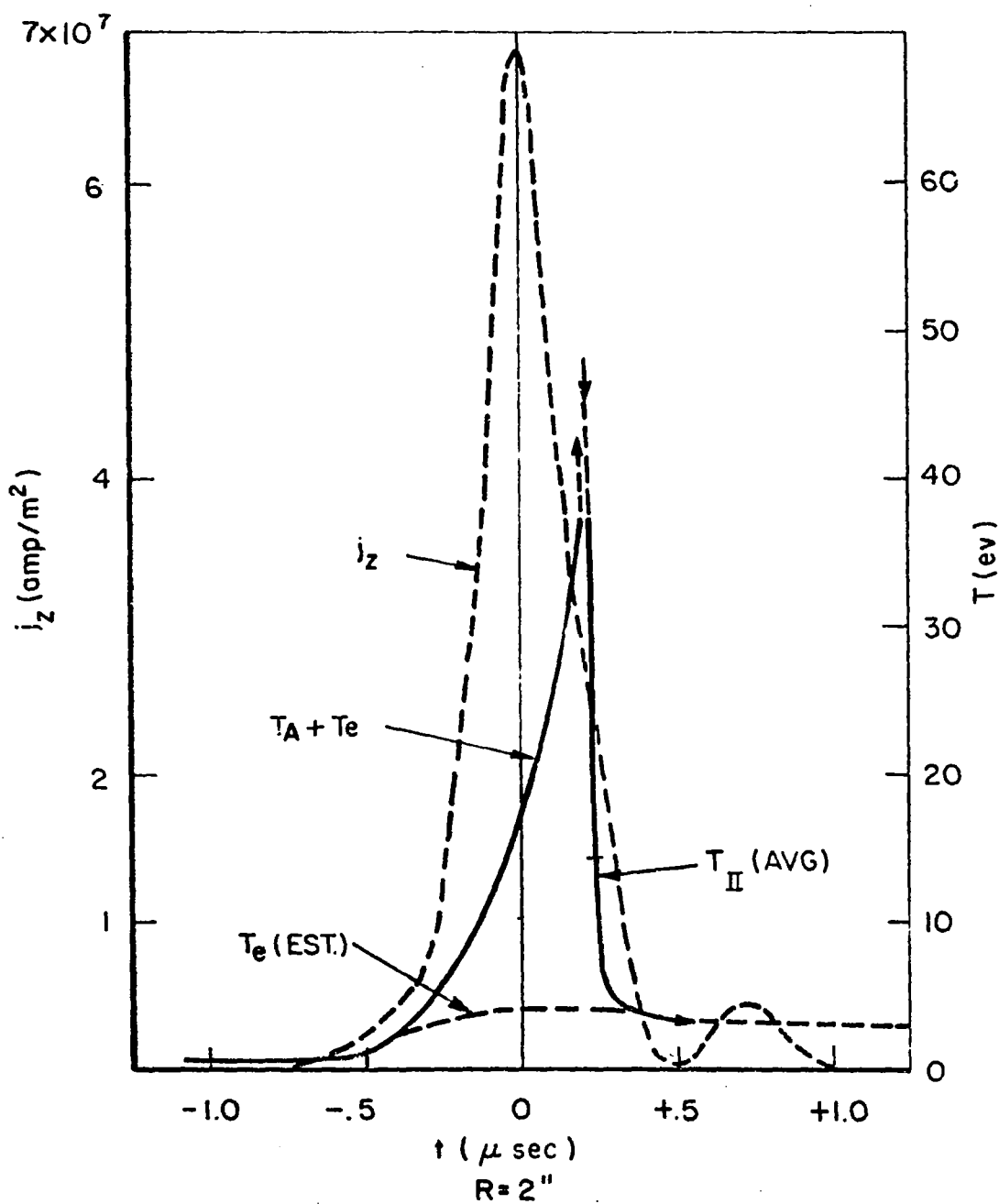
Ion velocities in Region I may be estimated from collisionless energetics through the radial electric field; the radial velocity of the particles in the entrained zone (II) is defined as the measured sheet speed, $v_R = V_s$; in Region III with negligible current density and an estimated moderate conductivity, $v_R \approx E_Z/B_\theta$. The density profile estimated by the above procedures is presented in Fig. 46; the temperature profile indicated by combining the pressure and density in the equation of state is presented in Fig. 47. The particle density profile is related to a sweeping parameter, S , defined as the ratio of entrained mass to that originally in the volume swept by the sheet, in the form

$$S = \left(\frac{n_{II}}{n_o} - 1 \right) \frac{2R\delta}{(R_o^2 - R^2)} \quad (5-5)$$



ESTIMATED NUMBER DENSITY AND CURRENT DENSITY PROFILES

FIGURE 46



ESTIMATED TEMPERATURE AND CURRENT DENSITY
PROFILES

FIGURE 47

where δ is the thickness of Region II with density n_{II} , n_0 is ambient density, and R_0 is chamber radius; δ is determined from the reduction of axial pressure response time during the sheet sweeping event. Typically, $V_s = 3 \times 10^4$ m/sec, $\delta = 1.2$ mm, $n_{II} = 1.6 \times 10^{-16}$ cm $^{-3}$, and $S = 0.90$ indicating a very efficiently sweeping sheet.

A radial momentum balance across the current sheet profile results in the relationship,

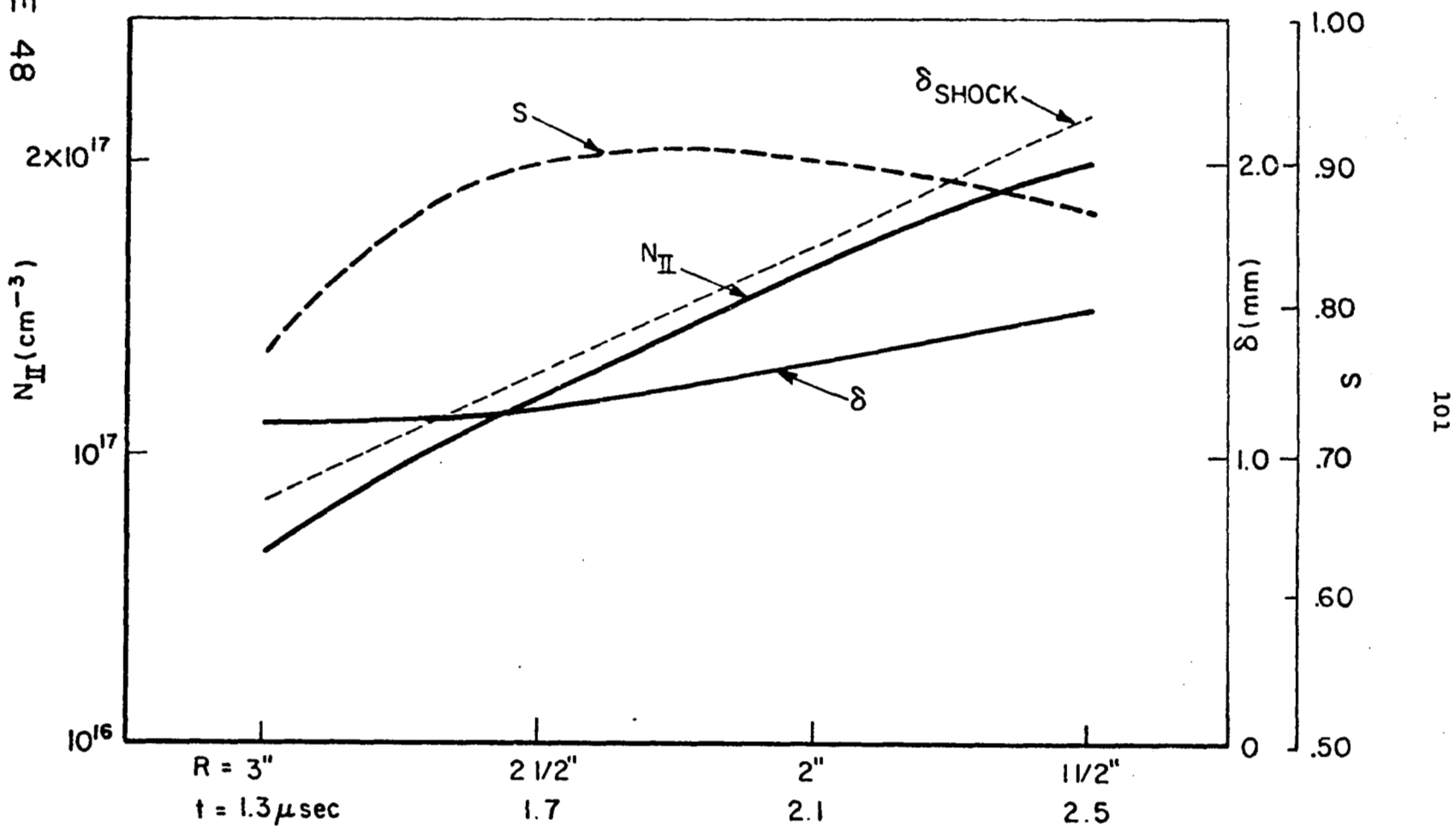
$$P_{jB} \int_{R_1}^{R_2} j_z B_\theta dr \approx \rho_0 V_s^2 S \quad (5-6)$$

Taking typical values, the particle kinetic pressure of the entrained gas, P_{STAT} , roughly equals P_{jB} , the electromagnetic pressure supporting the sheet system. Further, typical values imply $S > 1$, an indication that a correct momentum balance must include wall (electrode) momentum losses.

The sheet tilt angle, ϕ , can be related to the axial pressure increment with the relationship $P_z(C) - P_{STAT} = n_{II} m_A v_{zi}^2$ defining a value of v_{zi} ; this value is in good agreement with the axial sheet velocity component, $V_s \sin \phi$. This fact, along with a Larmor radius of the order of sheet thickness, would appear to indicate that ion turning by the sheet magnetic field produces the characteristic sheet tilt angle.

The radial variation of n_{II} , δ , and S provides another indication of the nature of the acceleration process and is presented in Fig. 48. It can be seen that the density of the entrained gas increases with sheet incursion, while the thickness (δ) remains constant, in complete contrast to the behavior of the shock-heated gas in a classical shock-piston system.

FIGURE 48



RADIAL VARIATION OF PEAK DENSITY, WIDTH OF ENTRAINED ZONE , AND SWEEPING EFFICIENCY

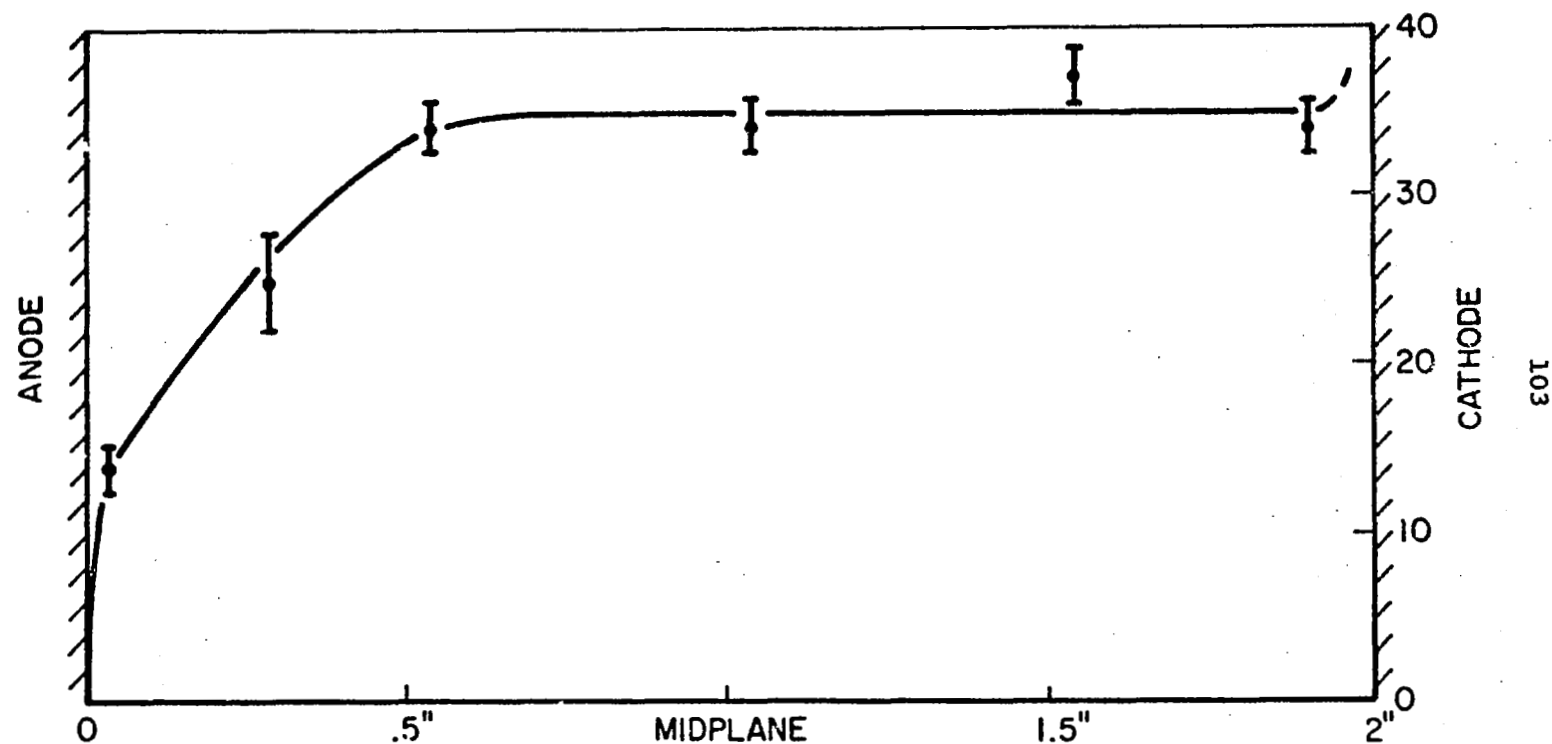
VI. POTENTIAL DISTRIBUTIONS IN A PINCH CHAMBER (Oberth)

In the last report [54] we discussed a drastic asymmetry which was found to exist between the anode and cathode sheaths of the pinch discharge. This asymmetry was demonstrated by an experiment in which portions of the anode and cathode were insulated by circular discs of mylar and the arc voltage was monitored for each situation. We observed that insulation of the anode caused the arc voltage to increase significantly (from 50 to 160 volts), whereas cathode insulation had only a minor effect.

In an effort to examine the structure of the anode sheath and adjacent discharge region, a single tip electrostatic probe has been designed to measure local plasma potential (less a small sheath correction around the probe tip). In its first application, the probe has been used to map plasma potential in the slightly ionized region ahead of the propagating current sheet. With no insulation on either electrode, and the current sheet at a radius of about 3 in., it is found that almost all of the voltage drop occurs across a region within 1/2 in. of the anode surface (Fig. 49). The gradient attains its strongest value of about 2 v/cm right at the anode surface. No comparable region of strong electric field is found near the cathode.

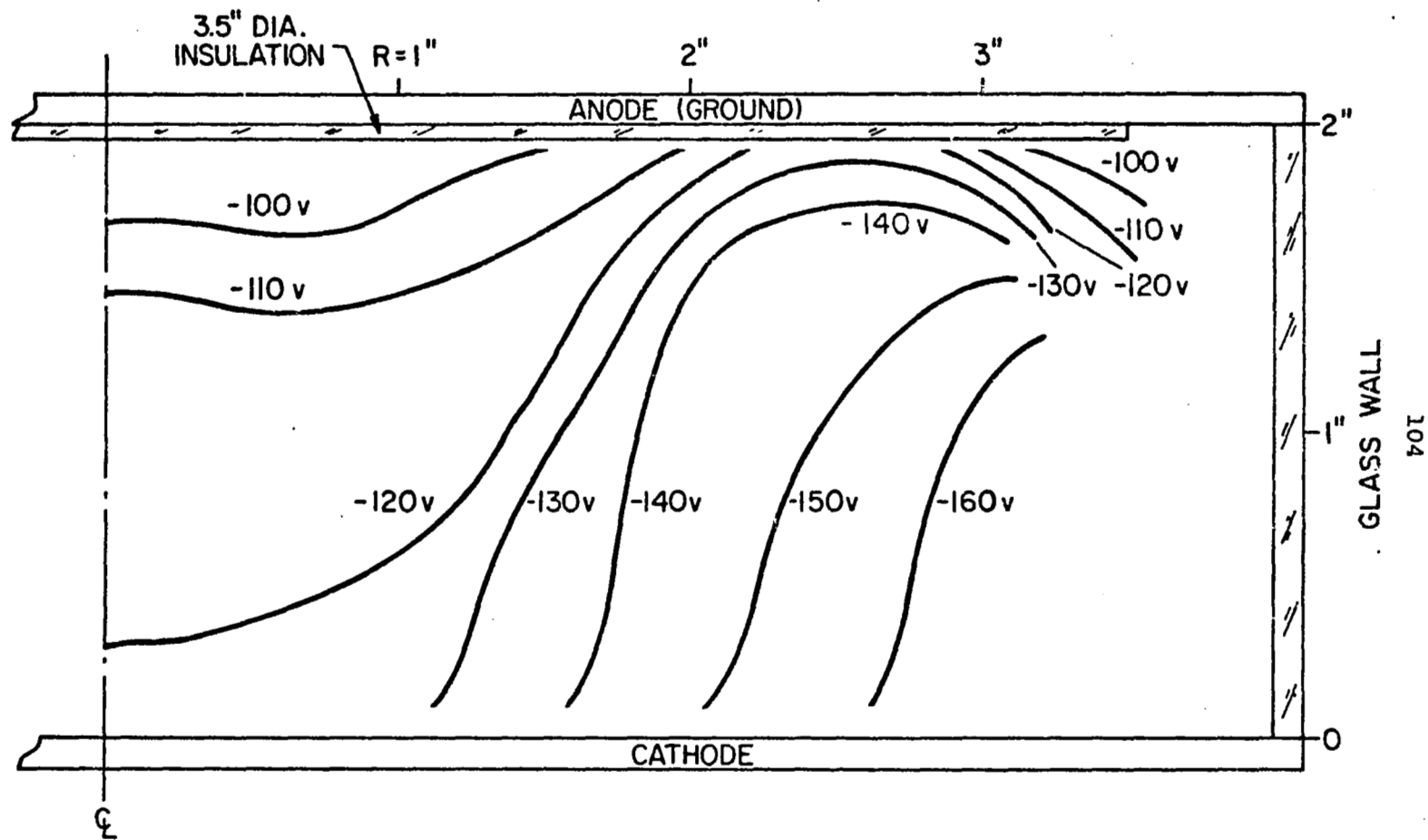
Similar series of experiments are now in progress for cases where the anode and/or cathode are insulated with circular mylar discs. It is noted that anode insulation causes a threefold increase in arc voltage, even before the current sheet arrives at the insulated portion, suggesting that it may not be the high-current density conduction processes in the sheet itself, but those in the ambient plasma ahead of the sheet which determine the arc voltage. Details of this possibility should be clarified by maps of the potential contours throughout the pinch chamber, such as that shown in Fig. 50 for various anode insulated discharges.

FIGURE 49



VOLTAGE DISTRIBUTION ACROSS CHAMBER AT 1 INCH RADIUS

$t = 1 \mu \text{ sec}$
CURRENT SHEET AT $R = 3''$



POTENTIAL CONTOURS IN CHAMBER

$t = 1 \mu\text{sec}$

CURRENT SHEET AT $R = 3.5"$

VII. POPULATION INVERSION IN A PULSED DISCHARGE (Bruckner)

The laser interferometry of the pinch discharge has been brought to a conclusion, with the feeling that the technique is now sufficiently developed to justify application to our more advanced accelerators. The first application will be to the parallel-plate device in the configuration used by Eckbreth for his studies of transition to quasi-steady acceleration modes [59]. The first phase of this study is not strictly interferometric in nature, but consists of examining the effects of the argon discharge plasma on the radiation produced by an argon ion laser. It is hoped in this manner to determine whether there exists in this discharge an inversion in the relative populations of certain argon ion energy levels, as indicated by negative absorption of certain wavelengths of light.

The work of Eckbreth on this parallel-plate device revealed evidence of conditions favorable to the onset of population inversion, i.e., current densities of the order of hundreds of amp/cm^2 at particle densities of $10^{14} - 10^{15} \text{ cm}^{-3}$. In addition, Hertzberg and Leonard have recently reported the existence of inversion in the plume of a long pulse (10 msec) MPD arc operating on argon [A-6].

On the basis of these encouraging indications we have acquired a TRW Model 71-A pulsed argon-ion laser and are in the process of setting up the ancillary equipment and carrying out preliminary tests. Initial operations will be confined to the 4880 \AA wavelength component of the laser because of the wealth of information available in the literature on this particular line.

The probing of an ionized gas with radiation from a laser using the same ionized gas should prove to be a highly useful diagnostic technique because the absorption (be it positive or negative) of radiation is closely related to the

density and temperature, and to the relative populations of the energy levels involved. Combined with our previously reported interferometric techniques it may lead to compilation of previously inaccessible data on the structure of the accelerating zone. The broader implication of population inversions to plasma propulsion resides in the associated frozen flow losses for monatomic-ionic species, which may not be insignificant in view of the relatively high electronic energy levels involved.

VIII. CATHODE JET STUDIES (Turchi)

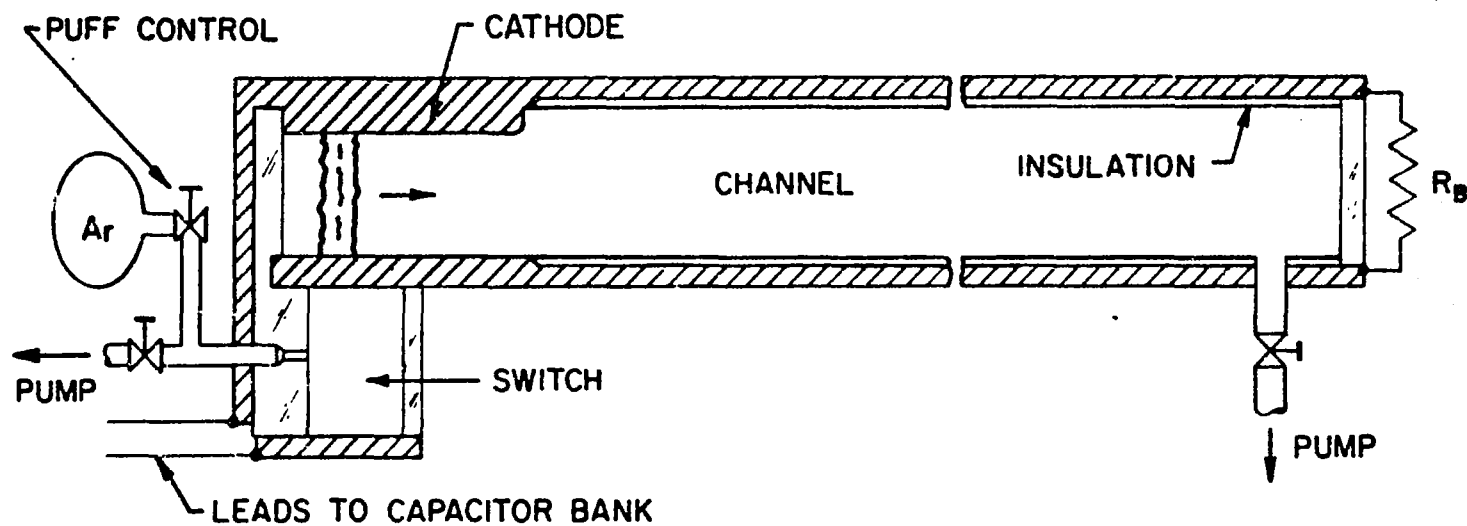
A variety of processes can contribute to gas acceleration in a high-current discharge. In addition to several combinations of crossed-field interactions, electrothermal heating of a magnetically constrained jet and electrostatic action may be involved. In coaxial discharges of the MPD class, the cathode jet region of the plasma flow is of particular interest. It is in this region that the intensity of magnetic forces is greatest and that the most violent plasma and electrode heating phenomena occur.

The goal of the research program to be described is to delineate and understand the processes involved in the cathode jet that contribute to the high specific impulse capability of magnetoplasma dynamic arcs. This includes not only the various gas acceleration mechanisms, but also the processes whereby the cathode can sustain extremely high-current densities. For example, we may possibly have some sort of magnetic shielding effect, or perhaps a virtual cathode that spreads the current out along the jet or entrains ions before they reach the cathode. The approach to this problem involves detailed interior study of the structure of a very large cathode jet by means of magnetic and electric probes, pressure probes, detailed photography and perhaps a new generation of floating double probes.

To be able to perform these investigations in the necessary detail requires some modification of the situation usually found in actual thruster operation. The rather small initial cross section of the cathode jet in such situations must be altered so that the introduction of probes does not radically distort the discharge, or substantially obstruct the flow of current. Any alteration will inevitably compromise some of the physical characteristics of the actual situation. For example, in a coaxial configuration, the magnetic field near the cathode tip is quite intense and possesses,

in addition, a strong gradient and curvature. While the intensity and variation of the magnetic field may be simulated with a different geometry, the field curvature is rather distinctive. Any phenomena associated with such curvature will be lost in transformation to another configuration. Nevertheless, to obtain at least some information about cathode jet phenomena, we propose to sacrifice such things as field curvature effects by transforming to a parallel-plate type geometry. Now, by spreading the total discharge current over the width of the cathode plate, we may probe a region of the jet without substantially affecting the overall discharge mode and, by proper approach to the point of measurement, without greatly disturbing the local current and plasma flows with the probe structure. To compensate for the expansion of the discharge geometry, we shall operate at much higher current levels than are found in steady-state MPD arcjets, so that the field intensity and (to a lesser degree) the current density levels are quite similar. If we fashion the cathode tip in such a way that the discharge attachment thickness is similar to the attachment radius normally found, then we may even recover some of the field gradient effects.

At present, preliminary studies are being conducted in a modified version of the parallel-plate accelerator used for several other studies [59]. Here the channel has been altered by the addition of a cathode plate over the original cathode surface (Fig. 51). This plate has a 1/4-in. radius at the discharge attachment edge and serves to initiate the cathode jet away from the insulator surface (the initial separation was calculated on the basis of a thermal boundary layer resulting from the balance of ohmic heating with electronic heat conduction). In this way, a simple modification of existing equipment allows us to carry out necessary preliminary investigations prior to the design of a more appropriate system in which the cathode jet will project symmetrically between two anodes.



SCHEMATIC DIAGRAM OF PARALLEL PLATE ACCELERATOR
MODIFIED FOR CATHODE JET STUDIES

Magnetic probe studies at two current levels (17 and 42 kA) and two values of initial pressure (50 and 100 μ of argon) indicate that the discharge in this device has no tendency to "spoke" but spreads rather uniformly over most of the cathode width. The cathode jet appears to extend several inches downstream of the cathode edge with higher current and lower initial pressure levels exhibiting the greater downstream extension. The electric and magnetic field distributions within the cathode jet are presently being mapped out in detail. The results obtained from this series of investigations and the experience gained from the design and operation of various probes in this environment will be applied to the design of experiments and apparatus to be conducted at higher current levels, with longer pulse times to allow gas-dynamic, as well as electromagnetic, stabilization of the discharge (see Sec. IX).

IX. A 100 KILOJOULE PULSE-FORMING NETWORK POWER SUPPLY
FOR A QUASI-STEADY PLASMA ACCELERATOR (Di Capua)

Proper study of the phenomenon of current sheet stabilization in pulsed plasma accelerators, previously observed in this laboratory and elsewhere [57,59,A-2] requires observation over a millisecond time scale, rather than the microsecond scale more common in most pulsed plasma work. The gas-dynamic processes in quasi-steady accelerators are governed by the sound speed, and for useful device dimensions predicate current pulse lengths of hundreds of microseconds if both current pattern and flow stabilization are to be achieved simultaneously. Moreover, this pulse length cannot be achieved at the expense of current amplitude; for vigorous electromagnetic acceleration the current level in these pulses must be retained in the order of 100,000 amperes. The composite requirement is thus for an energy storage facility substantially larger than the 6400 joule bank presently in use in this laboratory.

Recently we have obtained on long-term loan a set of 128 26-microfarad capacitors rated at 10 kV, from which we are constructing a 10^5 joule pulse line. The configuration chosen consists of four LC ladder networks each assembled from 30 equal sections. Each network will deliver, when charged to 8 kV, a flattop current pulse of 62.5 kA for 200 μ sec into a short circuit load. The following table summarizes the current pulses available from the network.

Connection	Length of Pulse	Short Cir- cuit Current
4 lines in series.	800 μ sec	62.5 kA
4 lines in series-parallel . . .	400 μ sec	125.0 kA
4 lines in parallel.	200 μ sec	250.0 kA

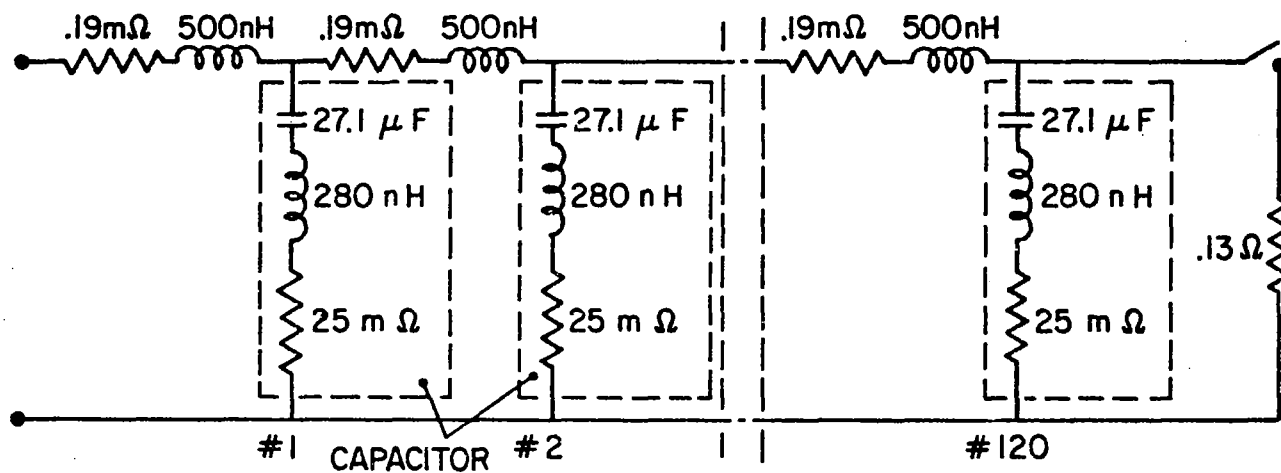
Each section of the ladder network will consist of a series inductor of 500 nH and a shunt capacitor of 27.1 μ fd. To obtain

a flattop current pulse this inductance should be larger than the self-inductance of each individual capacitor. A diagram of the ladder network is shown in Fig. 52.

The capacitance, self-inductance, and resistance of the capacitors were determined by testing five units chosen at random. The capacitance of each one of these units was measured directly with a capacitance bridge. The ringing frequency and resistance of the units were obtained by loading each capacitor to 180 volts and discharging it through a low inductance switch, monitoring the current in the circuit with a Rogowski coil. The switch utilizes the mechanism of a large mouse trap to close the circuit. The self-inductance was calculated from the ringing frequency while the resistance was obtained from the envelope of the decay. The results, averaged for the five units, are as follows (Fig. 52):

Capacitance.	27.1 μ F
Self-inductance. . . .	280.0 nH
Resistance	25.0 m Ω
Ringing Frequency. . .	58.0 Kc/sec

There are two additional limitations on the design of the network: (1) the maximum current tolerable to each capacitor and (2) the maximum peak-to-peak voltage allowed on the capacitors. The specified maximum allowable current in each capacitor is 52,000 amperes. Tests performed on a prototype network show that each capacitor delivers at most 1/3 of the total current, i.e., 20 kA which is well below the maximum value. The maximum peak-to-peak voltage on the capacitors should not exceed 12 kV if the lifetime of the capacitors is not to be seriously compromised. Therefore the capacitors, though rated at 10 kV, will be operated only at 8 kV, and reversal will only be allowed to -4 kV, by utilizing a crow-barring resistor at the back end of the network. This resistor, whose value is equal to the characteristic impedance of the line, will be switched into the line by an ignitron when the current pulse reaches the end of the network.



SCHEMATIC OF PULSE FORMING NETWORK

FIGURE 52

Due to the large amount of energy stored in the network, each capacitor must be adequately fused since a fault in one of the units when the bank is fully loaded will release enough energy within the faulted unit to rupture the capacitor case. For this purpose, each capacitor will be connected to the series inductor through a fuse which consists of 4 in. of #16 AWG tinned copper wire surrounded by Tygon tubing. For additional protection, each unit in the bank will be surrounded by 3/4 in. of plywood.

The fuse was tested experimentally in the laboratory by switching a prototype network across it at 4700 volts. The results of the test are shown in Fig. 53. The top trace in each oscillogram shows the voltage across the fuse while the bottom trace shows the current in the circuit. The top oscillogram was obtained by replacing the fuse by a 4-in. long, 0.064-in. thick, 1-in. wide aluminum strip and shows the usual ringdown decay of the current in the bank. The bottom oscillogram shows a marked rise of the voltage across the fuse after 220 μ sec and the current is actually interrupted after 520 μ sec.

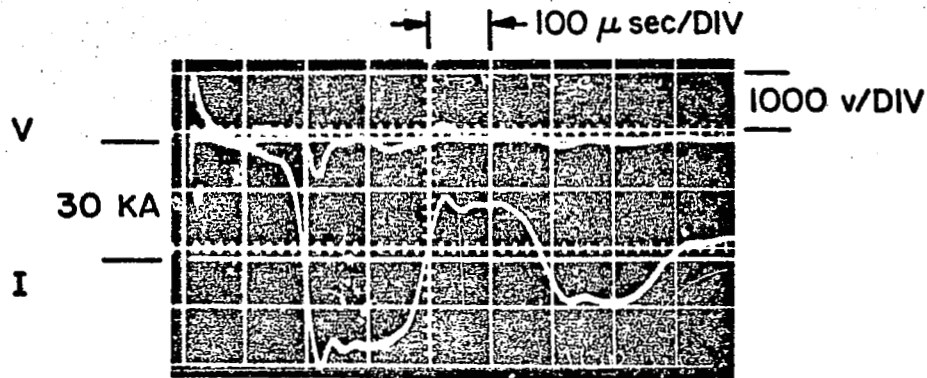
The energy released in a capacitor when a fault occurs is given by

$$Q_f(t) = \int_0^t I^2 R_F dt \quad (9-1)$$

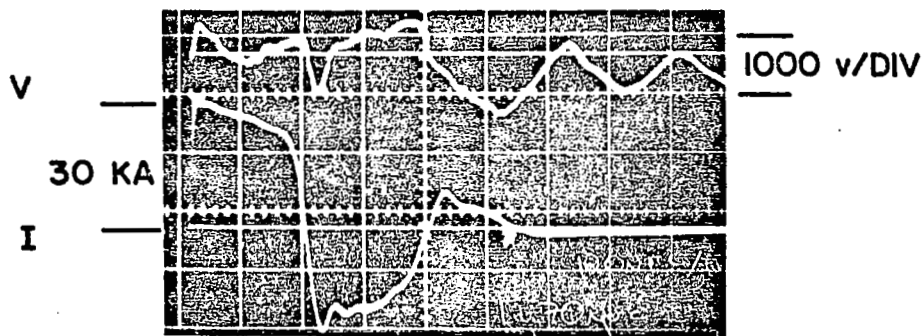
This fault will typically be an arc with a resistance R_F in the order of 10 m Ω . If we assume this resistance to be constant, a maximum value of Q_f of 2000 joules will require that:

$$\int_0^t I^2 dt = 2 \times 10^5 \text{ A}^2 \text{ sec} \quad (9-2)$$

The experimental results shown in the bottom oscillogram



a) ALUMINUM STRIP



b) FUSE

VOLTAGE AND CURRENT IN FUSE TEST

of Fig. 53 show that the fuse wire interrupts the current when

$$\int_0^t I^2 dt = 2.2 \times 10^5 \text{ A}^2 \text{ sec} \quad (9-3)$$

The fuses were then incorporated into each unit of a prototype of the transmission line and preliminary tests indicate that a pulse of the desired characteristics can be obtained from such a configuration. We are, therefore, proceeding with the construction of the permanent line.

PROJECT REFERENCES

1. Proposed Studies of the Formation and Stability of an Electromagnetic Boundary in a Pinch, proposal for NASA Research Grant NsG-306-63, Princeton University, 5 March 1962.
2. Pulsed Electromagnetic Gas Acceleration, 1st Semi-Annual Progress Report for the period 1 July 1962 to 31 December 1962, Princeton University Aeronautical Engineering Report No. 634, January 1963.
3. "The Plasma Pinch as a Gas Accelerator," AIAA Electric Propulsion Conference, 11-13 March 1963, AIAA Preprint 63013.
4. Pulsed Electromagnetic Gas Acceleration, 2nd Semi-Annual Progress Report for the period 1 January 1963 to 30 June 1963, Princeton University Aeronautical Engineering Report No. 634a, June 1963.
5. Structure of a Large-Radius Pinch Discharge, AIAA Journal 1, 8, 1809-1814 (1963).
6. Gas-Triggered Inverse Pinch Switch, Review of Scientific Instruments 34, 12, 1439-1440 (1963).
7. A Gas-Triggered Inverse Pinch Switch, technical note, Princeton University Aeronautical Engineering Report No. 660, August, 1963.
8. "Pulsed Electromagnetic Gas Acceleration," 4th NASA Inter-center Conference on Plasma Physics, Washington, D. C., Paper No. II, 8, 2-4 December, 1963.
9. "Current Distributions in Large-Radius Pinch Discharges," AIAA Aerospace Sciences Meeting, 20-22 January 1964, AIAA Preprint No. 64-25.
10. Current Distributions in Large-Radius Pinch Discharges, AIAA Bulletin 1, 1, 12 (1964).
11. Current Distributions in Large-Radius Pinch Discharges, AIAA Journal 2, 10, 1749-1753 (1964).
12. Pulsed Electromagnetic Gas Acceleration, 3rd Semi-Annual Progress Report for the period 1 July 1963 to 31 December 1963, Princeton University Aeronautical Engineering Report No. 634b, December, 1963.
13. Pulsed Electromagnetic Gas Acceleration, renewal proposal for 15-months extension of NASA Research Grant NsG-306-63, Princeton University, 15 January 1964.
14. Pulsed Electromagnetic Gas Acceleration, 4th Semi-Annual Progress Report for the period 1 January 1964 to 30 June 1964, Princeton University Aerospace and Mechanical Sciences Report No. 634c, July, 1964.

PROJECT REFERENCES-contd

15. Gas-Triggered Pinch Discharge Switch, Princeton University Aerospace and Mechanical Sciences Technical Note No. 101, July, 1964.
16. Gas-Triggered Pinch Discharge Switch, Review of Scientific Instruments 36, 1, 101-102 (1965).
17. J. M. Corr, "Double Probe Studies in an 8" Pinch Discharge," M.S.E. thesis, Department of Aerospace and Mechanical Sciences, Princeton University, Princeton, New Jersey, 1964.
18. Exhaust of a Pinched Plasma From an Axial Orifice, AIAA Bulletin 1, 10, 570 (1964).
19. "Exhaust of a Pinched Plasma From an Axial Orifice," AIAA 2nd Aerospace Sciences Meeting, New York, New York, 25-27 January 1965, AIAA Paper No. 65-92.
20. Ejection of a Pinched Plasma From an Axial Orifice, AIAA Journal 3, 10, 1862-1866 (1965).
21. Pulsed Electromagnetic Gas Acceleration, 5th Semi-Annual Progress Report for the period 1 July 1964 to 31 December 1964, Princeton University Aerospace and Mechanical Sciences Report No. 634a, July, 1964.
22. On the Dynamic Efficiency of Pulsed Plasma Accelerators, AIAA Journal 3, 6, 1209-1210 (1965).
23. Linear Pinch Driven by a High-Current Pulse-Forming Network, AIAA Bulletin 2, 6, 309 (1965).
24. "Linear Pinch Driven by a High-Current Pulse-Forming Network," 2nd AIAA Annual Meeting, San Francisco, California, 26-29 July 1965, AIAA Paper No. 65-336.
25. E. S. Wright, "The Design and Development of Rogowski Coil Probes for Measurement of Current Density Distribution in a Plasma Pinch," M.S.E. thesis, Department of Aerospace and Mechanical Sciences, Princeton University, Princeton, New Jersey, 1965.
26. The Design and Development of Rogowski Coil Probes for Measurement of Current Density Distribution in a Plasma Pinch, Princeton University Aerospace and Mechanical Sciences Report No. 740, June, 1965.
27. Pulsed Electromagnetic Gas Acceleration, renewal proposal for 12-months extension of NASA Research Grant NsG-306-63, Princeton University, 7 June 1965.
28. Miniature Rogowski Coil Probes for Direct Measurement of Current Density Distribution in Transient Plasmas, Review of Scientific Instruments 36, 12, 1891-1892 (1965).

PROJECT REFERENCES-contd

29. Pulsed Electromagnetic Gas Acceleration, 6th Semi-Annual Progress Report for the period 1 January 1965 to 30 June 1965, Princeton University Aerospace and Mechanical Sciences Report No. 634e, July, 1965.
30. G. A. Rowell, "Cylindrical Shock Model of the Plasma Pinch," M.S.E. thesis, Department of Aerospace and Mechanical Sciences, Princeton University, Princeton, New Jersey, 1966.
31. Cylindrical Shock Model of the Plasma Pinch, Princeton University Aerospace and Mechanical Sciences Report No. 742, February, 1966.
32. Pulsed Electromagnetic Gas Acceleration, 7th Semi-Annual Progress Report for the period 1 July 1965 to 31 December 1965, Princeton University Aerospace and Mechanical Sciences Report No. 634f, January, 1966.
33. Electric and Magnetic Field Distributions in a Propagating Current Sheet, AIAA Bulletin 3, 1, 35 (1966).
34. "Electric and Magnetic Field Distributions in a Propagating Current Sheet," AIAA 5th Electric Propulsion Conference, San Diego, California, 7-9 March 1966, AIAA Paper No. 66-200.
35. "Pulse-Forming Networks for Propulsion Research," paper presented at the 7th Symposium on Engineering Aspects of Magnetohydrodynamics, Princeton University, Princeton, New Jersey, March 30-April 1, 1966 (p. 10-11 of proceedings).
36. N. A. Black, "Dynamics of a Pinch Discharge Driven by a High Current Pulse-Forming Network," Ph.D. thesis, Department of Aerospace and Mechanical Sciences, Princeton University, Princeton, New Jersey, 1966.
37. Dynamics of a Pinch Discharge Driven by a High Current Pulse-Forming Network, Princeton University Aerospace and Mechanical Sciences Report No. 778, May, 1966.
38. "Pulsed Plasma Propulsion," paper presented at the 5th NASA Intercenter and Contractors Conference on Plasma Physics, Washington, D. C., 24-26 May 1966, p. 75-81, part V of proceedings.
39. Pulsed Electromagnetic Gas Acceleration, renewal proposal for 24-months extension of NASA Research Grant NsG-306-63, Princeton University, 25 May 1966.
40. A Large Dielectric Vacuum Facility, AIAA Journal 4, 6, 1135 (1966).
41. R. L. Burton, "Structure of the Current Sheet in a Pinch Discharge," Ph.D. thesis, Department of Aerospace and Mechanical Sciences, Princeton University, Princeton, New Jersey, 1966.

PROJECT REFERENCES-contd

42. Structure of the Current Sheet in a Pinch Discharge, Princeton University Aerospace and Mechanical Sciences Report No. 723, September, 1966.
43. Pulsed Electromagnetic Gas Acceleration, 8th Semi-Annual Progress Report for the period 1 January 1966 to 30 June 1966, Princeton University Aerospace and Mechanical Sciences Report No. 634g, July, 1966.
44. Electromagnetic Propulsion, Astronautics and Aeronautics 4, 69 (1966).
45. W. R. Ellis, Jr., "An Investigation of Current Sheet Structure in a Cylindrical Z-Pinch," Ph.D. thesis, Department of Aerospace and Mechanical Sciences, Princeton University, Princeton, New Jersey, 1967.
46. "Current Status of Plasma Propulsion," AIAA 2nd Propulsion Joint Specialist Conference, Colorado Springs, Colorado, 13-17 June 1966, AIAA Paper No. 66-565.
47. Pulsed Electromagnetic Gas Acceleration, 9th Semi-Annual Progress Report for the period 1 July 1966 to 31 December 1966, Princeton University Aerospace and Mechanical Sciences Report No. 634h, January, 1967.
48. Pulsed Electromagnetic Gas Acceleration, 10th Semi-Annual Progress Report for the period 1 January 1967 to 30 June 1967, Princeton University Aerospace and Mechanical Sciences Report No. 634i, July, 1967.
49. "Current Pattern Stabilization in Pulsed Plasma Accelerators," AIAA Electric Propulsion and Plasmadynamics Conference, Colorado Springs, Colorado, 11-13 September 1967, AIAA Paper No. 67-656.
50. An Investigation of Current Sheet Structure in a Cylindrical Z-Pinch, Princeton University Aerospace and Mechanical Sciences Report No. 805, July, 1967.
51. Pulsed Electromagnetic Gas Acceleration, 11th Semi-Annual Progress Report for the period 1 July 1967 to 31 December 1967, Princeton University Aerospace and Mechanical Sciences Report No. 634j, January, 1968.
52. Current Pattern Stabilization in Pulsed Plasma Accelerators, AIAA Bulletin 4, 9, 433 (1967).
53. Jahn, R. G.: "Physics of Electric Propulsion," McGraw-Hill Book Company, New York, 1968.

PROJECT REFERENCES-contd

54. Pulsed Electromagnetic Gas Acceleration, 12th Semi-Annual Progress Report for the period 1 January 1968 to 30 June 1968, Princeton University Aerospace and Mechanical Sciences Report No. 634k, July, 1968.
55. P. J. Wilbur, "Energy Transfer from a Pulse Network to a Propagating Current Sheet," Ph.D. thesis, Department of Aerospace and Mechanical Sciences, Princeton University, Princeton, New Jersey, 1968.
56. Energy Transfer from a Pulse Network to a Propagating Current Sheet, Princeton University Aerospace and Mechanical Sciences Report No. 846, September, 1968.
57. Current Pattern Stabilization in Pulsed Plasma Accelerators, AIAA Journal 6, 11, 2125 (1968).
58. A. C. Eckbreth, "Current Pattern and Gas Flow Stabilization in Pulsed Plasma Accelerators," Ph.D. thesis, Department of Aerospace and Mechanical Sciences, Princeton University, Princeton, New Jersey, 1968.
59. Current Pattern and Gas Flow Stabilization in Pulsed Plasma Accelerators, Princeton University Aerospace and Mechanical Sciences Report No. 857, December, 1968.
60. T. M. York, "Pressure Distribution in the Structure of a Propagating Current Sheet," Ph.D. thesis, Department of Aerospace and Mechanical Sciences, Princeton University, Princeton, New Jersey, 1968.
61. Pressure Distribution in the Structure of a Propagating Current Sheet, Princeton University Aerospace and Mechanical Sciences Report No. 853, December, 1968.
62. Current Pattern and Gas Flow Stabilization in Pulsed Plasma Accelerators, AIAA Bulletin 5, 12, 730 (1968).
63. "Current Pattern and Gas Flow Stabilization in Pulsed Plasma Accelerators," AIAA 7th Aerospace Sciences Meeting, New York, New York, 20-22 January 1969, AIAA Paper No. 69-112.
64. Energy Transfer from a Pulse Network to a Propagating Current Sheet, AIAA Bulletin 5, 12, 730 (1968).
65. "Energy Transfer from a Pulse Network to a Propagating Current Sheet," AIAA 7th Aerospace Sciences Meeting, New York, New York, 20-22 January 1969, AIAA Paper No. 69-113.

PROJECT REFERENCES-contd.

66. K. E. Clark, "Quasi-steady Plasma Acceleration," Ph.D. thesis, Department of Aerospace and Mechanical Sciences, Princeton University, Princeton, New Jersey, February 1969.
67. Pressure Distribution in the Structure of a Propagating Current Sheet, AIAA Bulletin 6, 2, 75 (1969).
68. "Pressure Distribution in the Structure of a Propagating Current Sheet," AIAA 7th Electric Propulsion Conference, Williamsburg, Virginia, 3-5 March 1969, AIAA Paper No. 69-264.
69. Quasi-steady Plasma Acceleration, " AIAA Bulletin 6, 2, 75 (1969).
70. "Quasi-steady Plasma Acceleration," AIAA 7th Electric Propulsion Conference, Williamsburg, Virginia, 3-5 March 1969, AIAA Paper No. 69-267.

GENERAL REFERENCES

- A-1. L. C. Burkhardt, and R. H. Lovberg: "Current sheet in a coaxial gun," Phys. Fluids 5, 3, 341 (1962).
- A-2. R. L. Burton, and O. V. Chang: "Acceleration process in a stabilized high-current arc," AIAA J. 6, 11, 2190-2192 (1968).
- A-3. T. G. Jones, and G. C. Vlases: "Pressure probes for research in plasma dynamics and detonation," Rev. Sci. Instr., vol. 30, August, 1967.
- A-4. N. V. Fillipov: "Investigation of pressures in a powerful pulsed gas discharge using a piezoelectric measuring device," Vol. 3 of Plasma Physics and The Problems of Controlled Thermonuclear Reactions, Pergamon Press, Inc., New York (1959).
- A-5. G. C. Vlases: "Shock and current layer structure in an electromagnetic shock tube," Phys. Fluids 10, 2351 (1967).
- A-6. R. L. Leonard, and A. Hertzberg: University of Washington, Seattle, Wash., private communication.

END

DATE

FILMED

APR 29 1969